`

`

The Dissertation Committee for Matthew David West Certifies that this is the approved version of the following dissertation:

Low Thermal Expansion Transition Metal Oxides for Reduced Temperature Solid Oxide Fuel Cell Cathodes

Committee:

Arumugam Manthiram, Supervisor

Desiderio Kovar

John Ekerdt

Gyeong Hwang

Charles B. Mullins

`

Low Thermal Expansion Transition Metal Oxides for Reduced Temperature Solid Oxide Fuel Cell Cathodes

by

Matthew David West, B.S.Ch.E.

Dissertation

Presented to the Faculty of the Graduate School of

The University of Texas at Austin

in Partial Fulfillment

of the Requirements

for the Degree of

Doctor of Philosophy

The University of Texas at Austin

December 2014

`

Dedication

For my wife, Ashley

Acknowledgements

First, I would like to thank my advisor, Dr. Arumugam Manthiram, for his years of support and advice.

I would also like to thank my fellow labmates, past and present, for their advice, support, and friendship. First I would like to thank my solid oxide fuel cell colleagues, Jung-Hyun Kim, Young-Nam Kim, Daeil Yoon, and Ke-Yu Lai, for their years of collaboration, advice, and friendship. They all helped to bring a sense of a closely knit lab environment to a group of around thirty people, and I will always be grateful for their patience with my many questions and their advice with tough problems. I would also like to thank my fellow chemical engineering labmates, James Knight, Matthew Beaudry, and Craig Milroy. Graduate school has been a struggle for all of us, but I like to think that our friendship has made it all more bearable. I would like to thank Zach Rosenberg-Moorhead for sharing an office with me through the years, and patiently answering all my materials science questions along with our discussions about Star Trek, space travel, and racecar. There are many times more labmates that I do not have the space to mention, but they have all made a significant impact upon my tenure in the Manthiram laboratory.

I had the good fortune of working very closely with two undergraduate students during my studies, and I would like to thank Christina Ortiz and Soa-Jin Sher for their friendship and assistance during these long years. It has been my greatest pleasure and privilege in graduate school to be a mentor to these students, and I am grateful they chose to work with me for the past three years. Much of their work is included in these pages, and I will be forever grateful to them for helping me achieve my dream.

`

Through my years at the University of Texas at Austin, I had the fortune to be a teaching assistant for a few courses. In particular, I would like to thank Drs. Douglas Lloyd and Robb Wilson for their after-hours advice and guidance in helping me become a better instructor and graduate student.

I am blessed to have a large family, and I would like to take the time here to express my love and gratitude to them all. To David, Sharon, Carl, and Mary Lehtonen, I would like to thank you all for being a source of love, support, and encouragement throughout the years. You helped to quickly transform Austin into a home for me, and it never would have been the same without you all. My cousin Lauren Lehtonen is the closest thing I have to a sibling, and I am glad that we were able to grow closer during my time in Texas. To my grandparents, David and Joyce Lehtonen, thank you for your love, support, and encouragement in me chasing my dreams; I am glad that I was able to make you proud. To my aunt, Lisa Lehtonen; thank you for being a part of my life, coming to my wedding, and welcoming Ashley to the family with open arms. To my family I left behind in Arizona; thank you all for making every visit back home feel as though I had never left. Thank you especially to Gayle Sipe and Brandon West for taking the time to fly to Austin for my wedding; I will never forget it. To my grandparents Van and Delores West, and Irene Lehtonen; thank you for the values you passed on to me, including the value of education. It is because of their many sacrifices that I am able to stand on their shoulders and write these words today.

I have been blessed to have been able to keep close contact with many old friends throughout the years, and I would like to thank them all here. Thank you in particular to Matthew Herlihy, Tarif Abedin, Dan Wanegar, Andrew Friedman, Peter Clark, and Matthew Lehrman for coming to my wedding from all across the continent, including across international borders. I am humbled that I managed to foster such feelings of love and loyalty from you all, and I am glad to count you among my family.

To Kyle Hollingshead, my closest friend across the last decade: through a series of mishaps and odd coincidences, I have been able to stay incredibly close to you and Fran from grades 11 to 21. You have been a source of stability through these years, and I am glad to have a friend as close as you. Thank you for all your years of support and advice; even though I don't always follow it, I value your opinion above most others.

I am fortunate to have added new family members as well during my studies, and I would like to thank my new parents Kevin and Vicki Hill, along with my new siblings Dan and Paige Hill. Thank you for all you have done to support me these last few years, and the trust you have placed in me with regards to your daughter/sister. I am proud to have joined your family.

I would like to thank my parents as well for everything they have done for me in the past, and will do for me in the present. It is because of them, and their never-ending love, support, and guidance that I have survived these last five years, along with the previous twenty-two. Thank you for helping prepare me to achieve in life, including learning when to relax.

Last, but foremost, I would like to thank my wife, Ashley. If it were not for her, I would not have been able to make it this far in my career. Thank you for your endless love and support for me to chase my dreams, as well as taking a chance on that strange graduate student auditing Transport Phenomena four years ago. Of all of the things that have happened to me in the last five years, including this degree, you were by far the best and most significant. Thank you for everything you have done and continue to do, and I hope that I can continue to make you proud and happy for all the years to follow.

Low Thermal Expansion Transition Metal Oxides for Reduced Temperature Solid Oxide Fuel Cell Cathodes

Matthew David West, Ph.D.

The University of Texas at Austin, 2014

Supervisor: Arumugam Manthiram

Solid oxide fuel cells (SOFCs) are power generation devices that offer many great advantages compared to lower temperature fuel cells; for example, they are able to operate at high efficiencies without the use of expensive precious metal catalysts, and are also able to directly utilize hydrocarbon fuels without the need of an external reformer. Unfortunately, the conventional high operating temperature of these devices ($T \approx 1000$ °C) requires the use of expensive, specialized materials that can withstand these high temperatures. This issue has generated considerable interest in reducing the operating temperature of these devices to the intermediate-temperature (600 – 800 °C) to allow for the use of less-expensive materials, such as stainless steel. However, the conventionally utilized SOFC cathode materials exhibit poor electrochemical performance at these reduced temperatures. Currently considered alternative intermediate temperature cathodes, such as $Ba_{0.5}Sr_{0.5}Co_{0.8}Fe_{0.2}O_{3-\delta}$ (BSCF), offer improved performance, but have a large thermal expansion coefficient (TEC), leading to cell failure. In light of these issues, this dissertation focuses on the development of low TEC cathodes for intermediate temperature SOFCS (IT-SOFCs).

The primary focus of this dissertation is on the *swedenborgite*-type $RBaCo_3MO_{7+\delta}$ (R = Y, In, and Ca; M = Zn and Fe) series of cathodes. Due to their tetrahedrally-coordinated M site, the cobalt ions in these materials do not undergo a spin-state transition, and have TECs similar to conventional SOFC electrolyte materials. The long-term phase stability of these materials was addressed, and it was discovered that a slight In substitution significantly promoted phase stability. In the $Y_{1-x}In_xBaCo_3ZnO_{7+\delta}$ series, it was observed that x = 0.1 successfully stabilized the phase without observable degradation of performance. Similarly, a high-Ca content material ($Y_{0.5}In_{0.1}Ca_{0.4}BaCo_3ZnO_{7+\delta}$) was successfully stabilized, though Ca is known to destabilize the phase; furthermore, this compound showed improved performance compared to $YBaCo_3ZnO_{7+\delta}$. Lastly, the replacement of the performance-inhibiting Zn with Fe was investigated, and the $Y_{0.9}In_{0.1}BaCo_3Zn_{0.6}Fe_{0.4}O_{7+\delta}$ sample showed low temperature performance rivaling BSCF. Other work in this dissertation focuses on the application of functional silver materials for use in SOFCs, with good performance; these materials were easily manufactured, and they showed performance drastically greater than the conventionally utilized platinum.

`

Table of Contents

List of Tables xiv

List of Figures xv

Chapter 1

Introduction..1

1.1 FUEL CELLS 1

1.2 SOLID OXIDE FUEL CELLS 2

1.2.1 Principles of SOFC Operation 2

1.2.2 Electrochemistry and Thermodynamics of SOFC Operation 4

1.2.3 Advantages and Challenges of SOFCs 7

1.3 SOLID OXIDE FUEL CELL COMPONENTS 8

1.3.1 Electrolytes 9

1.3.2 Electrodes..12

1.4 MOTIVATION AND OBJECTIVE 15

Chapter 2

Experimental Methods..19

2.1 MATERIALS SYNTHESIS 19

2.2 MATERIALS CHARACTERIZATION 20

2.2.1 X-ray Diffraction 20

2.2.2 Iodometric Titration 21

2.3 THERMAL ANALYSIS 21

2.3.1 Thermogravimetric Analysis 21

2.3.2 Thermal Expansion 22

2.3.2 Electrical Conductivity 22

2.4 ELECTROCHEMICAL ANALYSIS 24

`

2.4.1 Materials Processing 24
2.4.2 Electrochemical Impedance Analysis 24
2.4.3 Microstructural Analysis 25

Chapter 3

Effects of In Substitution in $Y_{1-x}In_xBaCo_3ZnO_{7+\delta}$ ($0 \leq x \leq 0.5$) Cathodes for Intermediate Temperature Solid Oxide Fuel Cells 26

3.1 INTRODUCTION 26
3.2 EXPERIMENTAL METHODS 28
3.3 RESULTS AND DISCUSSION 32
  3.3.1 Crystal Chemistry and Phase Stability 32
  3.3.2 Thermal Expansion and Oxygen Content 38
  3.3.3 Symmetric Cell Optimization and Electrochemical Performances 42
3.4 CONCLUSIONS 55

Chapter 4

Improved Phase Stability and Electrochemical Performance of $(Y,In,Ca)BaCo_3ZnO_{7+\delta}$ Cathodes for Intermediate Temperature Solid Oxide Fuel Cells 56

4.1 INTRODUCTION 56
4.2 EXPERIMENTAL METHODS 57
  4.2.1 Materials Synthesis 57
  4.2.2 Material Characterization 58
  4.2.3 Electrochemical Characterization 58
4.3 RESULTS AND DISCUSSION 59
  4.3.1 Phase Stability and Crystal Chemistry 59
  4.3.2 Thermal Properties and Electrochemical Performance 64
4.4 CONCLUSIONS 76

`

Chapter 5

High-Performance $Y_{0.9}In_{0.1}BaCo_3(Zn,Fe)O_{7+\delta}$ Swedenborgite-Type Oxide Cathodes for Reduced Temperature Solid Oxide Fuel Cells.....................................78

5.1 INTRODUCTION 78

5.2 EXPERIMENTAL METHODS...80

5.2.1 Materials Synthesis 80

5.2.2 Materials Characterization 80

5.2.3 Electrochemical Characterization 81

5.3 RESULTS AND DISCUSSION..82

5.3.1 Crystal Chemistry and Phase Stability..82

5.3.2 Thermal Properties and Electrochemical Performance...............88

5.4 CONCLUSIONS...98

Chapter 6

Layered $LnBa_{1-x}Sr_xCoCuO_{5+\delta}$ (Ln = Nd and Gd) Perovskite Cathodes for Intermediate Temperature Solid Oxide Fuel Cells.....................................99

6.1 INTRODUCTION 99

6.2 EXPERIMENTAL METHODS...100

6.3 RESULTS AND DISCUSSION..103

6.3.1 Crystal Chemistry 103

6.3.2 Thermal and Electrical Properties...109

6.3.3 Electrochemical Properties 118

6.4 CONCLUSIONS..124

Chapter 7

Synthesis Method for 3-Dimensional Silver Networks and their Application in Solid Oxide Fuel Cells...126

7.1 INTRODUCTION 126

7.2 EXPERIMENTAL METHODS...128

`

7.3 RESULTS AND DISCUSSION 130
7.3.1 Materials Processing and Effect on Microstructure 130
7.3.2 Materials Stability in Solid Oxide Fuel Cell Environments 133
7.3.3 Electrochemical Performance as a Cathode Material for SOFC 136
7.4 CONCLUSIONS..141

Chapter 8

Summary..143

List of Publications Related to this Work 150

References..151

`

List of Tables

Table 3.1: Structural and thermal expansion parameters of $Y_{1-x}In_xBaCo_3ZnO_{7+\delta}$ oxides 36

Table 3.2: Electrochemical performance data of the $Y_{1-x}In_xBaCo_3ZnO_{7+d}$ + GDC symmetric cells 49

Table 4.1: Unit cell parameters and activation energies of the (Y,In,Ca)$BaCo_3ZnO_{7+\delta}$ oxides and composite cathodes....................64

Table 4.2: Oxygen contents and Co oxidation states of the (Y,In,Ca)$BaCo_3ZnO_{7+\delta}$ oxides 67

Table 5.1: Unit cell parameters, high temperature phase stability, and activation energies of the $Y_{0.9}In_{0.1}BaCo_3Zn_{1-x}Fe_xO_{7+\delta}$ oxides and composite cathodes....................84

Table 5.2: Oxygen contents of the $Y_{0.9}In_{0.1}BaCo_3Zn_{1-x}Fe_xO_{7+\delta}$ oxides....................85

Table 6.1: Structural and compositional parameters of $LnBa_{1-x}Sr_xCoCuO_{5+\delta}$ (Ln = Nd and Gd) oxides 107

Table 6.2: Variations in oxygen content values as measured by titration and TGA of $LnBa_{1-x}Sr_xCoCuO_{5+\delta}$ (Ln = Nd and Gd 112

Table 6.3: Maximum power density, TEC, and electrical conductivity of selected cathode materials 115

`

List of Figures

Figure 1.1: Schematic of a H_2-fuelled SOFC in operation, including electrode half-reactions 3

Figure 1.2: General example of a SOFC current-voltage (IV) curve 7

Figure 1.3: Cross-sectional SEM micrograph of an anode-supported single cell. Note the large porous anode, the dense, thin electrolyte layer, and the thin porous cathode layer 9

Figure 1.4: Total electrical conductivity in air of well-studied SOFC electrolytes as a function of temperature 12

Figure 2.1: Schematic of the Van der Pauw setup, where I is the current source, V is the voltage receiver, and numbers 1-4 are the sample contacts........23

Figure 3.1: Room-temperature XRD patterns of the as-synthesized $Y_{1-x}In_xBaCo_3ZnO_{7+\delta}$ $(0 \leq x \leq 0.5)$ samples before long-term stability testing 32

Figure 3.2: Room-temperature oxygen contents and lattice parameter values of $Y_{1-x}In_xBaCo_3ZnO_{7+\delta}$ $(0 \leq x \leq 0.5)$ 33

Figure 3.3: Room-temperature XRD patterns of the $Y_{1-x}In_xBaCo_3ZnO_{7+\delta}$ $(0 \leq x \leq 0.5)$ samples after 120 h exposure to temperatures of 600, 700, and 800 °C. Peaks marked with * denote $BaCoO_{3-\delta}$ phase formed due to decomposition 37

Figure 3.4: Thermal expansion behaviors of $Y_{1-x}In_xBaCo_3ZnO_{7+\delta}$ oxides 39

Figure 3.5: TGA plots displaying the oxygen content variations of the $Y_{1-x}In_xBaCo_3ZnO_{7+\delta}$ oxides: (a) full curve of $YBaCo_3ZnO_{7+\delta}$ vs. temperature as an example, (b) oxygen content of the samples with time after the 15 h dwell at 900 ^{o}C, and (c) final cooling curves of the samples..41

Figure 3.6: Area-normalized AC impedance spectra of $YBaCo_3ZnO_{7+\delta}$ + GDC symmetric cells with varying current collectors: (a) undiluted silver dots, (b) dilute screen-printed silver paste, (c) screen-printed silver paste with dispersant, and (d) pristine $YBaCo_3ZnO_{7+\delta}$ 44

Figure 3.7: SEM micrographs of the various silver current collectors: (a) undiluted silver dots, (b) dilute screen-printed silver paste, and (c) screen-printed silver paste with dispersant 45

Figure 3.8: SEM micrographs displaying the microstructure of the microscale mesh resulting from screen-printing and heat treating the dispersed silver paste. Images (a) and (b) both show the same section of mesh at different magnifications. Image (c) is included to feature the grade of the mesh. These images show the degree of interconnectivity and strength of the current collector, while featuring pore sizes below 10 microns..46

Figure 3.9: Arrhenius plots of the $Y_{1-x}In_xBaCo_3ZnO_{7+\delta}$ + GDC symmetric cells in the range of 600 – 800 °C 48

Figure 3.10: SEM micrographs of the $Y_{1-x}In_xBaCo_3ZnO_{7+\delta}$ + GDC symmetric cells (whose performance values can be seen in Figure 9) after testing ...49

Figure 3.11: Nyquist plots providing the effects of the microstructure of the $YBaCo_3ZnO_{7+\delta}$ + GDC symmetric cells on 8YSZ electrolytes, showing the impedance with (a) GDC synthesized by solid-state reaction, (b) GDC synthesized by GNP, and (c) GDC synthesized by GNP with 5 wt. % graphite as pore former. Note that the 800 °C plots use a Bézier curve fitting to reduce signal noise 51

Figure 3.12: (a) Arrhenius plots of $YBaCo_3ZnO_{7+\delta}$ + GDC (made by solid-state reaction and labeled here as YBC3Z), BSCF, and BSCF + GDC symmetric cells on 8YSZ electrolytes in the range of 400 – 800 °C. (b) Nyquist plots of all three cells at 600 °C with the equivalent circuit used to generate the fitted data 53

Figure 3.13: Nyquist plots comparing (a) BSCF, (b) $YBaCo_3ZnO_{7+\delta}$ + GDC, and (c) BSCF + GDC symmetric cells on GDC electrolyte in the range of 400 – 600 °C 54

Figure 4.1: Room-temperature XRD patterns of the as-synthesized $(Y,In,Ca)BaCo_3ZnO_{7+\delta}$ samples before long-term stability testing..60

Figure 4.2: Room-temperature XRD patterns of the $(Y,In,Ca)BaCo_3ZnO_{7+\delta}$ samples after 120 h exposure to 600, 700, and 800 °C. No impurity phases were detected in any sample after long-term exposure 63

Figure 4.3: TGA plots detailing the oxygen content variations of the as-synthesized (Y,In,Ca)$BaCo_3ZnO_{7+\delta}$ oxides: (a) full curve of $Y_{0.8}In_{0.1}Ca_{0.1}BaCo_3ZnO_{7+\delta}$ as an example, (b) final cooling curve of the high-In samples, and (c) final cooling curve of the high-Ca samples. All samples were allowed to anneal 15 h in air, as seen in (a). Figure 4.3a also defines three points along the curve that are used in Table 4.2: (1) is the room-temperature point, (2) is the TGA-dwell point, and (3) is the final-cool point........66

Figure 4.4: Arrhenius plots of the (Y,In,Ca)$BaCo_3ZnO_{7+\delta}$ + GDC symmetric cells on 8YSZ electrolyte in the range of 400 – 800 °C: (a) Arrhenius plots of the high-In samples, (b) Arrhenius plots of the high-Ca samples, and (c) Arrhenius plots comparing $Y_{0.8}In_{0.1}Ca_{0.1}BaCo_3ZnO_{7+\delta}$ with the undoped $YBaCo_3ZnO_{7+\delta}$ for a comparison........71

Figure 4.5: Arrhenius plots of $Y_{0.8}In_{0.1}Ca_{0.1}BaCo_3ZnO_{7+\delta}$ + GDC, $Y_{0.5}In_{0.4}Ca_{0.1}BaCo_3ZnO_{7+\delta}$ + GDC, and $Y_{0.5}In_{0.1}Ca_{0.4}BaCo_3ZnO_{7+\delta}$ + GDC symmetric cells on GDC electrolyte in the range of 400 – 800 °C. The $Y_5In_1Ca_4$ sample shows improved performance at all temperatures, particularly below 600 °C........73

Figure 4.6: Nyquist plots of the (a) $Y_{0.8}In_{0.1}Ca_{0.1}BaCo_3ZnO_{7+\delta}$ + GDC, (b) $Y_{0.5}In_{0.4}Ca_{0.1}BaCo_3ZnO_{7+\delta}$ + GDC, and (c) $Y_{0.5}In_{0.1}Ca_{0.4}BaCo_3ZnO_{7+\delta}$ + GDC symmetric cells on GDC electrolyte. Frequency markers are included for the $Y_{0.8}In_{0.1}Ca_{0.1}BaCo_3ZnO_{7+\delta}$ + GDC sample at all temperatures........74

Figure 4.7: SEM micrographs of the (Y,In,Ca)$BaCo_3ZnO_{7+\delta}$ + GDC symmetric cells on GDC electrolyte after testing (tests may be seen in Figures 4.5 and 4.6) 75

Figure 5.1: Room-temperature XRD patterns of selected as-synthesized $Y_{0.9}In_{0.1}BaCo_3Zn_{1-x}Fe_xO_{7+\delta}$ oxides before long-term stability testing. All samples with $x < 0.8$ are single-phase oxides with the *P31c* space group. The * in the x = 0.9 and 1.0 samples denote impurity phases 83

Figure 5.2: Room-temperature XRD patterns of the $Y_{0.9}In_{0.1}BaCo_3Zn_{1-x}Fe_xO_{7+\delta}$ ($0 \leq x \leq 0.8$) oxides after 120 h exposure to 600, 700, and 800 °C. The * in the x = 0.4 sample at 700 °C denote the generated $BaCoO_3$ impurity. The impurities generated in the x = 0.6 and 0.8 samples at 700 and 800 °C are unidentified due to the severity of the phase decomposition 87

Figure 5.3: Variations in oxygen content as observed via TGA of all the single-phase $Y_{0.9}In_{0.1}BaCo_3Zn_{1-x}Fe_xO_{7+\delta}$ ($0 \leq x \leq 0.8$) oxides: (a) full trace of the x = 0.4 sample for a reference, with the arrows denoting directionality; (b) oxygen content with time after 15 h annealing at 900 °C; and (c) final cooling curve of all samples to 80 ^{o}C 90

Figure 5.4: Arrhenius plots in the range of 400 – 800 °C of (a)$Y_{0.9}In_{0.1}BaCo_3Zn_{1-x}Fe_xO_{7+\delta}$ ($0 \leq x \leq 0.4$) + GDC composite cathodes and (b) $Y_{0.9}In_{0.1}BaCo_3Zn_{0.6}Fe_{0.4}O_{7+\delta}$ + GDC composite cathode compared to the single-phase BSCF. All samples were measured on 8YSZ electrolyte-supported symmetric cells. Activation energies were calculated from the best-fit lines in the range of 433 – 766 °C and are listed in Table 5.1 93

Figure 5.5: Area-normalized Nyquist plots of the $Y_{0.9}In_{0.1}BaCo_3Zn_{1-x}Fe_xO_{7+\delta}$ + GDC composite cathodes on 8YSZ electrolyte-supported symmetric cells: (a) x = 0, (b) x = 0.2, and (c) x = 0.4 95

Figure 5.6: Cross-sectional SEM micrographs of the $Y_{0.9}In_{0.1}BaCo_3Zn_{1-x}Fe_xO_{7+\delta}$ + GDC composite cathodes on 8YSZ electrolyte-supported symmetric cells after testing. Performances of these cells are presented in Figures 5.4 and 5.5 96

Figure 5.7: Symmetric cell tests comparing $Y_{0.9}In_{0.1}BaCo_3Zn_{0.6}Fe_{0.4}O_{7+\delta}$ composite cathodes with both GDC synthesized by solid state reaction and by GNP on GDC electrolyte supports. (a) Arrhenius plots of polarization resistance in the range of 400 – 800 °C, and (b) Nyquist plots of these cells at 500 °C 97

Figure 6.1: Room temperature XRD patterns of the successfully synthesized (a) $NdBa_{1-x}Sr_xCoCuO_{5+\delta}$ and (b) $GdBa_{1-x}Sr_xCoCuO_{5+\delta}$ samples 104

Figure 6.2: Room temperature XRD patterns of intended (a) $NdSrCoCuO_{5+\delta}$ and (b) $GdSrCoCuO_{5+\delta}$. Peaks marked with * belong to unidentified impurity phases 105

Figure 6.3: Observed and calculated XRD profiles, the differences between them, and peak positions for $GdBa_{0.5}Sr_{0.5}CoCuO_{5+\delta}$. The quality of refinement was found to be $\chi^2 = 3.36$ and $R_{bragg} = 4.94$ 106

Figure 6.4: TGA plot of $NdBa_{0.75}Sr_{0.25}CoCuO_{5+\delta}$, illustrating the variations on oxygen content during heating and cooling 110

`

Figure 6.5: Variations in the oxygen content with temperature of the $LnBa_{1-x}Sr_xCoCuO_{5+\delta}$ samples in air: (a) x = 0.0, (b) x = 0.25, (c) x = 0.50, and (d) x = 0.75. Measurements were taken during heating of the samples 111

Figure 6.6: Thermal expansion (dL/L_0) curves in air of the $LnBa_{1-x}Sr_xCoCuO_{5+\delta}$ samples: (a) x = 0.0, (b) x = 0.25, (c) x = 0.50, and (d) x = 0.75. L_0 is the initial length of the sample pellet..114

Figure 6.7: Variations of the electrical conductivity with temperature of (a) $NdBa_{1-x}Sr_xCoCuO_{5+\delta}$ and (b) $GdBa_{1-x}Sr_xCoCuO_{5+\delta}$ in air, measured with a 4 probe Van der Pauw setup 117

Figure 6.8: Variations of the conductance (R_p^{-1}) with temperature of the (a) $NdBa_{1-x}Sr_xCoCuO_{5+\delta}$ and (b) $GdBa_{1-x}Sr_xCoCuO_{5+\delta}$ cathodes with temperature in air, as measured with an LSGM-supported symmetrical cell by ac-impedance spectroscopy 120

Figure 6.9: Comparison of the electrochemical performance data of (a) $GdBaCoCuO_{5+\delta}$, (b) $GdBa_{0.25}Sr_{0.75}CoCuO_{5+\delta}$, and (c) $NdBa_{0.25}Sr_{0.75}CoCuO_{5+\delta}$ cathodes in the range of 700 – 800 °C with an electrolyte supported single cell...123

Figure 6.10: SEM micrographs showing the cross sections of the (a) LSGM dense electrolyte and (b) cathode | cathode + LSGM | LSGM portion of the $GdBaCoCuO_{5+\delta}$ single cells. Images were taken after the measurement of single cell performance. Cathode particles in the dense electrolyte region in both images are due to fracturing of the cell after measurement 124

Figure 7.1: XRD data of the as-synthesized Ag_2O powders after washing with de-ionized water and drying overnight. The peaks marked with an * refer to trace amounts of Ag metal contaminants from the drying process.131

Figure 7.2: SEM micrographs of as-synthesized Ag network. All samples were made from the same ink (50 : 50 weight ratio), but were sintered at different temperatures. 133

Figure 7.3: Cross-sectional SEM micrographs of the cells shown in Figure 7.2. 133

Figure 7.4: SEM micrographs showing the results of the Ag current collector of a SOFC single cell on the (a) air-exposed cathode side and (b) the hydrogen-exposed anode side. The cathode side current collector wire shows no damage, while the anode side wire shows remarkable pitting and grain boundary fractures resulting in total cell failure. 135

Figure 7.5: SEM micrographs of two Ag disks after heat treatment in different atmospheres: (a) an Ag disk that was exposed to 10% H_2 – 90 % Ar atmosphere at a low temperature (~ 25 ^{o}C) before being heated to 900 °C, and (b) an Ag disk that was exposed to N_2 atmosphere at 900 °C for 2 h before being exposed to 10% H_2 – 90 % Ar. 136

Figure 7.6: Nyquist plots recorded at 600 °C of two electrolyte-supported symmetric cells with an Ag cathode sintered at two different temperatures: (a) impedance spectrum of the symmetric cell sintered at 600 °C and (b) impedance spectrum of the symmetric cell sintered at 800 °C. Both symmetric cells were manufactured with the same starting material138

Figure 7.7: Nyquist plots recorded at 600 °C of symmetric cells manufactured from commercially available Ag and Pt pastes: (a) comparison between Ag and Pt inks sintered at 800 °C and (b) comparison between the Pt cell in Figure (a) and another cell sintered at 1500 °C 140

Figure 7.8: SEM micrographs detailing the differences in the microstructures of two cathodes manufactured with commercially available Pt inks: (a) sintered at 800 °C and (b) sintered at 1500 °C. The performance of these cathodes can be seen in Figure 7.7..141

`

CHAPTER 1

Introduction

1.1 FUEL CELLS

Fuel cells are electrochemical energy generation devices that directly convert chemical energy to electrical energy. This direct utilization of chemical energy allows for the bypass of the Carnot cycle, which is a significant limitation on traditional combustion based power generation devices.[1] Traditional combustion based fossil fuel power plants operate at an average of ~30% fuel to electricity efficiency. Fuel cells, on the other hand, can readily operate at efficiencies greater than 50%, due to the removal of the mechanical energy losses.[1] There are a wide variety of fuel cells, each offering unique benefits and challenges. The polymer electrolyte fuel cell, for example, may operate at near-ambient temperatures (< 100 °C), but require extremely pure hydrogen fuel and expensive platinum catalysts.[1-4] The phosphoric acid fuel cell, on the other hand, operates at elevated temperatures (~200 °C), which allows for both elevated efficiencies and a greater tolerance towards contaminants, but unfortunately still relies on a platinum catalyst. This reliance on expensive catalysts is a significant limitation towards the increased adoption and commercialization of fuel cell technologies; however, with increasing environmental concerns and decreasing availability of traditional fossil fuels, there is a significant effort to address these challenges.

`

1.2 SOLID OXIDE FUEL CELLS

Similar to other fuel cell technologies, solid oxide fuel cells (SOFCs) are electrochemical energy conversion devices that directly convert fuel to electricity. SOFCs are completely solid-state devices that utilize ceramic electrolytes with ceramic or cermet (ceramic-metallic) electrodes.[4-6] SOFCs have some unique benefits when compared to alternative fuel cell technologies; for example, they are able to utilize both hydrogen or hydrocarbon based fuels, and are able to operate with less expensive transition-metal based catalysts. Traditionally, SOFCs operate with O^{2-} conducting ceramic electrolytes, but there has been recent work to create protonic ceramic fuel cells (PCFCs) that utilize H^+ conducting electrolytes.[7-11] In order to achieve adequate catalytic activity and ionic transport in SOFCs involving oxide-ion conductors, however, an increased operating temperature of > 500 °C is traditionally required.

1.2.1 Principles of SOFC Operation

Figure 1.1 illustrates the operation schematic of a hydrogen fueled SOFC based on an oxide-ion electrolyte. Hydrogen is fed to the anode side, which is oxidized to produce H^+, and the resultant electrons are fed through the external circuit to power a load, producing electrical work. At the cathode, the supplied oxygen is reduced by these electrons to generate O^{2-} ions. These oxide ions are then conducted through the solid electrolyte to the anode, where they combine with the previously generated H^+ ions to

`

generate water. Overall, the supplied reactants are H_2 and O_2, and the products are H_2O and heat.

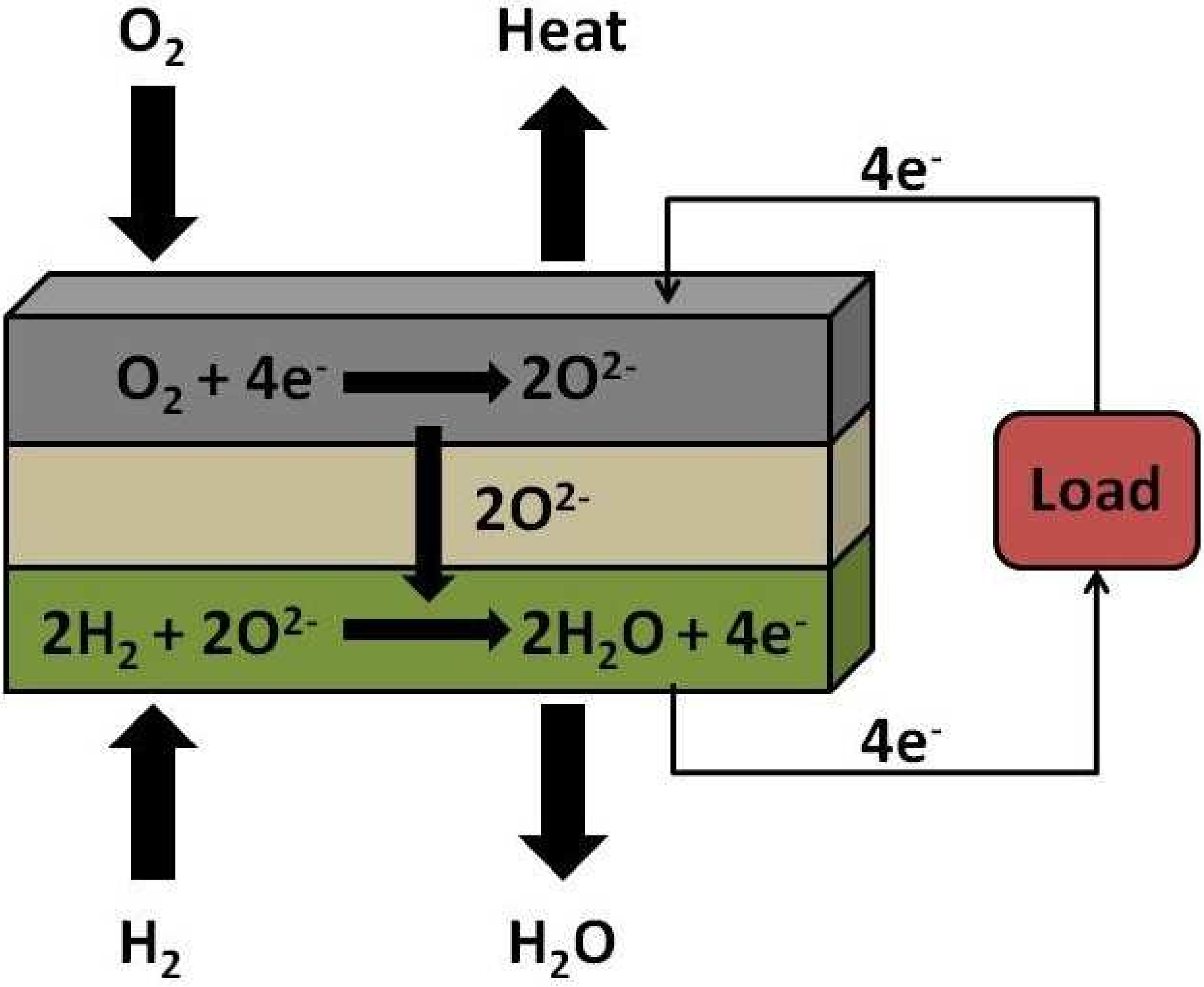

Figure 1.1 Schematic of a H_2-fuelled SOFC in operation, including electrode half-reactions

`

These reactions are dependent on their active surface area; as such, both electrodes utilize a porous structure to increase the solid-gas boundary region. In contrast, a dense electrolyte is utilized to create a barrier between fuel and oxidant to prevent their direct mixing and internal electrical short.

1.2.2 Electrochemistry and Thermodynamics of SOFC Operation

As stated previously, the overall chemical reaction for traditional hydrogen-fuelled SOFC operation is as follows:

$$H_2 + 2\ O_2 = 2\ H_2O \tag{1.1}$$

If the Gibbs free energies of the reactants are greater than that of the products (*i.e.* the change in free energy is negative), the reaction can be said to be spontaneous. In this case, the overall Gibbs free energy of reaction ($\Delta G_{f,rxn}$) is given as

$$\Delta G_{f,rxn} = 2\ G_{f,H_2O(g)} - (2\ G_{f,H_2} + G_{f,O_2}) \tag{1.2}$$

where $G_{f,H_2O(g)}$, G_{f,H_2}, and G_{f,O_2}refer to the Gibbs free energy of formations of gaseous water, hydrogen, and oxygen, respectively. The Gibbs free energies vary corresponding to the conditions of the reaction, but at standard conditions, the overall change in the energy of the reaction is -237.3 kJ mol^{-1}.[1] If the entire change in free energy is converted to electrical energy, the equation can be given as

$$\Delta G^0{}_{f,rxn} = -nFE^0 \tag{1.3}$$

`

where n is the number of electrons involved in the reaction, F is the Faraday constant, and E^0 is the standard potential. E^0, in this case, is 1.23 V for the reaction listed in Eq. (1.1). However, this reversible standard potential varies with real conditions, and is described by the Nernst equation[12,13] as

$$E = E^0 - \frac{RT}{nF}\ln(Q) \qquad (1.4)$$

where R is the gas constant, T is the absolute pressure, and Q is the reaction quotient, defined as

$$Q = \frac{\prod_j {p_j}^{v_j}}{\prod_i {p_i}^{v_i}} \qquad (1.5)$$

where the numerator is the product of the partial pressure of the products (p_j) raised to the power of their stoichiometric coefficients (v_j); the denominator refers to the same, but for the reactants. In terms of the standard cell described in Eq. (1.1), this simplifies to

$$Q = \frac{p_{H_2O}}{P_{H_2} * {P_{O_2}}^{1/2}} \qquad (1.6)$$

These series of equations can not only be used for the standard cell at standard conditions, but can also be used to define fuel cells operating at SOFC temperatures and utilizing hydrocarbon fuels.

The real-world performance of SOFCs can deviate rather significantly from the theoretical model. This difference between the theoretical cell potential and the actual cell potential is defined as the over-potential or polarization (η).[12] This over potential is affected by many different aspects of SOFC operation and construction, including but not

`

limited to gas flow rates, operating temperature, and choice of cell materials. A representative current-voltage curve can be seen in Figure 1.2.[14] As current is drawn from the cell in operation, the potential of the cell decreases. The overall polarization loss can be broken into three separate factors: (1) the activation polarization from the electrochemical reaction kinetics (η_{act}), (2) the Ohmic polarization from the internal resistances of the materials to electronic and ionic conductivity (η_{Ohm}), and (3) the concentration polarization due to the limitations in mass transport in the supply of oxidant and fuel to the electrodes at high current drain (η_{con}).[1,4,15] Therefore, the total polarization in the fuel cell can be defined as the sum of the three components as

$$\eta_{T} = \eta_{act} + \eta_{Ohm} + \eta_{con} \tag{1.7}$$

`

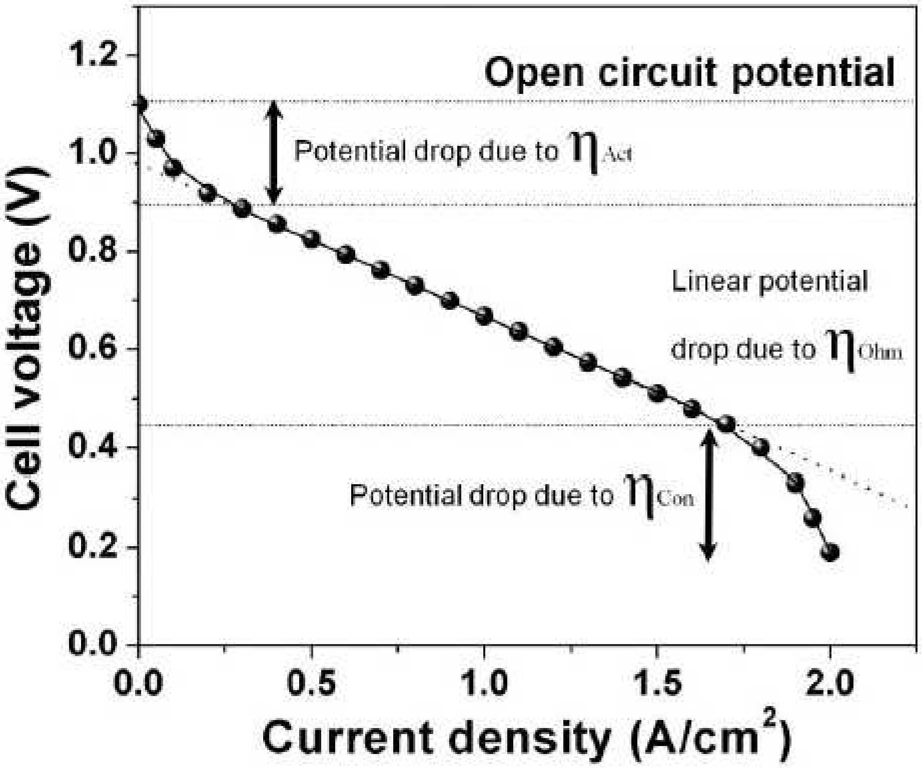

Figure 1.2 General example of a SOFC current-voltage (IV) curve.[14]

1.2.3 Advantages and Challenges of SOFCs

In contrast to some of the fuel cells mentioned previously, the high operating temperatures of SOFCs produces both positive and negative qualities. As for the advantages, they include, but are not limited to the following:[4-6,15-18]

- Use of inexpensive electrode catalysts such as Ni, Fe, and Co
- Fuel flexibility, as SOFCs can utilize hydrogen or hydrocarbon fuels without the need for external reformation

`

- Extremely high efficiencies (> 80%) when utilized in a combined heat and power setup
- Reduction in CO_x, SO_x, and NO_x per kWh through improved fuel efficiencies

Similarly, SOFCs have challenges to overcome in order to reach widespread commercialization and utilization:

- Chemical and mechanical instability of traditional materials due to the elevated operating temperatures (T > 800 °C)
- Inadequate catalytic and transport activity of traditional SOFC materials in the intermediate-temperature (IT) range of 600 – 800 °C
- Large thermal expansion coefficients (TEC) of traditional SOFC cathodes, resulting in TEC mismatch and delamination between other SOFC components
- Coking and sulfur problems at the anode site with conventional Ni-based anodes directly utilizing hydrocarbon fuels
- Chromium poisoning of many traditional SOFC cathodes, necessitating the use of expensive interconnect materials

1.3 SOLID OXIDE FUEL CELL COMPONENTS

Solid oxide fuel cells consist of four primary components; two porous electrodes (anode and cathode), a dense electrolyte layer, and electrical interconnects (or current collectors). All components should have good chemical and mechanical stability with each other for long-term stability during operation and thermal cycling. A cross-sectional SEM micrograph of an anode-supported SOFC can be observed in Figure 1.3.

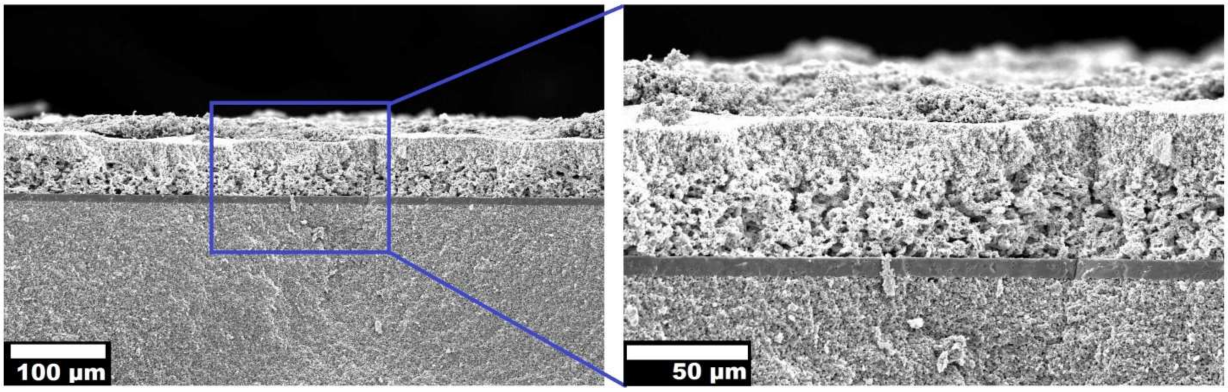

Figure 1.3 Cross-sectional SEM micrograph of an anode-supported single cell. Note the large porous anode, the dense, thin electrolyte layer, and the thin porous cathode layer.

1.3.1 Electrolytes

In order to be used as an electrolyte in an SOFC, a material must possess certain properties. First, the material must be stable in both fuel and oxidant atmospheres as the electrolyte acts as the barrier between both atmospheres; similarly, the material must not react with the adjoining electrodes. Secondly, the electrolyte must be electrically insulating to prevent a short and the bypassing of the external circuit. The electrolyte material must also have adequate mechanical properties; it must have good mechanical strength at operating temperatures and have thermal expansions that closely match the

`

rest of the cell components. Lastly, the electrolyte must have high ionic conductivity; traditional SOFCs have been based around oxide-ion conductive electrolytes, but recent work has shown promise for proton-conducting ceramic electrolyte materials.[7-11] A comparison of oxide-ion conducting electrolyte conductivities can be found in Figure 1.4 at the end of this section.

The first SOFC electrolyte used was yttria-stabilized zirconia (YSZ) in 1937 by Baur and Preis.[18,19] Undoped ZrO_2 undergoes multiple phase transitions upon heating, but the substitution of Y^{3+} for Zr^{4+} stabilizes the material as the desired cubic fluorite phase.[4,20] However, this substitution also reduces the oxygen content of the crystal in order to remain electrically neutral; these oxygen vacancies act as transport vehicles and provide oxide-ion conductivity. There are a wide number of $Zr_{1-x}Y_xO_{2-0.5x}$ compositions used, but one of the most common is 8 mol% YSZ (8YSZ) containing 8 mol % Y_2O_3. YSZ has many attractive properties that have allowed it to remain in widespread use, but it suffers from reduced ionic conductivity at temperatures below 800 °C.[4,15,20-22]

An alternative electrolyte material is the Sr and Mg doped $La_{1-x}Sr_xGa_{1-y}Mg_yO_{3-\delta}$ (LSGM) perovskite. The maximum oxide-ion conductivity of these materials has been reported to occur in the range of $0.1 \leq x \leq 0.2$ and $0.15 \leq y \leq 0.2$; the substitution of Sr^{2+} for La^{3+} and Mg^{2+} for Ga^{3+} create oxygen vacancies that facilitate oxide-ion conduction.[23-26] This material has been shown to have higher ionic conductivity than YSZ at lower temperatures, but this material unfortunately reacts with Ni-based anodes to form undesired impurity phases.[15,27] This shortcoming can be overcome by adding non-

`

reactive barrier layers (generally an alternative electrolyte material) between the anode and LSGM, but this adds to the complexity of the cell and increases the ohmic losses of the cell through an increased electrolyte thickness.

Ceria (CeO_2) based electrolytes are another promising class of alternative electrolytes for use in SOFCs. A wide variety of substitutions for Ce have been investigated, such as Y^{3+} (YDC), La^{3+} (LDC), Gd^{3+} (GDC), and Sm^{3+} (SDC).[15,16] The ionic conductivity is generally maximized with the substitution of Gd or Sm, while other various substitutions can be utilized as buffer layers to prevent side reactions.[16,28,29] These electrolytes are known for their high oxide-ion conductivity in the intermediate temperature range (500 – 800 °C) and are stable with a wide variety of electrode materials.[15,16,30,31] Unfortunately, ceria-based electrolytes are readily reduced in low oxygen partial pressures, creating electronic conductivity and a decrease in efficiency.[32] To overcome this problem, GDC electrolytes are widely used in a bilayer electrolyte configuration, with a thin YSZ layer on the anode-side to prevent reduction.[33,34] Unfortunately, YSZ and GDC are known to react to form impurity phases with reduced ionic conductivity at elevated temperatures.[35-37] However, this problem may be reduced through utilizing low-temperature manufacturing techniques or by doping the GDC with stability-promoting ions.[38]

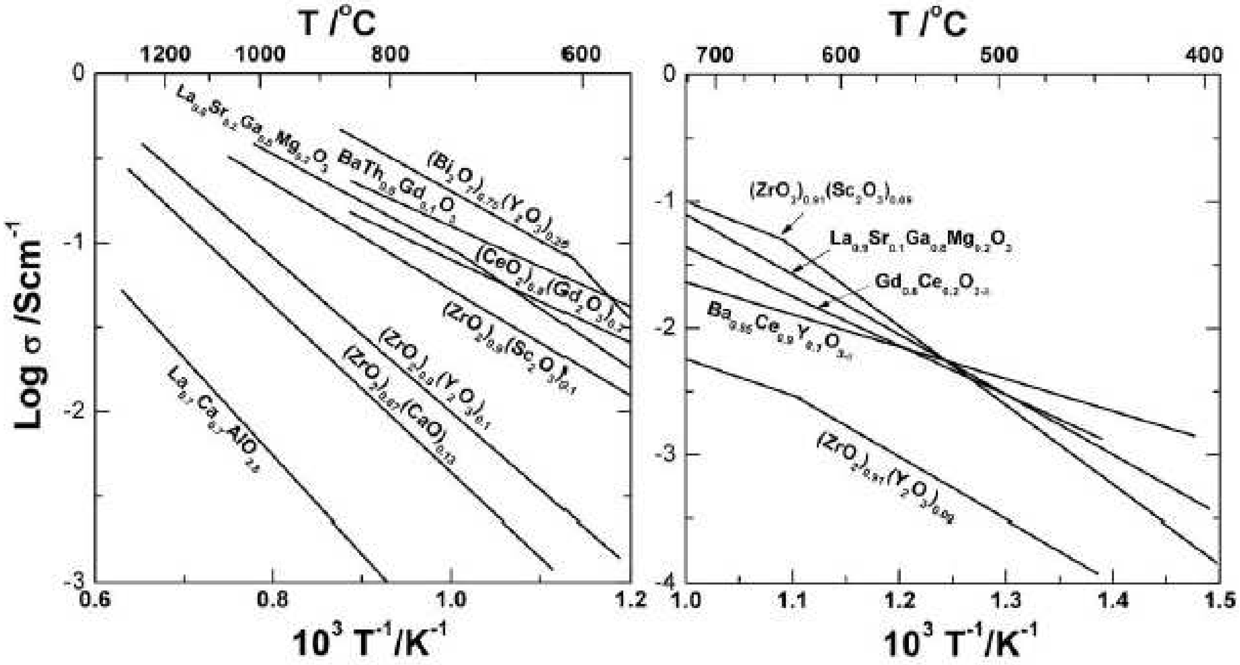

Figure 1.4 Total electrical conductivity in air of well-studied SOFC electrolytes as a function of temperature.[15]

1.3.2 Electrodes

The two electrodes of a SOFC system are the reducing electrode (cathode), and the oxidizing electrode (anode). Both electrodes have some shared requirements for successful application: (1) good chemical stability in their respective atmospheres under load, (2) high catalytic activity for their respective reactions, (3) good chemical and mechanical stability with surrounding cell components, and (4) adequate electronic and ionic conductivities.

Traditionally, anodes for SOFCs are based around cermets made of Ni and electrolyte material (traditionally YSZ or GDC).[1,4,5,15,16,39,40] These cermet composites

`

offer good electronic and oxide ion conductivity, and have good catalytic oxidation of H_2 at operating temperatures. Unfortunately, these materials have significant barriers towards use in hydrocarbon-based fuels, due to sulfur poisoning and carbon deposition.[41-43] Some recent work has shown that the carbon deposition problem may be alleviated through the use of various transition-metal dopants; these dopants act as a catalyst for the oxidation of deposited carbon on the surface to form CO_2.[44,45] Further work on these anodes is required to achieve widespread commercialization.

The most traditional SOFC cathode is arguably Pt, though in more recent years metal oxides have been developed to reduce the cell cost. Perovskite-based systems have been widely investigated in particular due to their tolerance towards cationic substitutions and their ability to hold oxygen vacancies for ionic conductivity.[15,16,28,46-49] One conventionally-utilized perovskite cathode is $La_{1-x}Sr_xMnO_3$ (LSM), which shows favorable oxygen reduction activity at high temperatures and good chemical and mechanical stability with traditional electrolyte materials.[16,50-53] Unfortunately, LSM requires high operating temperatures (800 – 1000 °C) for adequate electrochemical performance; these high temperatures require expensive interconnect materials to avoid thermal degradation, increasing the cost of stack assembly. Due to these problems with elevated operating temperatures, there is a desire to decrease SOFC operating temperature, but unfortunately LSM offers inadequate catalytic activity at reduced temperature, necessitating the development of alternative cathode materials.

One area of investigation has focused on cobalt-containing perovskite materials, such as $La_{1-x}Sr_xCoO_{3-\delta}$ (LSC).[54,55] Due to cobalt's ability to exist as a mixed-valent ion, these perovskites are able to create oxygen vacancies and, therefore, act as mixed ionic and electronic conductors (MIECs). Cobalt also has excellent oxygen reduction reaction capabilities due to the overlap between the $Co^{2+/3+}$ 3d and O^{2-} 2p bands, and, therefore, there have been a wide variety of related perovskites such as the disordered $La_{1-x}Sr_xCoO_{3-\delta}$ (LSC) and the layered $LaBaCo_2O_{5+\delta}$.[56-62] Unfortunately, these materials generally have very large thermal expansion coefficients (TECs) due to the tendency of octahedrally-coordinated Co^{3+} ions to undergo a spin-state transition during thermal cycling; this thermal expansion is significantly greater than the TECs of traditional electrolyte materials, and can cause delamination of the electrodes or cracking of the cell.[63] In order to reduce the large thermal expansion of these materials, attempts to design perovskite cathodes with partial substitutions of other transition metals such as Mn, Fe, Cu, Cr, and Ni have been investigated, with varying degrees of success.[64-66] In particular, iron-substituted perovskites such as $La_{1-x}Sr_xCo_{1-y}Fe_yO_{7+\delta}$ (LSCF) and $Ba_{1-x}Sr_xCo_{1-y}Fe_yO_{7+\delta}$ (BSCF) have been found to have moderate thermal expansion properties, while offering acceptable catalytic activities.[61] In general, it has been observed that the substitution of Co for other transition metals offers reduced thermal expansion behavior, but at the cost of reduced catalytic activity. As such, the development of alternative cathodes with both high catalytic activity and low TEC is an area of immense interest for intermediate temperature SOFCs.

`

Another class of materials that have been investigated for their use as SOFC cathodes are the trigonal *swedenborgite*-type oxides. Initially, these materials were observed as oxygen storage materials, but recent work has shown that, with some modifications, they are capable of acting as SOFC cathodes.[37,67-70] Following a general formula of $RBa(Co,M)_4O_{7+\delta}$ (R = Y, In, and Ca; M = Co, Fe, Zn, Ga, and Al), these materials have been found to offer good catalytic activity for oxygen reduction reaction at temperatures in the range of 600 – 800 °C, and they offer good chemical compatibility with GDC electrolytes.[29,37] One of their main advantages though is that they have TECs that offer excellent matching to other fuel cell components, as the cobalt ions in tetrahedral sites do not undergo a spin-state transition. In these materials, the cobalt ions are tetrahedrally coordinated to the neighboring oxide ions, so the $Co^{2+/3+}$ ions cannot undergo a spin state transition.[37] However, this tetrahedral coordination is unstable for $Co^{2+/3+}$, and these materials have been found to decompose without the addition of stability-promoting ions in the M site like Zn, Ga, and Al.[71,72] These materials also have poor oxide-ion conductivity, and as such are generally mixed with GDC to form a composite cathode to extend the three-phase boundary (TPB). The cathode TPB is defined as the surface area that is shared between the cathode, electrolyte, and oxidant.[73]

1.4 Motivation and Objectives

One significant impetus to the commercialization of solid oxide fuel cells is the high cost associated with the high operating temperature (800 – 1000 °C). However, current high-temperature cathode materials do not perform adequately at intermediate temperatures due to a sluggish oxygen reduction reaction. Current intermediate temperature SOFC (IT-SOFC) cathodes offer excellent performance at reduced temperatures, but they are plagued by large TEC mismatches with the electrolytes. These mismatches cause accelerated stack failure due to delamination and destruction of cathodes after thermal cycling, further increasing the cost per kWh of these materials. As such, IT-SOFC cathodes with reduced thermal expansion coefficient and adequate catalytic activity are required.

As for the *swedenborgite*-type cathodes, these materials offer excellent electrochemical performance and thermal expansion properties, but are observed to decompose after exposure to operating temperatures, making their applications limited.[37,74] Long-term operational stability is paramount to successful commercialization of these devices, and as such, the stability of these materials must be improved. Some initial work on improving the stability of these materials has discovered a generally inverse relationship between stability and performance; for example, replacing $Co^{2+/3+}$ with Zn^{2+} improves long-term stability, but significantly diminishes the electrochemical performance of the cathode. The design of materials with improved stability without greatly sacrificing the performance of these materials is critical for them to be successfully applied as SOFC cathodes.

Overall, the goals of this dissertation are as follows:

`

- Investigate the stability of $RBaCo_3ZnO_{7+\delta}$ (R = Y, In) oxides as IT-SOFC cathodes as well as their electrochemical performance as a function of the three-phase boundary surface area.

- Investigate the performance-boosting substitutions of Ca and Fe of the $RBaCo_3MO_{7+\delta}$ (R = Y, In, Ca; M = Zn, Fe) oxides as IT-SOFC cathodes and the effect of these substitutions on their long-term stability at SOFC operating temperatures.

- Investigate the effects of substituting Sr for Ba in the copper-substituted $LnBa_{1-x}Sr_xCoCuO_{5+\delta}$ (Ln = Nd and Gd); its effect on crystal structure, electrochemical performance, and thermal properties

- Characterization of the synthesized oxides through x-ray diffraction; analysis of their crystal structure in the as-synthesized states and observation of their decomposition products after long-term exposure to SOFC operating temperatures.

- Chemical and thermal analysis of synthesized oxides through wet-chemical analysis, thermogravimetric analysis, thermal expansion measurements, and electron microscopy.

`

- Evaluation of the electrochemical performance of the materials through AC impedance spectroscopy of symmetric cells and electrolyte-supported single cell SOFC performances

`

CHAPTER 2

Experimental Methods

2.1 MATERIALS SYNTHESIS

The primary method for the synthesis of the various cathodes in this dissertation was by conventional solid-state reactions. Required quantities of oxides and carbonates were mixed together before heating at high temperature to complete the reaction. Methods and materials specific to each material system investigated are detailed in the relevant following Chapters.

$Gd_{0.2}Ce_{0.8}O_{1.9}$ (GDC20), $Gd_{0.1}Ce_{0.9}O_{1.95}$ (GDC10), $La_{0.2}Ce_{0.8}O_{1.9}$ (LDC), and $Y_{0.2}Ce_{0.8}O_{1.9}$ (YDC) powders were synthesized by the glycine nitrate process (GNP).[75,76] Required amounts of $Ln(NO_3)_3 \bullet 6H_2O$ (Ln = Y, La, Gd) and $Ce(NH_4)_2(NO_3)_6$ were dissolved in deionized (DI) water with glycine (NH_2CH_2COOH) and heated on a stir plate under agitation until a viscous gel was formed. The stir bar was then removed, and the gel was heated until combustion. The resultant powders were collected and heated in air at 600 °C for 2 h to ensure decarbonation.

GDC20 was also synthesized by conventional solid state reaction. Required amounts of CeO_2 and Gd_2O_3 were ball-milled in ethanol with 1 mol % (metals basis) $Ni(NO_3)_2$ added as a sintering aid, and 1 wt.% binder (Butvar B76).[77,78] The powders were then dried, pressed into pellets, and sintered at 1550 °C for 24 h.

`

The $La_{0.8}Sr_{0.2}Ga_{0.8}Mg_{0.2}O_{2.8}$ (LSGM) electrolyte was prepared by mixing required amounts of La_2O_3, $SrCO_3$, Ga_2O_3 and MgO in an agate mortar and pestle in ethanol, drying and pressing the powder into pellets, and firing at 1100 °C for 5 h. The resultant powder was then ground and ball-milled in ethanol for 48 h, mixed with a binder (Butvar B76) in ethanol, dried, pressed into pellets, and fired at 1500 °C for 10 h.[79]

2.2 MATERIALS CHARACTERIZATION

2.2.1 X-ray Diffraction

The crystal structures of the synthesized materials were analyzed by powder x-ray diffraction (XRD) with Cu K_α radiation at room temperature in air. The equipment used was a Philips Model APD 3520 diffractometer. The resultant patterns were then refined with MDI Jade software and by the Rietveld method with the FullProf program.[80-83] XRD was also used to determine if the as-synthesized samples were single-phase. Phases were identified by matching the measured patterns with the database at the International Centre for Diffraction Data (ICDD) using the JADE 9 software.

`

2.2.2 Iodometric Titration

The room-temperature oxygen contents of the synthesized materials were determined by iodometric titration.[84] Samples of the powders were dissolved in 15 mL of 10 % KI solution in DI water by adding 10 – 15 mL of 3.5 N HCl. The samples were gently stirred until the powders fully dissolved, at which point the solution was titrated against 0.03 N sodium thiosulfate ($Na_2S_2O_3$) solution. When the solution became mostly clear, a saturated starch solution was added to the mixture to be used as an indicator, as the iodine-starch complex creates a vivid purple color. The solution was then titrated further until the solution became clear.

2.3 THERMAL ANALYSIS

2.3.1 Thermogravimetric Analysis

The change in mass as a function of temperature was observed with a Netzsch STA 449 F3 device. Thermogravimetric analysis (TGA) was carried out from room temperature to 900 °C with varying heating and cooling rates in air that are given in more detail in the respective Chapters. For all cathode materials, all mass change was attributed to loss/gain in oxygen content. The changes in oxygen content and oxidation state of cathodes as a function of temperature were calculated using the room-temperature oxygen content obtained by iodometric titration.

`

2.3.2 Thermal Expansion

The thermal expansion behaviors of the samples were observed in air atmosphere in a Linseis L75H dilatometer. The specimens prepared for observation were cylinder-shape pellets of > 90 % theoretical density, and a length > 5 mm. The thermal expansion coefficients were calculated as

$$\alpha = \frac{1}{L_0}\frac{dL}{dT} \qquad (2.1)$$

where α is the thermal expansion coefficient (TEC), L_0 is the initial length of the sample at room temperature, and dL dT^{-1} is the rate of change of length with respect to change in absolute temperature. The TECs were measured across three consecutive heating and cooling cycles in the range of 80 – 900 °C with a heating/cooling rate of 3 °C min^{-1}.

2.3.3 Electrical Conductivity

The electrical conductivity of the cathodes as a function of temperature were measured with a four-probe dc method using the Van der Pauw configuration.[85-87] The Van der Pauw configuration is shown in Figure 2.1. The Van der Pauw configuration can be used to calculate the specific sheet resistivity of a flat sample as long as the surface area is significantly greater than the thickness of the sample as to effectively create a two-dimensional sample. The specific resistivity, ρ, of a sample can be calculated as

`

$$\rho = \frac{\pi d}{ln2}\frac{\left(R_{12,34}+R_{23,41}\right)}{2} f\left(\frac{R_{12,34}}{R_{23,41}}\right) \qquad (2.2)$$

$$R_{12,34} = \frac{V_{34}}{I_{12}} \qquad (2.3)$$

where R is the resistance, and d is the thickness of the sample. *f* is a function of the ratio of the resistances $R_{12,34}$ / $R_{23,41}$; if the probes are placed so that the geometry is effectively square, the function resolves to equal to 1. In this case, the conductivity, σ, can be calculated as

$$\sigma = \rho^{-1} = 0.2207\,\frac{I}{V \cdot d} \qquad (2.4)$$

where I is the applied current, V is the measured voltage, and d is the sample thickness.

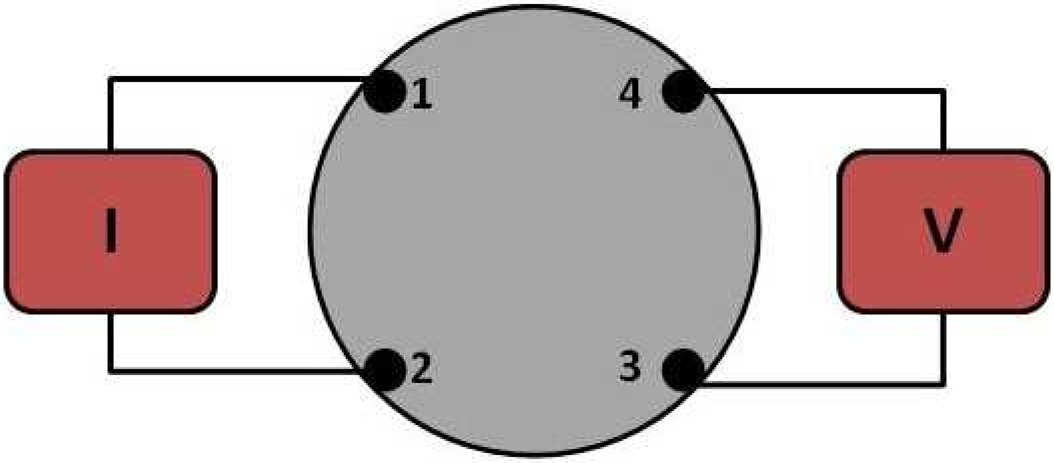

Figure 2.1 Schematic of the Van der Pauw setup, where I is the current source, V is the voltage receiver, and numbers 1-4 are the sample contacts.

`

2.4 ELECTROCHEMICAL ANALYSIS

2.4.1 Materials Processing

For use in electrochemical tests, the synthesized electrolyte supports needed to be cut to the target thickness. Synthesized electrolyte supports were ground on a surface grinder; both surfaces of the electrolyte supports were ground to ensure a uniform surface.

Anodes, cathodes, and barrier layers were applied to electrolyte supports by screen printing inks and sintering. Prior to creating the inks, the synthesized materials were ball-milled for 12 – 48 h in ethanol to ensure particle uniformity. The resultant dried powders were then hand-mixed with an organic binder (Heraeus V006) in either a 50:50 or 60 : 40 powder : binder mass ratio, depending on the amount of binder required to create an ink of desired viscosity. Barrier layers were screen printed 2 times to ensure adequate separation between incompatible materials, while anodes and cathodes were screen printed 3 – 4 times. Materials were sintered at various temperatures depending on the composition; these details are given in the relevant subsequent Chapters.

2.4.2 Electrochemical Impedance Analysis

The polarization resistances (R_ps) of each cathode were measured by AC impedance spectroscopy with a Solartron 1260 FRA analyzer. The cathodes were measured in a symmetric cell configuration on electrolyte supports. LSGM, GDC20, and

8YSZ were used as electrolyte supports in the course of this dissertation, depending on the cathode material investigated. YDC barrier layers were placed between the cathode and 8YSZ electrolytes to prevent side reactions.[35,36] These barrier layers were sintered at 1250 °C for 1 h. Pt and Ag current collectors were utilized. Pt current collectors were applied by screen-printing dilute Pt paste over both cathodes, attaching the Pt mesh and wires with a small amount of concentrated paste, and sintering at 800 °C for 20 minutes. Ag current collectors were applied by screen-printing Ag paste diluted with a dispersant (Hereaus RV 372) on both cathodes, attaching the Ag mesh and wires with concentrated paste (FuelCellMaterials Ag-I), and sintering at 800 °C for 1 h with a 1 °C/min heating rate and a 2 °C cooling rate. Polarization resistances were measured in the range of 400 – 800 °C.

2.4.3 Microstructural Analysis

The microstructures of both symmetric and single cells were observed with a JEOL JSM-5610 scanning electron microscope (SEM).

`

CHAPTER 3

Effects of In Substitution in $Y_{1-x}In_xBaCo_3ZnO_{7+\delta}$ ($0 \le x \le 0.5$) Cathodes for Intermediate Temperature Solid Oxide Fuel Cells

3.1 INTRODUCTION

As discussed in Chapter 1, one of the main areas of investigation in SOFC research is focused on reducing the operating temperature from the conventional 800 – 1000 °C range to the intermediate-temperature (IT) range of 500 - 800 °C. However, traditional cathode materials in the IT region offer greatly diminished performance, and alternative cathode materials are being intensively investigated to successfully develop an intermediate-temperature solid oxide fuel cell (IT-SOFC).[28,62,88,89] Unfortunately, many cathode materials investigated for IT-SOFC have been plagued by thermal expansion coefficients (TECs) that are significantly larger than those of the other SOFC components.[28,62] This TEC mismatch presents a problem, as it can lead to delamination of the components when elevated to operating temperatures. In many materials (*e.g.* $LaBaCo_2O_{5+\delta}$), this thermal expansion is primarily caused by the transition of an octahedral-site Co^{3+} ion from low-spin to high-spin state.[88] Recently, a new series of materials based on $RBa(Co,M)_4O_{7+\delta}$ (R = lanthanide ion, M = transition metal) has been investigated as both oxygen storage materials and by our group as low-TEC cathodes for IT-SOFC.[37,67,74,90,91] These materials do not exhibit any spin-state transition as the cobalt

`

ions are located in tetrahedral sites and therefore always remain in the high-spin configuration with temperature.[37]

The $RBa(Co,M)_4O_{7+\delta}$-based *swedenborgite*-type materials have limited O^{2-} ionic conductivity, so their electrochemical performance is strongly dependent upon the length of the three-phase boundary region (TPB) or the surface area where the cathode, electrolyte, and oxidant all touch.[73] In order to increase the performance, the $RBa(Co,M)_4O_{7+\delta}$ particles are traditionally mixed with an electrolyte to form a composite cathode to extend the TPB.[90,91] In this form, these materials generally offer satisfactory performance as IT-SOFC cathodes, but unfortunately suffer from inadequate long-term thermal stability at the operating temperatures.[37,67,74,90,91]

Previous studies in our group have focused on how substitutions in both the R and M sites of $RBa(Co,M)_4O_{7+\delta}$ affect the long-term thermal stability.[37,67,74,90,91] A substitution of one Zn ion at the M site greatly improves the stability, but the electrochemical performance suffers as the Zn content increases.[37] A variety of substitutions at the R site have also been investigated, and each has different effects on stability and performance.[37,67,74,90,91] It was found that an R = Y in $RBaCo_3ZnO_{7+\delta}$ shows good performance and stability at high temperatures ($T \approx 800$ °C), but otherwise decomposes after exposure to the operating temperatures for an extended period.[74] In contrast, when R = In, the performance and high-temperature stability are generally worse than those with R = Y, but they are stable when held at lower temperatures ($T \approx 600$ °C).[74] When the two are combined in an equimolar ratio (*i.e.* $R = Y_{0.5}In_{0.5}$), the

`

material is stable at all temperatures of interest, and the performance falls between that of R = Y and R = In.[74]

In this chapter, we examine in more detail the effects of In substitution in $Y_{1-x}In_xBaCo_3ZnO_{7+\delta}$ for $0 \leq x \leq 0.5$ between the high-performing R = Y and the fully stabilized R = $Y_{0.5}In_{0.5}$, with the intention of finding the minimum amount of In substitution necessary for stability at all temperatures of interest. The effects of In substitution on crystal chemistry, long-term thermal stability, oxygen content, and electrochemical performance of $Y_{1-x}In_xBaCo_3ZnO_{7+\delta}$ ($0 \leq x \leq 0.5$) are presented.

3.2 EXPERIMENTAL METHODS

The $Y_{1-x}In_xBaCo_3ZnO_{7+\delta}$ samples were synthesized by conventional solid-state reactions (SSR). Required amounts of Y_2O_3, In_2O_3, $BaCO_3$, Co_3O_4, and ZnO were mixed with ethanol in an agate mortar and pestle for 1 h. The mixtures were dried, pressed into pellets, and calcined at 1000 °C for 12 h.[62,69,86,87] The powders were then ground, pressed into pellets, and sintered at 1200 °C for 24 h.[62,69,86,87] The resultant powders were annealed in air at 900 °C for 6 h, and slowly cooled to room temperature at a rate of 1 °C min^{-1}.

The phase stabilities of the $Y_{1-x}In_xBaCo_3ZnO_{7+\delta}$ samples were assessed by both a long-term phase stability measurement and a shorter term variable-temperature method.[37,91] For the long-term measurement, the samples were heated in alumina

`

crucibles in a box furnace to a specific high temperature at 2 °C min^{-1} and were allowed to dwell for 120 h before cooling at the same rate. Three separate tests were conducted, with dwelling temperatures of 600, 700, and 800 °C. The resultant powders were then characterized by XRD.[37,80,91] For the variable-temperature program, the samples were heated at a rate of 5 °C min^{-1} to 1000 °C where they were allowed to dwell for 4 h, followed by cooling at a rate of 2 °C min^{-1} with subsequent 4 h dwells every 100 °C in the range of 900 – 100 °C.[37]

The $Y_{0.2}Ce_{0.8}O_{1.9}$ (YDC) electrolyte was synthesized by the glycine nitrate combustion process (GNP) as described in Chapter 2. Composite cathodes were created by ball-milling $Y_{1-x}In_xBaCo_3ZnO_{7+\delta}$ and $Gd_{0.2}Ce_{0.8}O_{1.9}$ (GDC) powder mixtures in a 50% : 50% weight ratio in ethanol for 12 – 36 h.[74,90,91] The composite cathode powders were then mixed with an organic binder (Heraeus V006) in a 60% : 40% cathode : binder weight ratio to create an ink. The GDC powder was synthesized by both solid-state reaction and GNP methods; both synthesis methods are described in Chapter 2.

For a comparison, $Ba_{0.5}Sr_{0.5}Co_{0.8}Fe_{0.2}O_{3-\delta}$ (BSCF) cathode material was also synthesized by solid-state reaction. Required amounts of $BaCO_3$, $SrCO_3$, Co_3O_4, and Fe_3O_4 were mixed by hand in ethanol in an agate mortar and pestle, dried, and calcined at 1000 °C for 12 h. The resultant powder was then pressed into pellets, sintered at 1100 °C for 20 h, followed by annealing at 900 °C for 6 h with a slow 1 °C min^{-1} cooling rate to maximize the oxygen content.[92] BSCF and YDC were mixed with an organic binder to

`

create inks as described previously with $(Y,In)BaCo_3ZnO_{7+\delta}$ + GDC composite cathode inks.

Thermal expansion data were collected as described in Chapter 2. The sample pellets used during thermal expansion were made by ball-milling the $Y_{1-x}In_xBaCo_3ZnO_{7+\delta}$ powders for 48 h in ethanol, drying the resultant powder, mixing the said powder with a binder (Butvar B76) in ethanol, drying, pressing, and sintering at 1200 °C for 6 h. TGA data were collected during two consecutive heating/cooling cycles at a rate of 3 °C min^{-1} from 80 to 900 °C, with a 15 h dwell at 900 °C after the first heating cycle.[37]

The polarization resistances (R_p) of the $Y_{1-x}In_xBaCo_3ZnO_{7+\delta}$ + GDC composite cathodes were measured on 8 mol % yttria-stabilized zirconia electrolyte supported symmetric cells (8YSZ) in the range of 600 – 800 °C by AC impedance spectroscopy (Solartron 1260 FRA). The effective area of all electrodes was 0.25 cm^2. The electrolyte thickness was between 150 and 200 μm. To prevent interfacial reactions between the composite cathode and the electrolyte, an intermediate layer of YDC was applied as outlined in Chapter 2. The composite cathode layers were then screen-printed three times on each side and sintered for 3 h at 900 °C. Silver paste (FuelCellMaterials Ag-I), mesh, and wires were used as current collectors as described in Chapter 2. The polarization resistances of BSCF were measured on 8YSZ electrolyte supports with the YDC buffer layer as previously described in Chapter 2. The BSCF cathode ink was screen printed three times on each YDC buffer layer and was sintered at 850 °C.[40] Silver current collectors were applied as previously described in Chapter 2. The R_ps of the

`

$YBaCo_3ZnO_7$ + GDC and BSCF cathodes were also measured on symmetric cells in the range or 400 – 600 °C with approximately 0.6 mm GDC electrolyte supports synthesized by solid-state reaction and ground to target thickness with a diamond wheel.

To observe the effect of microstructure on symmetric cell impedance, two new cells were manufactured; one cell with $YBaCo_3ZnO_{7+\delta}$ + GDC by GNP and another cell with $YBaCo_3ZnO_{7+\delta}$ + GDC by GNP that included a small amount of graphite (Alfa Aesar graphite flake 325 mesh) as a pore forming agent. For fabricating the cells, the YBC3Z powder was first ball-milled for 12 - 36 h in ethanol and then dried. Afterwards, this powder was ball-milled for 15 min with an equal mass of GDC synthesized by GNP for the first cell; for the second cell, the powder was ball-milled for 15 min with an equal mass of GDC synthesized by GNP along with 5 wt. % graphite as a pore former that was to be removed later by combustion. This powder was then dried and mixed into an ink as previously described. The symmetric cell preparation process was the same as previously described for $Y_{1-x}In_xBaCo_3ZnO_{7+\delta}$ symmetric cells.

`

3.3 RESULTS AND DISCUSSION

3.3.1 Crystal Chemistry and Phase Stability

The room-temperature XRD patterns of the $Y_{1-x}In_xBaCo_3ZnO_{7+\delta}$ ($0 \leq x \leq 0.5$) oxides are shown in Figure 3.1. All samples were found to be single-phase oxides with the trigonal P31c space group.[74] Unit cell parameters obtained by refinements and room-temperature oxygen contents obtained by iodometric titration are listed in Table 3.1 and shown in Figure 3.2 as a function of indium content. All lattice parameters decrease with increasing indium content due to the substitution of smaller In^{3+} ion (r = 0.92 Å) for the larger Y^{3+} ion (r = 1.019 Å).[93]

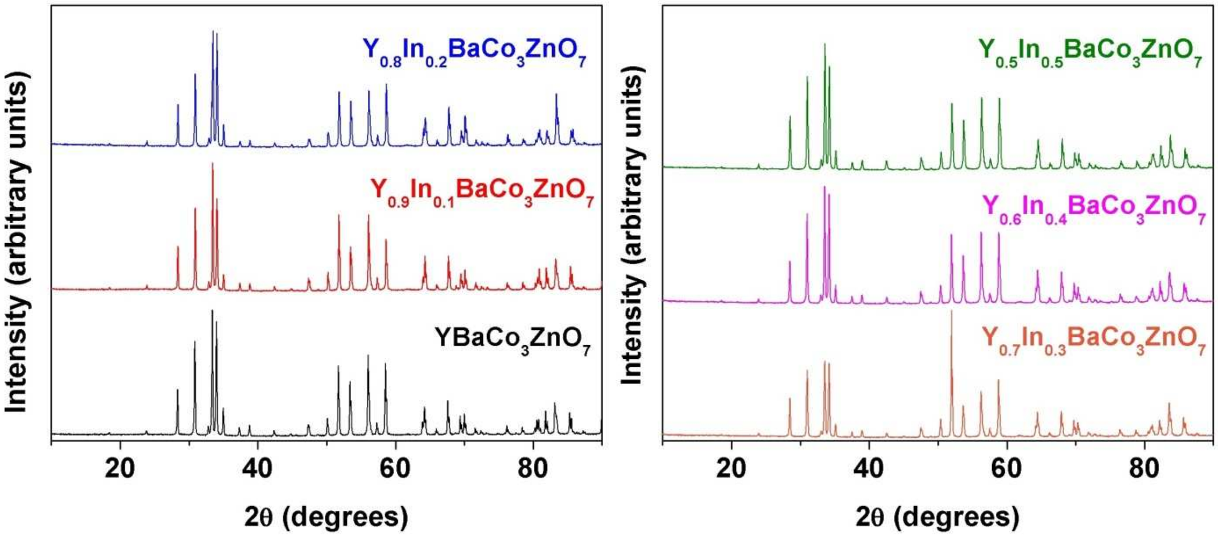

Figure 3.1 Room-temperature XRD patterns of the as-synthesized $Y_{1-x}In_xBaCo_3ZnO_{7+\delta}$ ($0 \leq x \leq 0.5$) samples before long-term stability testing.

`

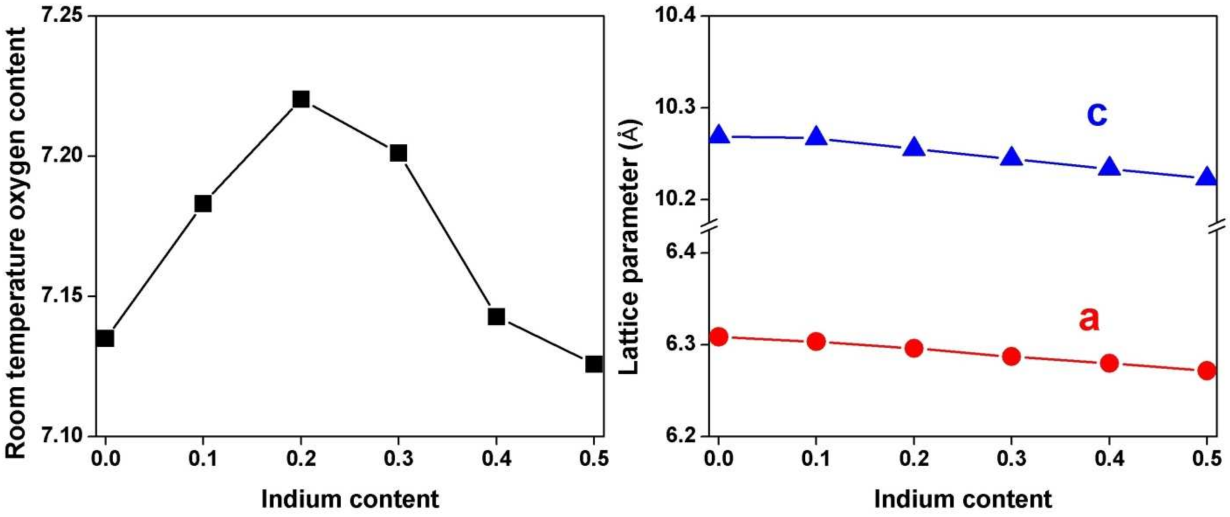

Figure 3.2 Room-temperature oxygen contents and lattice parameter values of $Y_{1-x}In_xBaCo_3ZnO_{7+\delta}$ ($0 \leq x \leq 0.5$).

The oxygen contents of the series increase with indium content for $0 \leq x \leq 0.2$, and then decrease for $0.2 \leq x \leq 0.5$; the values at the endpoints ($x = 0$ and $x = 0.5$) agree well with prior characterizations of this system.[74] This variation can be understood through a combination of unit cell volume and chemistry. Previous work has suggested that the excess oxygen in the lattice is primarily oriented to the CoO_4 tetrahedra.[94] As indium has a significantly larger electronegativity (1.78) compared to yttrium (1.22), the substitution of indium leads to a transfer of electron density from cobalt (electronegativity 1.88) to the R site, thereby allowing more oxygen to orient itself to the cobalt.[95] This may be why $InBaCo_4O_{7+\delta}$ has a slightly larger oxygen content than $YBaCo_4O_{7+\delta}$.[94] However, as the lattice volume decreases, there is less interstitial space in

`

the unit cell for the excess oxygen to reside, causing a decrease in excess oxygen.[67,74] The local maximum in oxygen content around x = 0.2 suggests that the concentration of excess oxygen is dependent upon both the electronegativity and the unit cell volume; at low indium contents, the electronegativity effect dominates, but at higher indium contents, the loss of interstitial space becomes the primary determining factor for the oxygen content.

The short-term phase stabilities of the $Y_{1-x}In_xBaCo_3ZnO_{7+\delta}$ $(0 \leq x \leq 0.5)$ oxides were assessed by a periodic dwelling program in the range of 1000 – 100 °C as outlined in the experimental section. This program was inspired by the program found by our group previously on similar materials and was utilized to determine if materials would decompose under short-term use.[37] No materials were observed to undergo phase decomposition after being exposed to this program (data not shown here). This correlates well with the prior research on similar compounds, as $YBaCo_3ZnO_{7+\delta}$ requires dwelling times above 50 h at elevated temperatures before secondary phases can be observed by XRD.[37,74]

The long-term phase stabilities of the $Y_{1-x}In_xBaCo_3ZnO_{7+\delta}$ $(0 \leq x \leq 0.5)$ oxides were assessed by heating the single-phase powders to 600, 700, or 800 °C for 120 h, as described in the experimental section. As reported in the previous work, $YBaCo_3ZnO_{7+\delta}$ is stable at 800 °C but partially decomposes at both 600 and 700 °C, while $InBaCo_3ZnO_{7+\delta}$ is stable at 600 °C, but partially decomposes at both 700 and 800 °C.[74] Our group also showed that the sample with a mixture of both ions (*i.e.*,

`

$Y_{0.5}In_{0.5}BaCo_3ZnO_{7+\delta}$) is stable at all temperatures. In this study, as shown in Figure 3.3, all samples where $x > 0$ are stable through the entire 600 – 800 °C region, showing that $x = 0.1$ is all that is required to stabilize the phase. As discussed in our previous work, the instability of the $RBa(Co,M)_4O_{7+\delta}$ series of oxides originates from the presence of tetrahedrally coordinated high-spin $Co^{2+/3+}$ ions.[37] The primary decomposition products of the $RBa(Co,M)_4O_{7+\delta}$ oxides are $BaCoO_{3-z}$ and Co_3O_4, both of which contain octahedrally coordinated cobalt ions ($Co^{3+/4+}$ and $Co^{2+/3+}$ ions, respectively).[37,67,74,90,91] Under oxidizing conditions at low temperatures, cobalt tends to exist as low-spin Co^{3+}, which has a large octahedral-site stabilization energy (OSSE), resulting in the above decomposition products.[37,88] Due to the strong preference of Zn^{2+} ions for tetrahedral coordination, the substitution of one Zn^{2+} ion (resulting in $RBaCo_3ZnO_{7+\delta}$) provides stability at shorter times, although depending on the composition of the R-site, long-term stability may not be achieved.[37,74,90,91] The stabilization effect of indium observed in this work may be due to both the increased oxygen content and the decreasing lattice volume. Increasing indium content corresponds with decreasing unit cell volume, which is known to increase the decomposition temperature of this class of materials.[67] These results suggest a complex relationship between the composition of the R-site and the overall thermodynamic stability of these materials, and further investigation is required to better understand these phenomena.

`

Table 3.1 Structural and thermal expansion parameters of $Y_{1-x}In_xBaCo_3ZnO_{7+\delta}$ oxides

x	a (Å)	c (Å)	Volume ($Å^3$)	χ^2	R_{bragg}	TEC 80-900 (10^{-6} K^{-1})
0	6.32	10.27	353.90	3.48	4.74	9.2
0.1	6.30	10.27	353.29	3.28	6.28	9.4
0.2	6.30	10.26	352.05	6.93	9.38	8.9
0.3	6.29	10.24	350.67	11.6	11.8	9.3
0.4	6.28	10.23	349.50	4.91	5.44	9.2
0.5	6.27	10.22	348.22	3.85	5.04	9.2

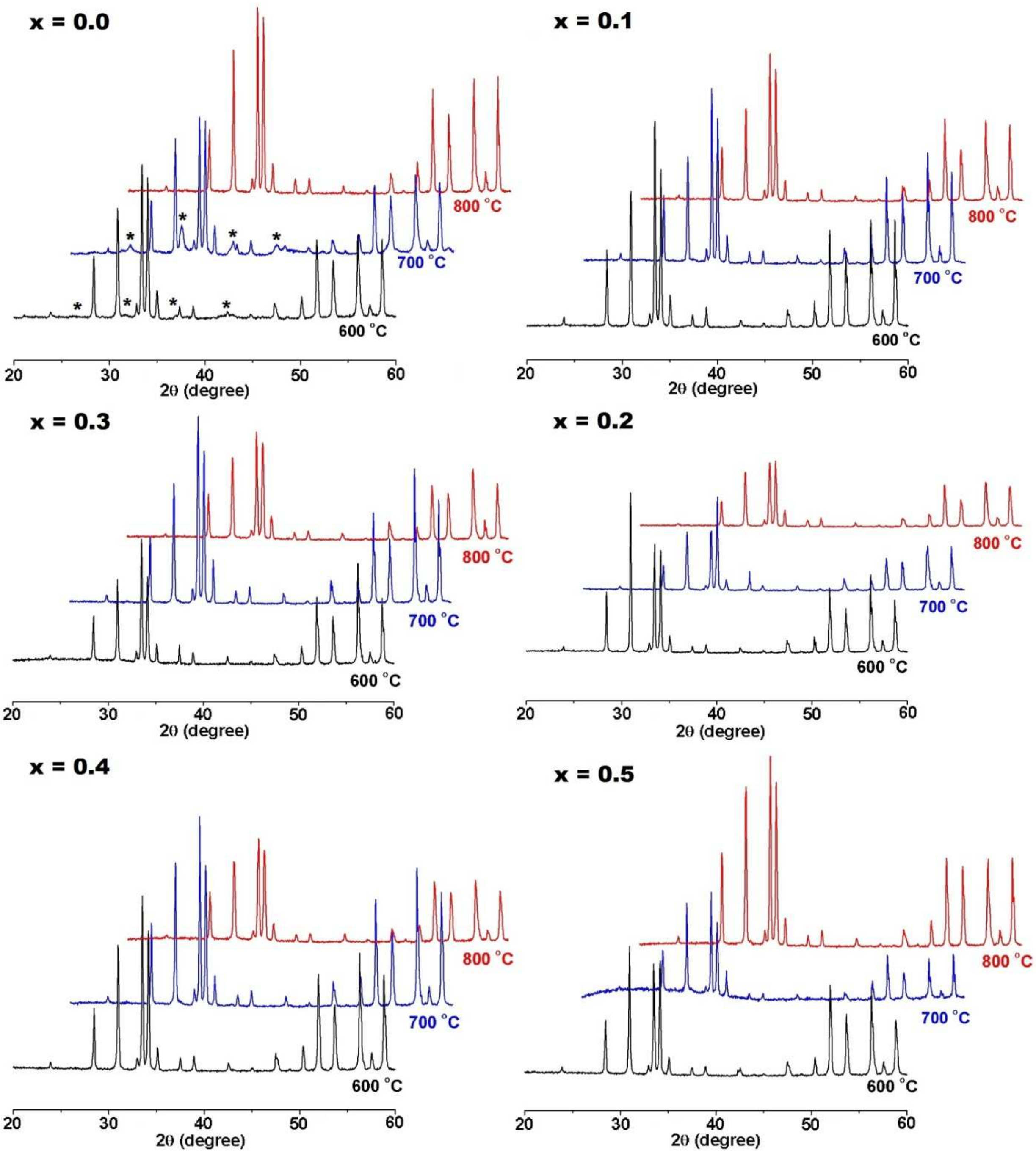

Figure 3.3 Room-temperature XRD patterns of the $Y_{1-x}In_xBaCo_3ZnO_{7+\delta}$ ($0 \leq x \leq 0.5$) samples after 120 h exposure to temperatures of 600, 700, and 800 °C. Peaks marked with * denote $BaCoO_{3-\delta}$ phase formed due to decomposition.

3.3.2 Thermal Expansion and Oxygen Content

The thermal expansion behaviors of these materials were assessed with a dilatometer in air in the temperature range of 80 – 900 °C, and are shown in Figure 3.4. These measurements were taken along three sequential heating and cooling curves to account for experimental variance, and the TECs were calculated ignoring the first heating curve. These values are given in Table 3.1. All TECs fall in the range of 8.9 – 9.4 x 10^{-6} K^{-1}, with no observable trend. As all of these values differ by a very small amount and are in good agreement with previously reported data on similar materials, it is clear that the substitution of indium for yttrium has negligible effect on thermal expansion behavior, and any observed differences are due to experimental variance, *e.g.* minute microstructural defects in the prepared sample pellets, as previous experiments showed that both YBC3Z and $Y_{0.5}In_{0.5}BaCo_3ZnO_{7+\delta}$ have identical thermal expansion coefficients.[74]

`

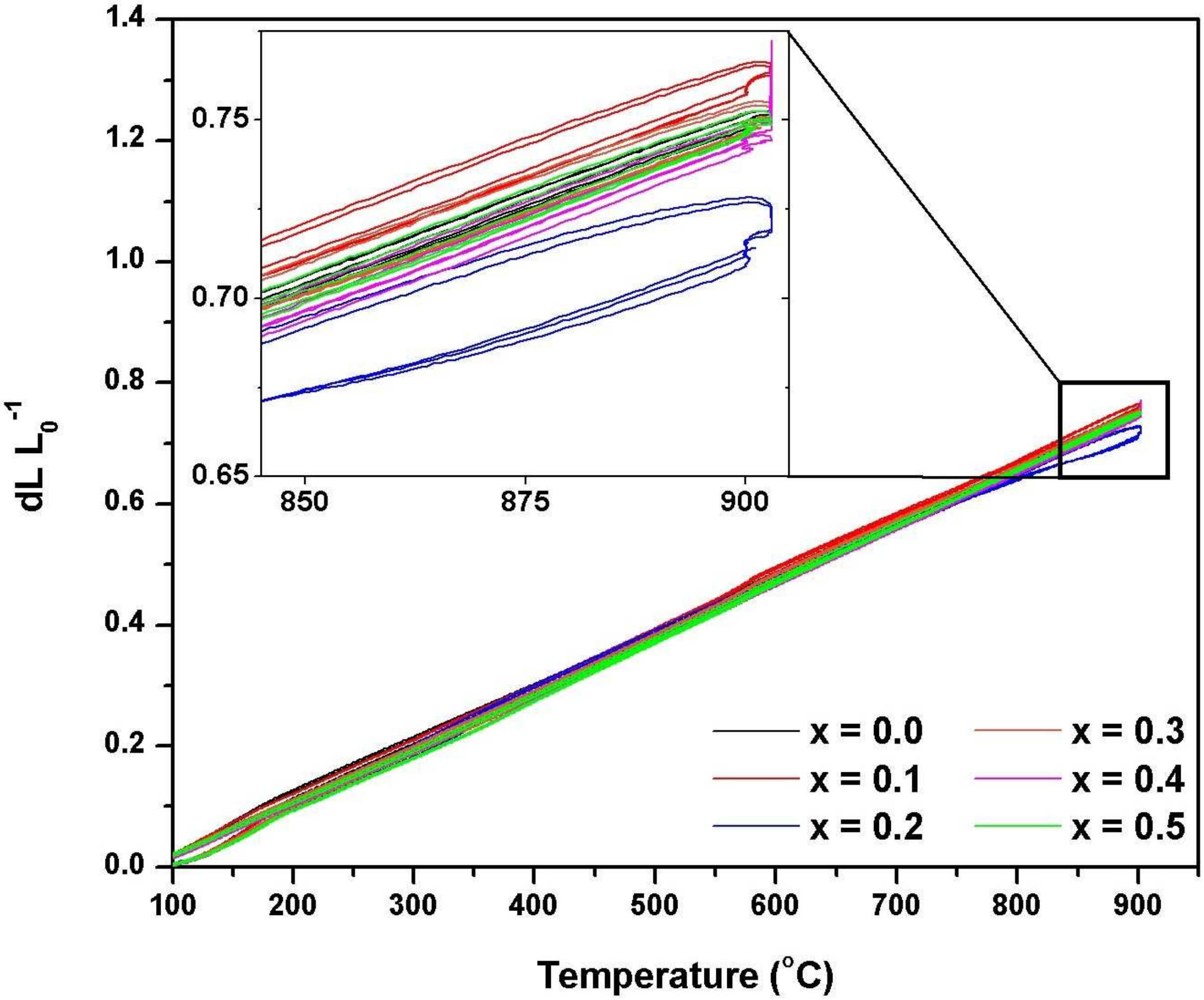

Figure 3.4 Thermal expansion behaviors of $Y_{1-x}In_xBaCo_3ZnO_{7+\delta}$ oxides.

The variations of oxygen content with temperature were assessed with TGA in air along two separate heating and cooling cycles with a 15 h dwell at 900 °C during the first heating cycle to allow for oxygen saturation and ensure equilibrium. This data can be seen in Figure 3.5. The complete oxygen content trajectory of $YBaCo_3ZnO_{7+\delta}$ is shown in Figure 3.5a for reference; in Figures 3.5b and 3.5c, trajectories for the full series have been truncated for clarity. After equilibrating at high temperatures, all samples are observed to reversibly gain mass as hyperstoichiometric interstitial oxygen upon cooling at approximately 300 °C, as in previous studies.[37,67,74,90,91] Interestingly, for all materials in this series, it is not until after the third temperature cycle that the oxygen content upon heating and cooling show similarity. In addition, the oxygen contents immediately after the high-temperature annealing increase with indium content for $0 \leq x \leq 0.3$, and decrease for $0.3 \leq x \leq 0.5$, which agrees well with the room-temperature oxygen content trend observed in Figure 3.2. Overall, the degree of oxygen content variability during thermal cycling decreases with increasing indium content, which agrees with other work.[94] These plots show that as the electronegativity of the R-site atoms increase, the samples show a tendency to increase affinity for a higher oxygen content, which is eventually overcome by the decreasing lattice volume as the indium substitution increases past 30%.

`

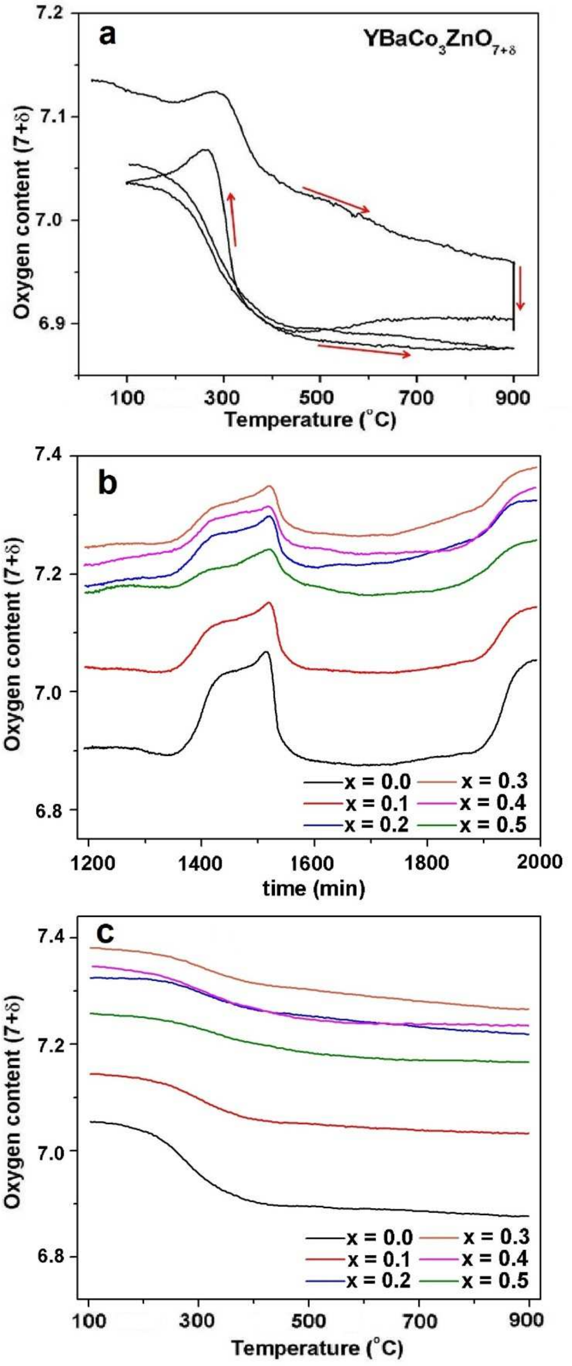

Figure 3.5 TGA plots displaying the oxygen content variations of the $Y_{1-x}In_xBaCo_3ZnO_{7+\delta}$ oxides: (a) full curve of $YBaCo_3ZnO_{7+\delta}$ vs. temperature as an example, (b) oxygen content of the samples with time after the 15 h dwell at 900 °C, and (c) final cooling curves of the samples.

`

3.3.3 Symmetric Cell Optimization and Electrochemical Performances

Electrochemical performances of the $Y_{1-x}In_xBaCo_3ZnO_{7+\delta}$ + GDC composite cathodes were measured by AC impedance spectroscopy in air with cathode | buffer layer | 8YSZ | buffer layer | cathode symmetric cells utilizing 0.2 mm thick electrolytes. The cathodes were prepared by ball-milling equal masses of $Y_{1-x}In_xBaCo_3ZnO_{7+\delta}$ with GDC electrolyte, as previous research has found this to be the optimal ratio for minimizing the polarization resistance (R_p) of the symmetric cells.[90] Since the previous research used micron-grade commercial powder, the GDC electrolyte chosen for these tests was synthesized by solid-state reaction with a small amount of Ni sintering aid to better match the particle size compared to the GNP electrolyte. Buffer layers were included to prevent side-reactions between the cobalt-containing cathode and the zirconia-based electrolyte; YDC was selected for this purpose, as GDC and 8YSZ are known to form a non-conducting interface layer at higher temperatures.[35,36] Silver was chosen as the current collector for its high electrical conductivity, chemical stability, and favorable oxygen reduction kinetics.[96-98]

The silver current collector was applied in three different ways: screen printing of silver paste diluted with the Heraeus organic binder; screen printing of the paste diluted with a dispersant; and as small dots of undiluted paste at each corner and the center of the cathode. A fourth sample of screen-printed pristine YBC3Z was used as a reference current collector. The Nyquist plots of symmetric cell impedances at 600 °C of the $YBaCo_3ZnO_{7+\delta}$ + GDC cathode with these variations are presented in Figure 3.6, and the

`

SEM images taken after testing are shown in Figure 3.7. Of the silver current collectors, the dispersed silver shows the best performance. The undiluted silver dots formed a thick, nonporous silver layer, which impeded the cathode's access to atmospheric oxygen (see Figure 3.7a), and the diluted silver paste did not create sufficient electrical conductivity pathways (Figure 3.7b). The dispersed silver paste, however, formed a fine micron-scale mesh across the cathode (Figure 3.7c). Figure 3.8 shows this mesh from multiple angles. This mesh allowed the cathode ample access to oxygen while still uniformly delivering electrons, serving as an exceptional current collector. The pristine YBC3Z did not perform as well as this silver current collector, due primarily to non-ideal sintering and limited electronic conductivity.[37]

`

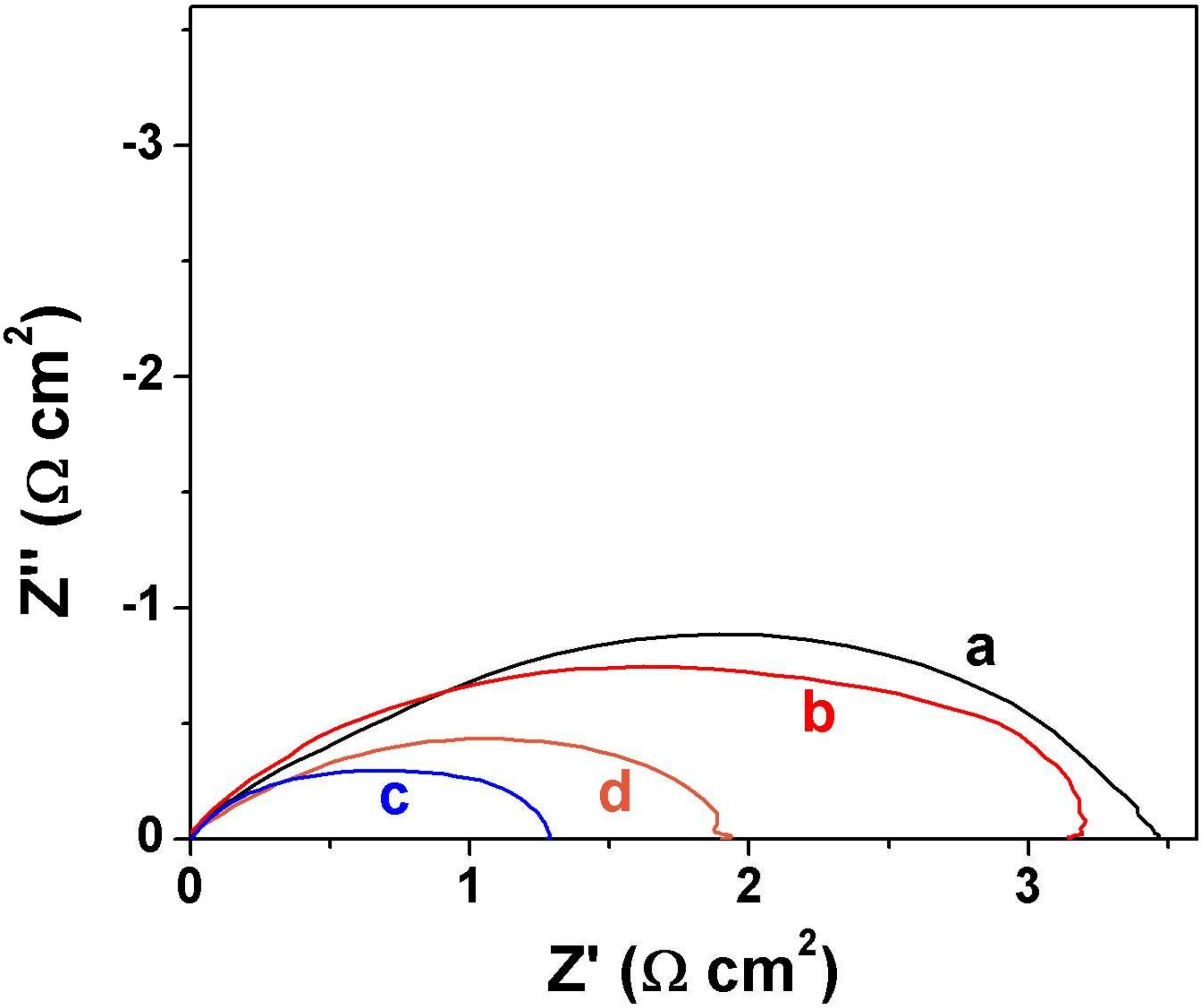

Figure 3.6 Area-normalized AC impedance spectra of $YBaCo_3ZnO_{7+\delta}$ + GDC symmetric cells with varying current collectors: (a) undiluted silver dots, (b) dilute screen-printed silver paste, (c) screen-printed silver paste with dispersant, and (d) pristine $YBaCo_3ZnO_{7+\delta}$.

`

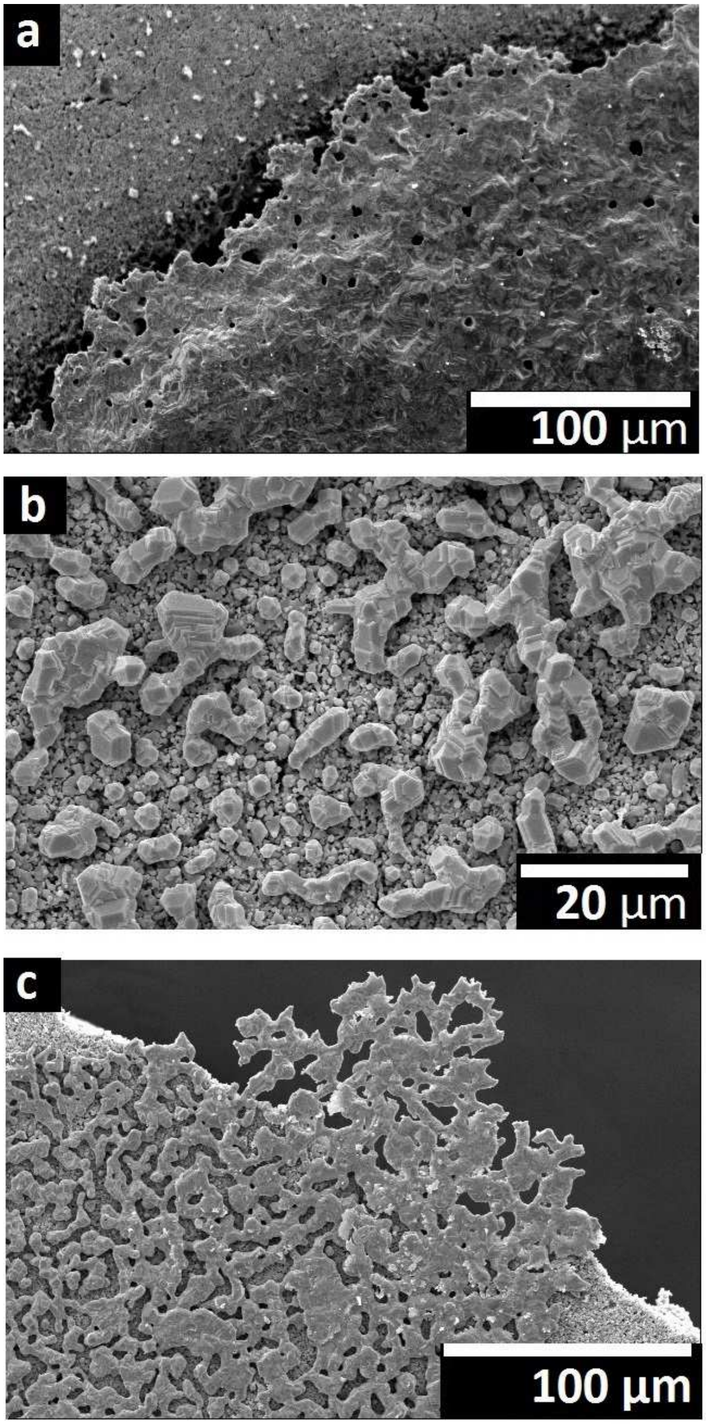

Figure 3.7 SEM micrographs of the various silver current collectors: (a) undiluted silver dots, (b) dilute screen-printed silver paste, and (c) screen-printed silver paste with dispersant.

`

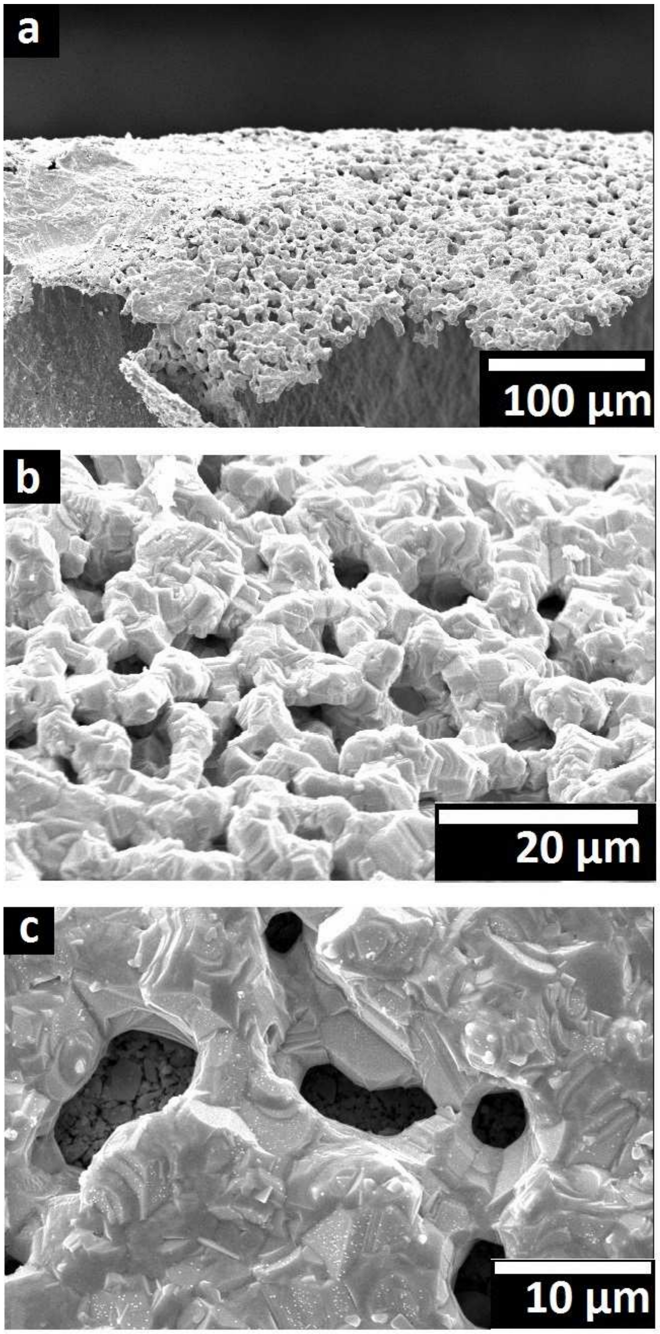

Figure 3.8 SEM micrographs displaying the microstructure of the microscale mesh resulting from screen-printing and heat treating the dispersed silver paste. Images (a) and (b) both show the same section of mesh at different magnifications. Image (c) is included to feature the grade of the mesh. These images show the degree of interconnectivity and strength of the current collector, while featuring pore sizes below 10 microns.

`

Figure 3.9 shows the Arrhenius plots of the polarization resistances of the $Y_{1-x}In_xBaCo_3ZnO_{7+\delta}$ + GDC composite cathodes in the range of 600 – 800 °C. All the samples have very similar R_p values, indicating that substitution of indium for yttrium has minimal impact on the electrochemical performance of this cathode in this temperature range. Any perceived differences among the samples at a given temperature can be primarily attributed to experimental variance. Activation energies derived from these Arrhenius plots are presented in Table 3.2. All samples show similar activation energies, although previous work showed a slight increase from $YBaCo_3ZnO_{7+\delta}$ to $Y_{0.5}In_{0.5}BaCo_3ZnO_{7+\delta}$.[74] However, the difference was very small, and is likely to be due to experimental variance in the fabrication and testing of these devices. Figure 3.10 shows the cross-sectional SEM images of these cells, where there are no discernible variations between microstructures after testing as a function of In content.

`

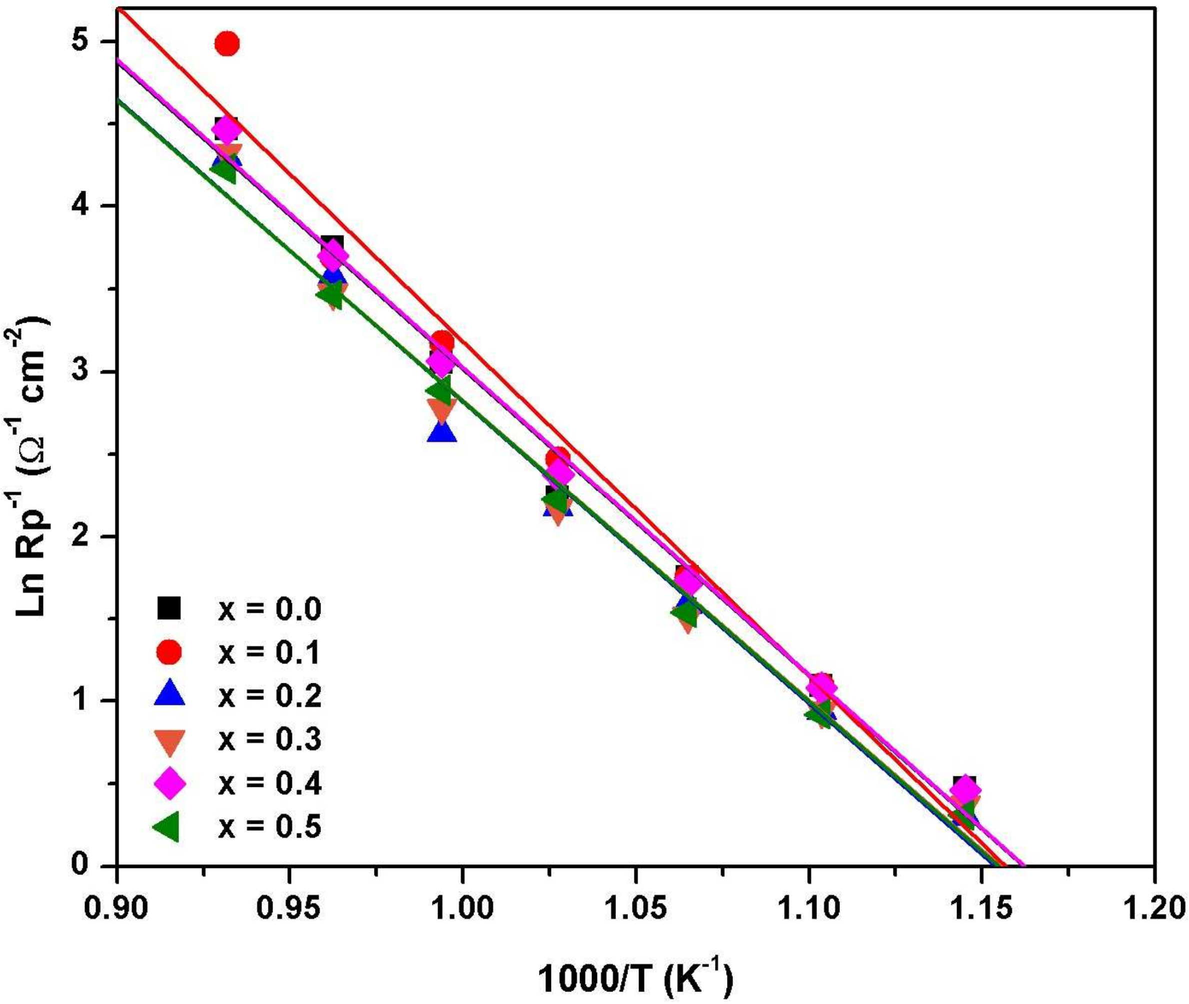

Figure 3.9 Arrhenius plots of the $Y_{1-x}In_xBaCo_3ZnO_{7+\delta}$ + GDC symmetric cells in the range of 600 – 800 °C.

`

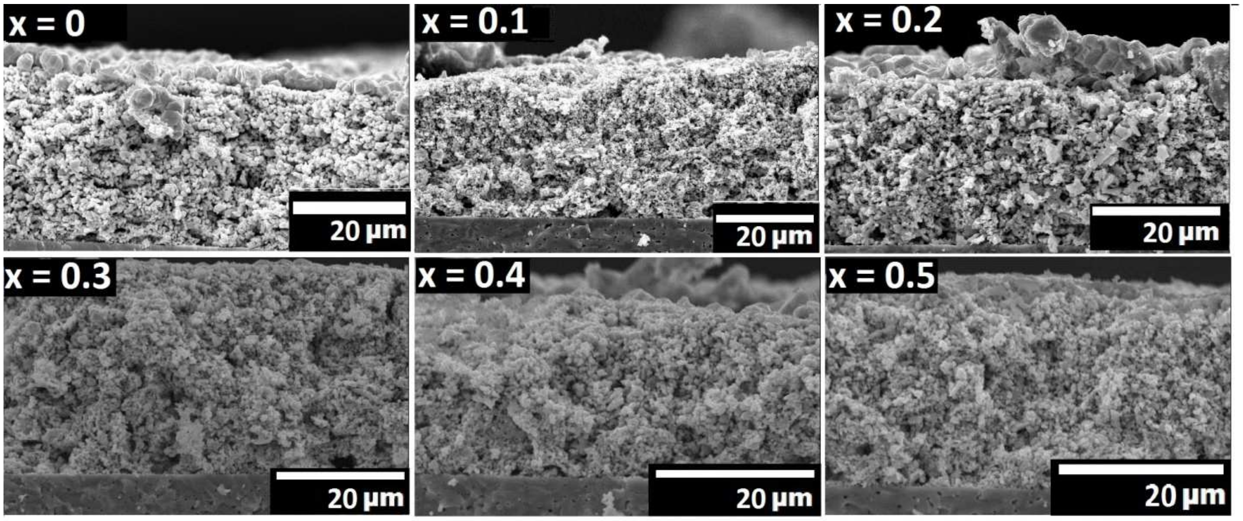

Figure 3.10 SEM micrographs of the $Y_{1-x}In_xBaCo_3ZnO_{7+\delta}$ + GDC symmetric cells (whose performance values can be seen in Figure 9) after testing.

Table 3.2 Electrochemical performance data of the $Y_{1-x}In_xBaCo_3ZnO_{7+\delta}$ + GDC symmetric cells

X value	E_a 600 – 800 °C (eV)
0	1.603
0.1	1.565*
0.2	1.577
0.3	1.566
0.4	1.605
0.5	1.570

* Value shown is as measured from 600 – 766 °C since the value at 800 °C deviated from linearity

`

To observe the effect of microstructure on the performance, two additional cells with $YBaCo_3ZnO_{7+\delta}$ + GDC were made to compare to the YBC3Z + GDC cell already tested: one using GDC synthesized by GNP, and one using GDC by GNP mixed with 5 wt% graphite as a pore former. Both samples were tested on 8YSZ electrolytes with YDC buffer layers. Figure 3.11 shows the AC impedance spectroscopy Nyquist plots comparing these three cells at varying temperatures. As the electrolyte in these cells has significant electrical resistivity in this temperature range, the diameter of the impedance loops may be used as an adequate approximation of polarization resistances.[99-101] In these plots, it can be seen that there is a significant reduction in polarization resistance when the solid-state-reaction GDC is replaced with the GDC-synthesized by the glycine nitrate process. There is a further reduction in polarization resistance when the graphite is added, particularly in the high-frequency region associated with oxygen reduction reaction. This can be understood to be due to the extension of the three-phase boundary region caused by these modifications.

`

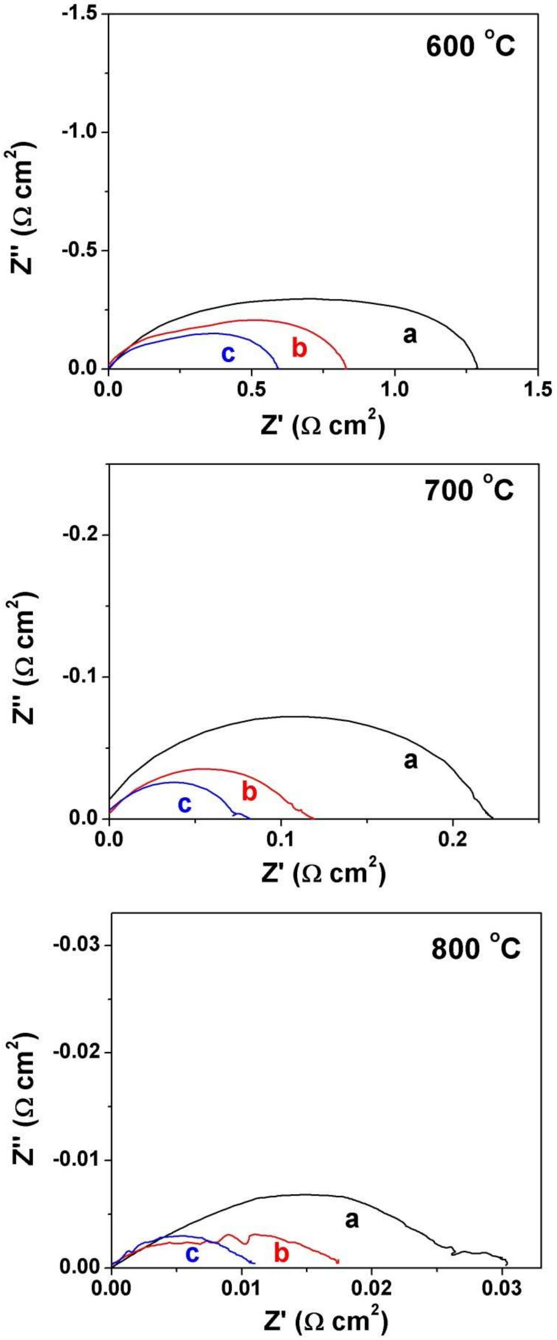

Figure 3.11 Nyquist plots providing the effects of the microstructure of the YBaCo$_3$ZnO$_{7+\delta}$ + GDC symmetric cells on 8YSZ electrolytes, showing the impedance with (a) GDC synthesized by solid-state reaction, (b) GDC synthesized by GNP, and (c) GDC synthesized by GNP with 5 wt. % graphite as pore former. Note that the 800 °C plots use a Bézier curve fitting to reduce signal noise.

`

Finally, the impedances of YBC3Z + GDC (synthesized by solid-state reaction), BSCF, and BSCF + GDC were compared on both 8YSZ + YDC electrolytes and on GDC electrolytes. These data are given in Figures 3.12 and 3.13. In Figure 3.12, it can be seen that YBC3Z + GDC shows performance comparable to both pristine and composite BSCF on 8YSZ electrolyte throughout the entire temperature range of 400 – 800 °C. The Arrhenius plots were generated by fitting the raw data with the equivalent circuit shown in Figure 12b.[91] Figure 3.13 shows that YBC3Z + GDC on GDC electrolyte has reduced polarization resistance at lower temperatures ($400\ °C \leq T \leq 600\ °C$), but BSCF begins to show improved performance as temperature increases. The composite BSCF shows increased polarization resistance across all temperatures due to its mixed ionic and electronic conducting properties; as BSCF can transport oxide ions on its own, the expansion of the three phase boundary has less of an effect on performance. This is also supported by the change in the shape of the Nyquist plot; according to Adler *et al*, the impedance at higher frequencies is attributed to the charge transfer across the electrode / electrolyte boundary, while the impedance at lower frequencies is attributed to the catalytic adsorption/reduction of oxygen at the cathode.[58,99] The inclusion of GDC into the BSCF composite can be seen to slightly reduce the high-frequency impedance due to the increased interface between cathode and electrolyte. In contrast, the low-frequency impedance section is expanded, due to the reduction in catalytically active oxide surface area. These results show that the performance of the $Y_{1-x}In_xBaCo_3ZnO_{7+\delta}$+ GDC cathodes rivals that of the well-studied BSCF, and that the performance can be improved through further optimization of the microstructure and manufacturing process. Future work will investigate these modifications, as well as their effect on microstructural stability and single-cell power densities.

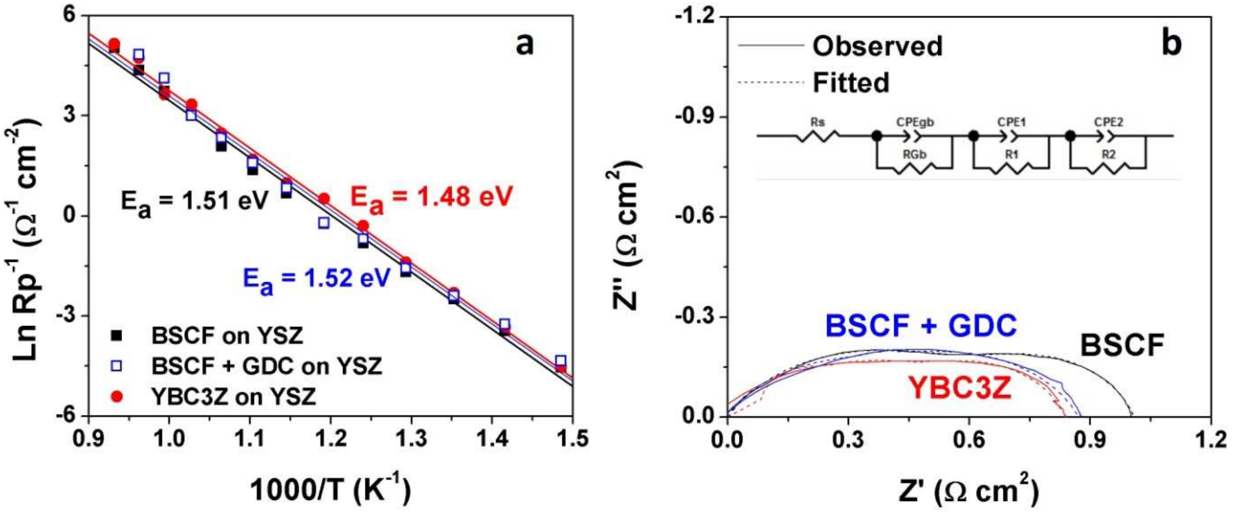

Figure 3.12 (a) Arrhenius plots of $YBaCo_3ZnO_{7+\delta}$ + GDC (made by solid-state reaction and labeled here as YBC3Z), BSCF, and BSCF + GDC symmetric cells on 8YSZ electrolytes in the range of 400 – 800 °C. (b) Nyquist plots of all three cells at 600 °C with the equivalent circuit used to generate the fitted data.

`

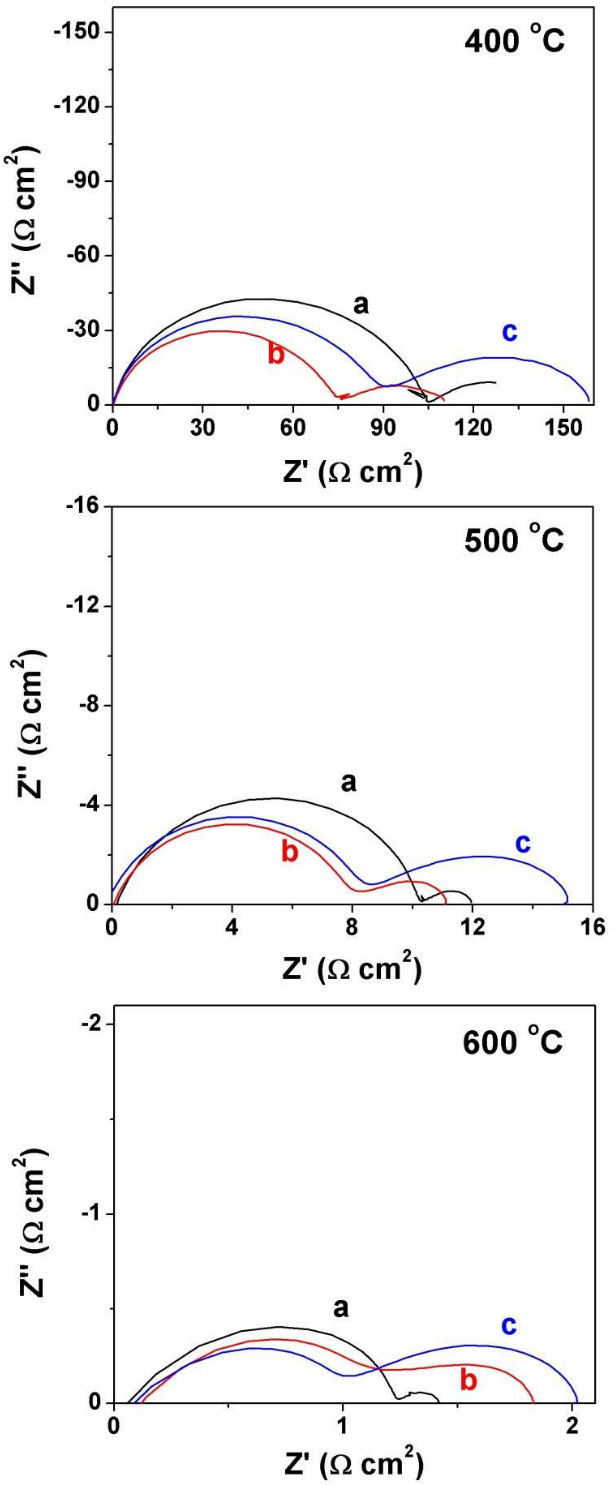

Figure 3.13 Nyquist plots comparing (a) BSCF, (b) $YBaCo_3ZnO_{7+\delta}$ + GDC, and (c) BSCF + GDC symmetric cells on GDC electrolyte in the range of 400 – 600 °C.

`

3.4 CONCLUSIONS

The effects of indium substitution in the $Y_{1-x}In_xBaCo_3ZnO_{7+\delta}$ ($0 \leq x \leq 0.5$) system have been investigated. In contrast to the $x = 0$ sample, all samples with $0.1 \leq x \leq 0.5$ are stable in the 600 – 800 °C range after 120 h exposures, indicating that a mere $x = 0.1$ indium substitution is capable of stabilizing the lattice and phase. Room-temperature oxygen content values reach a weak maximum around $x = 0.2$, but overall do not vary much with indium content. The oxygen contents of the materials show a similar trend after high-temperature annealing in a TGA in air atmosphere, and the substitution of indium for yttrium inhibits the adsorption/desorption of oxygen during thermal cycling. The thermal expansion properties of the samples do not differ significantly with the substitution of indium, and all the samples show good match with the TECs of the traditional SOFC electrolyte materials. Electrochemical performances are not significantly affected by the substitution of indium in this range, which correlates well to previous findings. Preliminary findings show that the polarization resistance of the cathode can be greatly influenced by the microstructure, as the performance of this class of cathodes is strongly dependent on the three-phase boundary region. $YBaCo_3ZnO_{7+\delta}$ + GDC shows a lower polarization resistance than BSCF at temperatures below 600 °C, although BSCF begins to outperform $YBaCo_3ZnO_{7+\delta}$ + GDC as temperatures increase 600 °C, revealing that the $Y_{1-x}In_xBaCo_3ZnO_{7+\delta}$ class of cathodes is particularly attractive for operation below 600 ^{o}C.

CHAPTER 4

Improved Phase Stability and Electrochemical Performance of (Y,In,Ca)BaCo$_3$ZnO$_{7+\delta}$ Cathodes for Intermediate Temperature Solid Oxide Fuel Cells

4.1 INTRODUCTION

As discussed in the previous chapters, SOFC cathodes based on the s*wedenborgite*-type RBa(Co,M)$_4$O$_{7+\delta}$ (R = Y, In, Ca; M = Fe, Zn) structure have shown favorable electrochemical performance and excellent TEC match with the electrolyte, but they tend to suffer from a tendency to decompose after long-term exposure (over 120 hours) to operating temperatures in the range of 600 – 800 °C.[37,74,90,91] Previous work by our group has shown that the stability and electrochemical performance of these materials depend on both the R and (Co,M)$_4$ compositions and tend to have an inverse relationship;[37,74,90,91] for example, a larger R^{3+} ion promotes the reversible oxygen absorption of these materials, but tends to suffer from increased phase instability at higher temperatures.[67,70] Frequently, Co is replaced with Zn, Al, or Ga, which help to stabilize the phase, but also diminish the oxygen absorption and electrical conductivity of these materials.[37,67,74,90,91]

In Chapter 3, it was shown that while YBaCo$_3$ZnO$_{7+\delta}$ is unstable at both 600 and 700 °C, substitution of a small amount of In in the R-site (Y$_{0.9}$In$_{0.1}$BaCo$_3$ZnO$_{7+\delta}$) fully stabilizes the lattice at all temperatures of interest.[29] In the previous work by other members of our group, it was shown that substitution of Ca^{2+} for Y^{3} significantly improves the performance by increasing the oxidation state of cobalt, but requires a substitution of large amount of Zn^{2+} for Co$^{2+/3+}$ to realize phase stability.[91] In this

`

Chapter, we explore the tri-substituted $Y_{1-x-y}In_xCa_yBaCo_3ZnO_{7+\delta}$ $(0.2 \leq (x + y) \leq 0.5)$ series of cathodes, with an aim to combine the stabilizing effect of In with the increased performance effect of Ca.

4.2 EXPERIMENTAL METHODS

4.2.1 Materials Synthesis

The $(Y,In,Ca)BaCo_3ZnO_{7+\delta}$ samples were synthesized by conventional solid-state reactions (SSR) similar to that described in Chapters 2 and 3. Required amounts of Y_2O_3, In_2O_3, $CaCO_3$, $BaCO_3$, Co_3O_4 and ZnO were mixed with ethanol in an agate mortar and pestle for one hour. Samples were dried, pressed into pellets, and calcined at 1000 °C for 12 h.[29,37,74,90,91] Powders were then ground, pressed into pellets again, and sintered at 1200 °C for 24 h.[29,37,74,90,91] After sintering, the pellets were annealed in air at 900 °C for 6 h and slowly cooled to room temperature at a rate of 1 °C min^{-1}.[29]

The $Y_{0.2}Ce_{0.8}O_{1.9}$ (YDC) electrolyte powders were synthesized by the glycine nitrate combustion (GNP) method as described in Chapters 2 and 3. The $Gd_{0.2}Ce_{0.8}O_{1.9}$ (GDC) powder was synthesized by SSR as described in Chapters 2 and 3.

`

4.2.2 Material Characterization

After synthesis and annealing, the (Y,In,Ca)$BaCo_3ZnO_{7+\delta}$ powders were analyzed by X-ray diffraction (XRD) with Cu K_α radiation. The XRD patterns were analyzed with the MDI Jade program, and the data were refined to calculate lattice parameters.

The long-term phase stabilities of the (Y,In,Ca)$BaCo_3ZnO_{7+\delta}$ samples were determined by long-term exposure to traditional SOFC operating temperatures as described in Chapter 3. The resultant powders were characterized by XRD.[29,37,74,90,91]

The oxygen content and oxidation state of cobalt at room temperature were determined by iodometric titration as described in Chapter 2. Thermogravimetric analysis (TGA) with a Netzsch STA 449 F3 thermal analysis system was used to determine the change in oxygen content during thermal cycling as described in Chapters 2 and 3.

4.2.3 Electrochemical Characterization

Composite cathodes were created by ball-milling equal parts by weight of (Y,In,Ca)$BaCo_3ZnO_{7+\delta}$ and GDC powders in ethanol for 36 – 48 h.[29,74,90,91] The composite powders were then dried, and mixed with an organic binder (Heraeus V006) in a 60 : 40 cathode : binder weight ratio to create an ink.[29,37,74,90,91] YDC electrolyte ink was prepared similarly, though the YDC powders were not ball milled prior to mixing.[29]

The polarization resistances (R_P) of the composite cathodes were measured on 8 mol% yttria-stabilized zirconia (8YSZ) electrolyte supported symmetric cells in the range of 400 – 800 °C by AC impedance spectroscopy (Solartron 1260 FRA). The details for this experiment are described in Chapter 3. R_P values of selected (Y,In,Ca)$BaCo_3ZnO_{7+\delta}$ were also measured on 250 μm thick GDC substrate (FuelCellMaterials) for a comparison, without a YDC buffer layer. The microstructures of all symmetric cells were observed in a JEOL JSM-5610 scanning electron microscope after the electrochemical impedance spectroscopy (EIS) measurement.

4.3 RESULTS AND DISCUSSION

For ease of reference, the samples will be referenced by their R-site composition; *e.g.* $Y_{0.8}In_{0.1}Ca_{0.1}BaCo_3ZnO_{7+\delta}$ will be referred to as $Y_8In_1Ca_1$, $Y_{0.7}In_{0.2}Ca_{0.1}BaCo_3ZnO_{7+\delta}$ will be referred to as $Y_7In_2Ca_1$, and so on. Similarly, the samples will be grouped into two sub-series based on their calcium content; samples where $y = 0.1$ will be labeled as “high-In,” and samples where $0.2 \leq y \leq 0.4$ will be labeled as “high-Ca,” with $Y_8In_1Ca_1$ belonging to both sub-series.

4.3.1 Phase Stability and Crystal Chemistry

The room-temperature XRD patterns of the (Y,In,Ca)$BaCo_3ZnO_{7+\delta}$ oxides, shown in Figure 4.1, indicate that all samples investigated were successfully synthesized as single-phase materials with a *P31c* space group similar to $Y_{1-x}In_xBaCo_3ZnO_{7+\delta}$ ($0 \leq x \leq 0.5$).[29] Unit cell parameters obtained by refinements are listed in Table 1. The addition of In decreases the unit cell volume, while the addition of calcium slightly increases the unit cell volume. This is attributed to the replacement of Y^{3+} (r = 1.019 Å), respectively, with In^{3+} (r = 0.92 Å) and Ca^{2+} (r = 1.12 Å).[93] In the high-In series, the *a* and *c* lattice parameters both decrease with increasing In content. In the high-Ca series, *a* increases and *c* decreases with increasing Ca content, leading to a smaller change in volume as compared to the In substitutions. This correlates well with previous reports.[91]

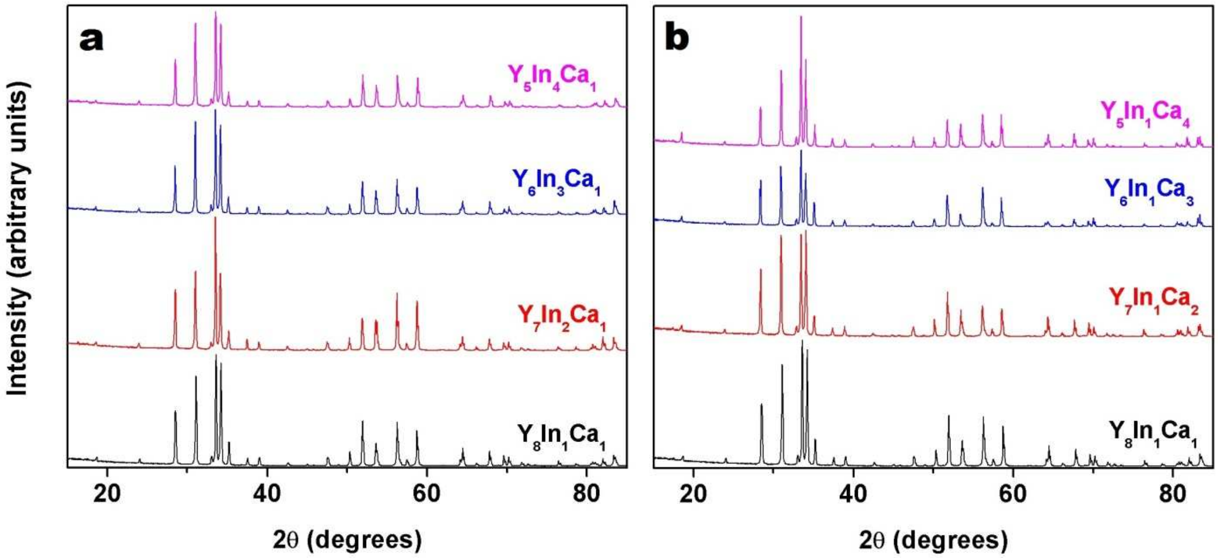

Figure 4.1 Room-temperature XRD patterns of the as-synthesized $(Y,In,Ca)BaCo_3ZnO_{7+\delta}$ samples before long-term stability testing.

`

The ratio of *a/c* is also listed in Table 4.1, where it can be seen that an increasing In content slightly decreases this ratio, while an increasing Ca content leads to an increasing ratio. The naturally occurring *swedenborgite* ($NaSbBe_4O_7$) shows a ratio of *a/c* = 0.613, which may be used as a reference.[102] As Ca content increases, the *a/c* ratio deviates further from the *swedenborgite* ratio, which may lead to increased lattice strain.

The room-temperature oxygen contents of all $(Y,In,Ca)BaCo_3ZnO_{7+\delta}$ oxides determined by iodometric titration are presented in Table 2. In the high-In series, the oxygen content tends to increase with increasing In content, except for an initial decrease from $Y_8In_1Ca_1$. This trend was also observed in the previous work on $Y_{1-x}In_xBaCo_3ZnO_{7+\delta}$, where it was shown that oxygen content initially increases with increasing In content and then decreases once the unit cell volume is smaller than approximately 350 Å^3.[29] As the In content continues to increase, the decreasing lattice volume reduces the available interstitial volume and limits the oxygen content.[29,67,74] In this work, with the addition of the larger Ca^{2+} ion, this constraint is lessened: at the maximum In content investigated, $Y_5In_4Ca_1$, the unit cell has a volume of 350.23 Å^3.

For the high-Ca series, the room-temperature oxygen content tends to decrease with increasing Ca content. The decrease arises from the substitution of trivalent Y^{3+} ions by divalent Ca^{2+} ions, which causes both an increase in Co oxidation state and a decrease in oxygen content to maintain charge neutrality. This observation is supported by previous work.[91] This leads to a trend in both series of an increasing oxidation state with decreasing Y content at room temperature.

`

The long-term phase stability XRD patterns are shown in Figure 2. All peaks match well with the XRD patterns shown in Figure 1, confirming that all samples are stable after 120 h exposure to all temperatures investigated here. As reported in our previous work, a small substitution of 10% In for Y results in the fully stabilized $Y_{0.9}In_{0.1}BaCo_3ZnO_{7+\delta}$ material due to increased oxygen content and decreased lattice size.[29] Our group has also previously found that in $(Y,Ca)Ba(Co,Zn)_4O_{7+\delta}$, a minimum Zn content of 1.5 is necessary to stabilize a Ca substitution of 0.5.[91] The inclusion of Zn stabilizes the phase since Zn^{2+} has a strong preference for tetrahedral coordination and $Co^{2+/3+}$ ions are relatively unstable in tetrahedral coordination.[37,67,74,90,91] However, the inclusion of Zn negatively impacts the performance of this material as a cathode in multiple ways. Zn has a very stable electron configuration of $3d^{10}$, and therefore cannot contribute to electrical conductivity, oxygen absorption, or oxygen reduction. As can be observed in Figure 4.2, all investigated samples of $(Y,In,Ca)BaCo_3ZnO_{7+\delta}$ are stable at all temperatures of interest. When compared to the previous work, where $Y_{0.5}Ca_{0.5}BaCo_3ZnO_{7+\delta}$ is unstable at both 600 and 700 °C, this shows that the small substitution of In is once again enough to stabilize the material at lower temperatures, reducing the dependence on the content of the performance-inhibiting Zn.[91]

`

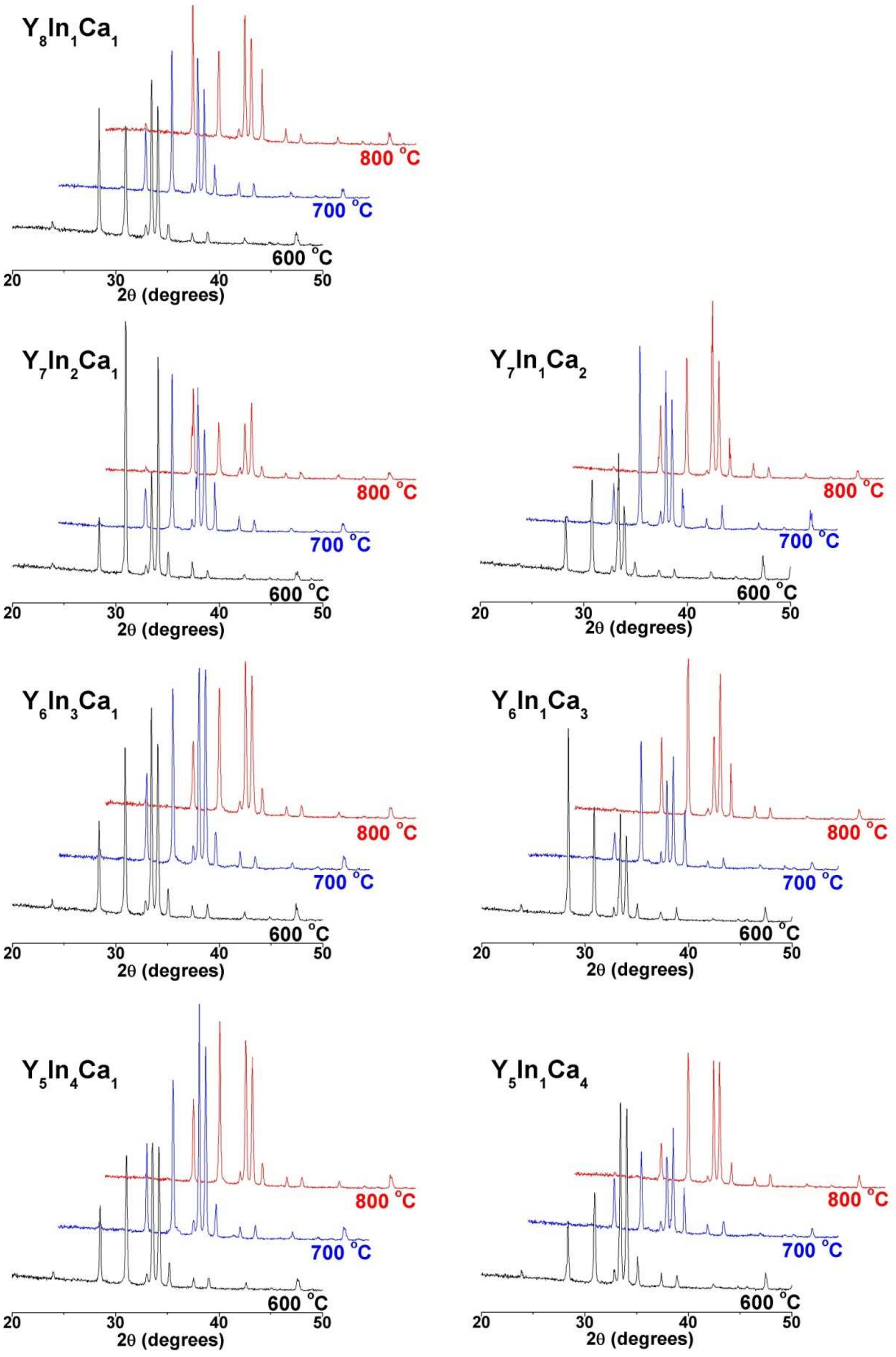

Figure 4.2 Room-temperature XRD patterns of the (Y,In,Ca)$BaCo_3ZnO_{7+\delta}$ samples after 120 h exposure to 600, 700, and 800 °C. No impurity phases were detected in any sample after long-term exposure.

`

Table 4.1 Unit cell parameters and activation energies of the (Y,In,Ca)$BaCo_3ZnO_{7+\delta}$ oxides and composite cathodes

Sample	*a* (Å)	*c* (Å)	Volume (Å^3)	*a*/*c*	E_a (eV)*
High In					
$Y_8In_1Ca_1$	6.310	10.261	353.75	0.6149	1.223
$Y_7In_2Ca_1$	6.305	10.256	353.05	0.6147	1.242
$Y_6In_3Ca_1$	6.300	10.248	351.8	0.6144	1.257
$Y_5In_4Ca_1$	6.286	10.234	350.23	0.6142	1.268
High Ca					
$Y_8In_1Ca_1$	6.310	10.261	353.75	0.6149	1. 223
$Y_7In_1Ca_2$	6.313	10.259	354.11	0.6154	1.259
$Y_6In_1Ca_3$	6.318	10.254	354.43	0.6161	1.328
$Y_5In_1Ca_4$	6.320	10.248	354.43	0.6167	1.320

* Activation energies calculated in the range of 400 – 750 °C

4.3.2 Thermal Properties and Electrochemical Performance

The variations of oxygen content with temperature as observed by TGA in air, with all mass gain and loss attributed to absorption and desorption of oxygen, are shown in Figure 4.3. The full trace of oxygen content versus temperature for $Y_8In_1Ca_1$ is shown in Figure 4.3a. Figure 4.3a also defines three points along the curve: room-temperature, TGA-dwell, and final-cooling points. Table 4.2 lists the oxygen contents at these points for all samples, along with the derived average Co oxidation states. All samples show similar traces, gaining a significant amount of oxygen during the 15 h annealing period. For clarity, Figures 4.3b and 4.3c only show the final cooling curve of the high-In and high-Ca samples, respectively. To determine the initial room-temperature oxygen content, titration was performed on all samples prior to experiments in the TGA.

`

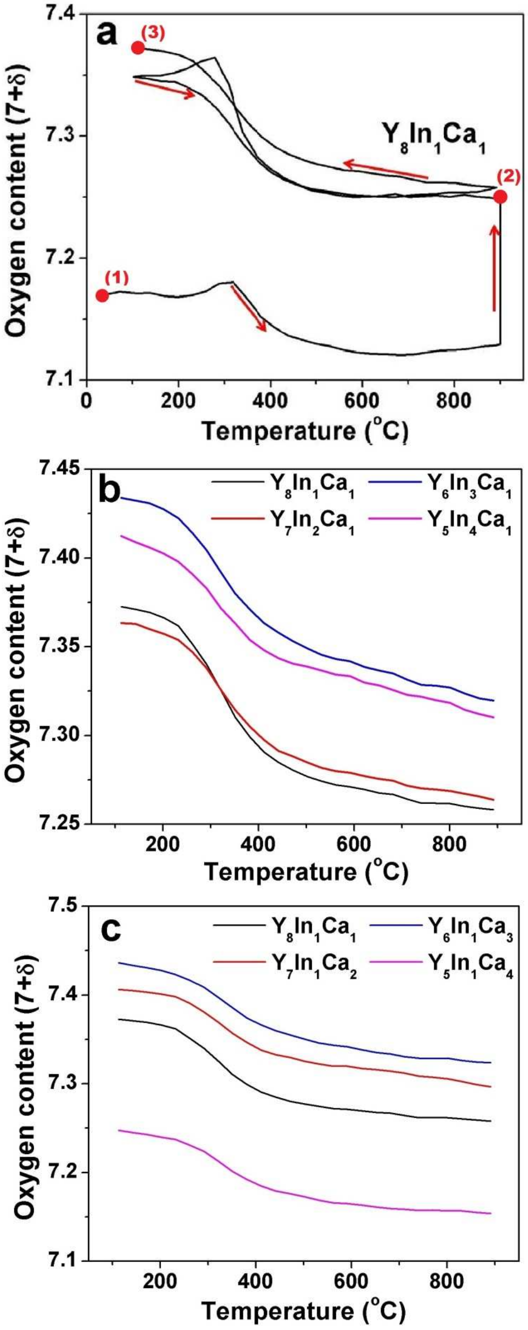

Figure 4.3 TGA plots detailing the oxygen content variations of the as-synthesized (Y,In,Ca)BaCo$_3$ZnO$_{7+\delta}$ oxides: (a) full curve of Y$_{0.8}$In$_{0.1}$Ca$_{0.1}$BaCo$_3$ZnO$_{7+\delta}$ as an example, (b) final cooling curve of the high-In samples, and (c) final cooling curve of the high-Ca samples. All samples were allowed to anneal 15 h in air, as seen in (a). Figure 4.3a also defines three points along the curve that are used in Table 4.2: (1) is the room-temperature point, (2) is the TGA-dwell point, and (3) is the final-cool point.

`

Table 4.2 Oxygen contents and Co oxidation states of the (Y,In,Ca)$BaCo_3ZnO_{7+\delta}$ oxides

	Room Temperature		TGA Dwell		Final Cool	
Sample	**Oxygen Content (7+δ)**	**Average Co Oxidation State***	**Oxygen Content (7+δ)**	**Average Co Oxidation State***	**Oxygen Content (7+δ)**	**Average Co Oxidation State***
High In						
$Y_8In_1Ca_1$	7.167	2.478	7.248	2.532	7.373	2.615
$Y_7In_2Ca_1$	7.128	2.452	7.237	2.524	7.363	2.609
$Y_6In_3Ca_1$	7.158	2.472	7.271	2.547	7.434	2.656
$Y_5In_4Ca_1$	7.170	2.480	7.288	2.558	7.412	2.642
High Ca						
$Y_8In_1Ca_1$	7.167	2.478	7.248	2.532	7.373	2.615
$Y_7In_1Ca_2$	7.153	2.502	7.251	2.567	7.406	2.671
$Y_6In_1Ca_3$	7.137	2.525	7.298	2.632	7.436	2.724
$Y_5In_1Ca_4$	7.143	2.562	7.171	2.581	7.248	2.632

* The average Co oxidation state of the undoped $YBaCo_3ZnO_7$ would be 2.33

`

As can be seen in Table 4.2, both the high-In and high-Ca series show a trend of increasing oxygen content after annealing in the TGA, with the exception of the $Y_5In_1Ca_4$ sample. This can be explained to be due to a reduction in oxygen storage capacity; since Ca has a fixed valence state of Ca^{2+} in this material, the substitution of Ca^{2+} for Y^{3+} leads to an increase in the oxidation state of Co. As the reversible oxygen absorption is directly related to the capability of the Co ions to be oxidized, this increase in Ca content leads to a decreased maximum oxygen content. This is supported by previous work, which shows that an increased Ca content results in a reduced oxygen absorption upon thermal cycling.[91]

Electrochemical performances of the $(Y,In,Ca)BaCo_3ZnO_{7+\delta}$ oxides were evaluated by AC impedance spectroscopy on cathode | YDC | electrolyte | YDC | cathode symmetric cells as outlined in the experimental section. As the $RBa(Co,M)_4O_{7+\delta}$ oxides have historically been shown to have low oxide-ion conductivity, composite cathodes of $(Y,In,Ca)BaCo_3ZnO_{7+\delta}$ and GDC were utilized in a 1 : 1 mass ratio.[37,90] This ratio was fixed as the previous research found it to be ideal in the case of $YBaCo_3ZnO_{7+\delta}$ composite cathodes.[90] Previous research has shown that the performances of this class of materials are strongly dependent on the three-phase boundary (TPB) region, which is the surface area where the electrolyte, cathode, and oxidant all touch.[29,73,74,90,91] The powders were ball-milled to both increase the homogeneity of the mixture and to reduce the particle size, thereby increasing the size of the TPB. YDC was utilized as the buffer layer to prevent the reaction between both the cobalt and gadolinium in the composite cathodes with the YSZ electrolyte.[35,36] Silver was used as the current collector due to its non-

`

reactivity, high electrical conductivity, and favorable oxygen reduction reaction kinetics.[96-98] The silver current collector was assembled as described in our previous work to form a micron-scale mesh on the surface of the cathode.[29] Similar composite cathodes have been shown to have low electrical conductivity due to both the inclusion of the electrolyte material and the Zn^{2+}:$3d^{10}$ ions with completely filled *d* orbitals in $RBa(Co,M)_4O_{7+\delta}$. The micro-mesh silver current collector has been shown to significantly reduce the polarization resistance of the symmetric cells due to their high degree of interconnectivity while still maintaining good porosity for oxidant transport.[29]

Figure 4.4 shows the Arrhenius plots of the polarization resistances of the $(Y,In,Ca)BaCo_3ZnO_{7+\delta}$ composite cathodes on 8YSZ electrolyte supported symmetric cells in the range of 400 – 800 °C. Since 8YSZ has insignificant electronic conductivity in this temperature range, the polarization resistances of these cathodes were calculated by taking the difference between the high- and low-frequency intercepts with the real axis.[99-101] As shown in Figure 4.4a, all high-In samples show similar polarization resistances. This matches well with our previous work in the $(Y,In)BaCo_3ZnO_{7+\delta}$ series, where the In content did not significantly impact the performance.[29] In Figure 4b, it can be seen that all high-Ca samples outperform the $Y_8In_1Ca_1$ samples. The activation energies obtained from these plots in the range of 400 – 750 °C are given in Table 4.1. The 800 °C values are omitted from calculation because of the increased errors in measurement at very low polarization resistances due to the sensitivity limits of the AC-impedance spectrometer. The high-In and high-Ca series both show a general trend of increasing activation energy with increasing In and Ca contents respectively, which

`

correlates well to the previous work.[29,91] The mechanism related to this increase in activation energy is not yet well understood and should be investigated further in future work. Figure 4.4c compares the performance of the $Y_8In_1Ca_1$ composite cathode with a composite cathode of $YBaCo_3ZnO_{7+\delta}$ (Y_{10}) + GDC, where it can be seen that $Y_8In_1Ca_1$ slightly outperforms Y_{10} at all temperatures.

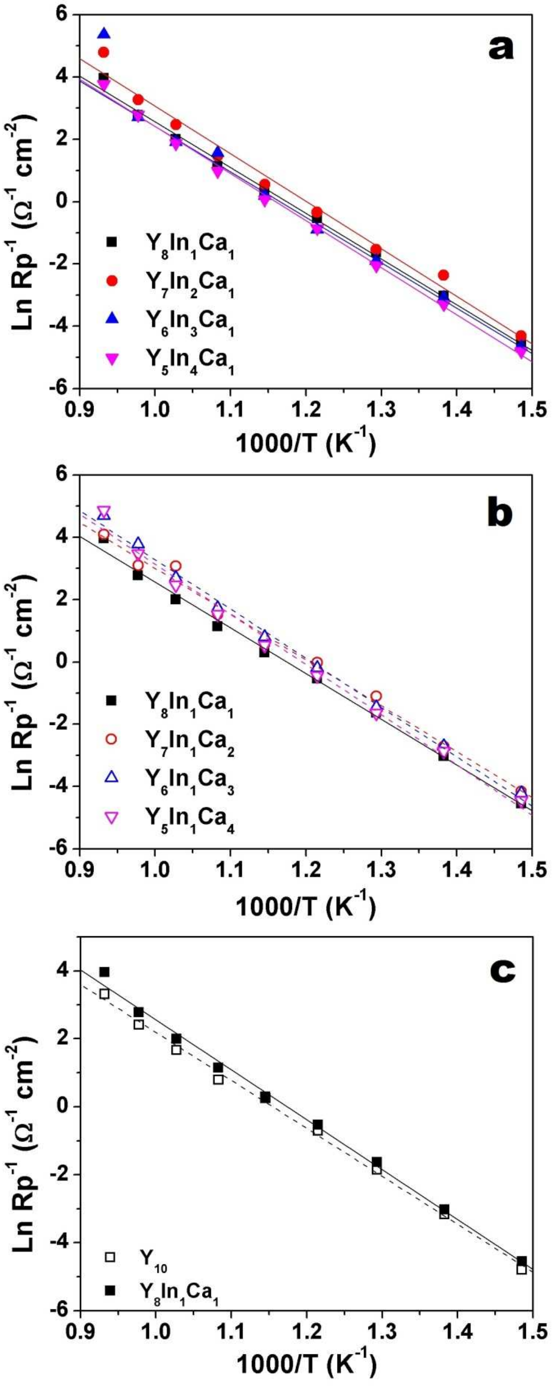

Figure 4.4 Arrhenius plots of the (Y,In,Ca)$BaCo_3ZnO_{7+\delta}$ + GDC symmetric cells on 8YSZ electrolyte in the range of 400 – 800 °C: (a) Arrhenius plots of the high-In samples, (b) Arrhenius plots of the high-Ca samples, and (c) Arrhenius plots comparing $Y_{0.8}In_{0.1}Ca_{0.1}BaCo_3ZnO_{7+\delta}$ with the undoped $YBaCo_3ZnO_{7+\delta}$ for a comparison.

`

Figure 4.5 shows the Arrhenius plots of the polarization resistances of $Y_8In_1Ca_1$, $Y_5In_4Ca_1$, and $Y_5In_1Ca_4$ composite cathodes on GDC electrolyte supported symmetric cells. These cells were manufactured to better observe the effects of composition on performance in the lower-temperature region, as the reduced ionic conductivity of 8YSZ at temperatures below 600 °C can limit performance.[16] Figure 4.5 shows that the polarization resistance of $Y_5In_4Ca_1$ is similar to $Y_8In_1Ca_1$ at temperatures below 600 °C, but begins to show reduced polarization resistance at higher temperatures. $Y_5In_1Ca_4$, on the other hand, outperforms $Y_8In_1Ca_1$ at all temperatures, notably including the 400 – 600 °C range. The Nyquist plots of all three samples at 400, 500, and 600 °C are presented in Figure 4.6 to further show this comparison. At 400 °C (Figure 4.6a), clear arc separation behavior is observed. According to Adler *et al.*, the impedance at high-frequencies derives from the charge transfer across the electrolyte, at medium frequencies from the charge transfer at the electrode/electrolyte interface, and at low frequencies from the oxygen surface exchange.[58,99] At 400 °C, the arc separation is clearest in the $Y_8In_1Ca_1$ sample, where three arcs are observed. As temperatures increase to 500 and 600 °C, the separation of arcs becomes harder to detect, with only the low-frequency oxygen surface exchange arc remaining observable. After the measurement, these cells were fractured and were observed by SEM to determine the effect of microstructure on performance. The cross-sectional images are presented in Figure 4.7, where it can be observed that all cells have negligible differences in microstructure.

`

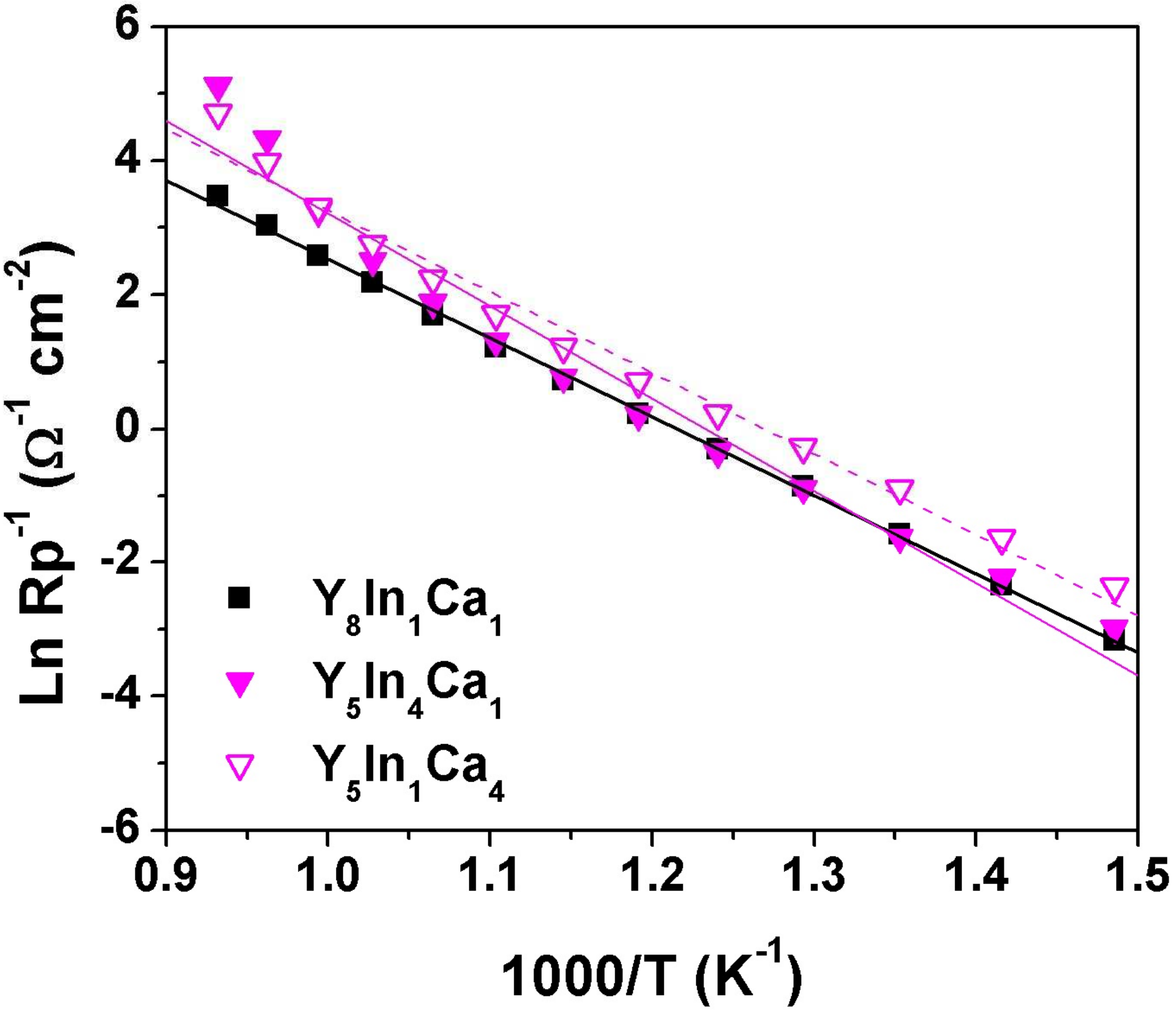

Figure 4.5 Arrhenius plots of $Y_{0.8}In_{0.1}Ca_{0.1}BaCo_3ZnO_{7+\delta}$ + GDC, $Y_{0.5}In_{0.4}Ca_{0.1}BaCo_3ZnO_{7+\delta}$ + GDC, and $Y_{0.5}In_{0.1}Ca_{0.4}BaCo_3ZnO_{7+\delta}$ + GDC symmetric cells on GDC electrolyte in the range of 400 – 800 °C. The $Y_5In_1Ca_4$ sample shows improved performance at all temperatures, particularly below 600 °C.

`

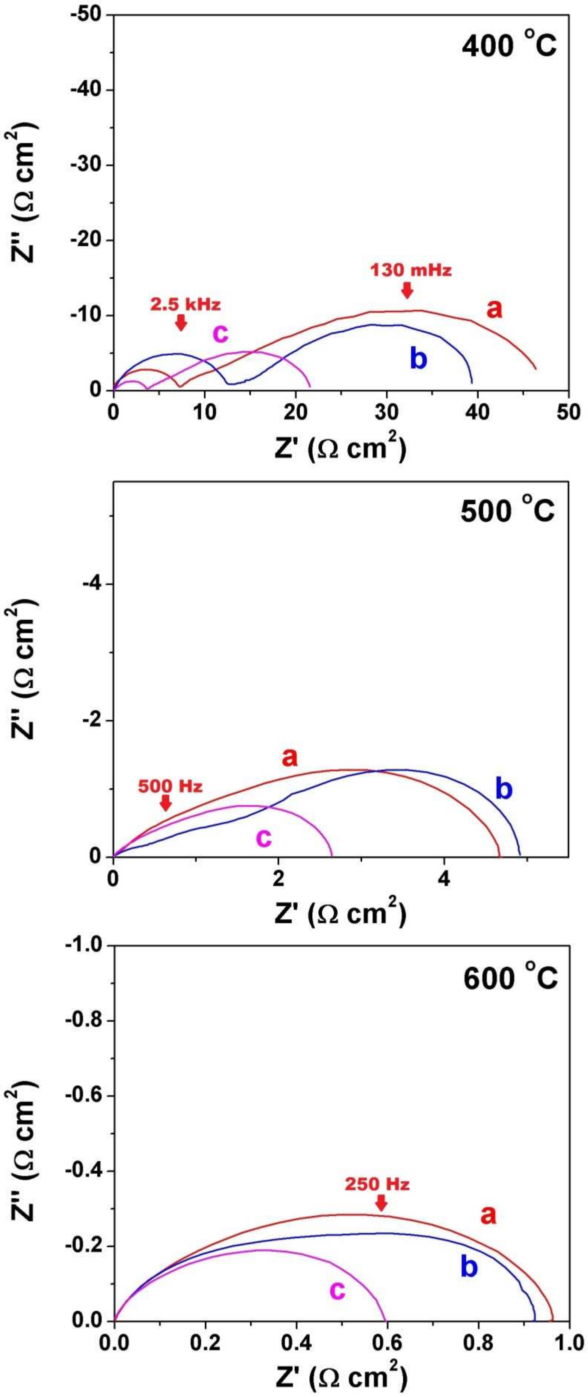

Figure 4.6 Nyquist plots of the (a) $Y_{0.8}In_{0.1}Ca_{0.1}BaCo_3ZnO_{7+\delta}$ + GDC, (b) $Y_{0.5}In_{0.4}Ca_{0.1}BaCo_3ZnO_{7+\delta}$ + GDC, and (c) $Y_{0.5}In_{0.1}Ca_{0.4}BaCo_3ZnO_{7+\delta}$ + GDC symmetric cells on GDC electrolyte. Frequency markers are included for the $Y_{0.8}In_{0.1}Ca_{0.1}BaCo_3ZnO_{7+\delta}$ + GDC sample at all temperatures.

`

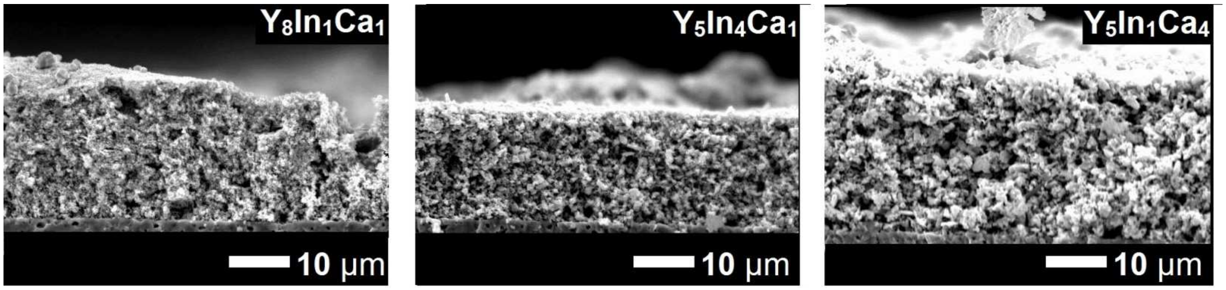

Figure 4.7 SEM micrographs of the (Y,In,Ca)$BaCo_3ZnO_{7+\delta}$ + GDC symmetric cells on GDC electrolyte after testing (tests may be seen in Figures 5 and 6).

The improved performance with increasing Ca content may be understood by the effective change in the oxidation state of the Co ions; by replacing Y^{3+} with Ca^{2+}, Co^{2+} is oxidized to Co^{3+}. Table 4.2 lists the oxidation states of cobalt determined after the 15 h dwell in TGA, where it shows that samples with a larger Ca content tend to have a higher Co oxidation state. Previous work on *perovskite*-based SOFC cathodes has shown that the oxygen reduction reaction (ORR) is strongly dependent on the electronic structure and covalency of the transition metal – oxygen bond.[59,103-105] It has been shown that the ORR kinetics tends to improve as the energy difference between the metal 3*d* and oxygen 2*p* bands decreases and the metal-oxygen covalence increases.[103] As the oxidation state of Co increases in $RBa(Co,M)_4O_{7+\delta}$, the metal-oxygen covalency increases, resulting in a reduction the area-specific resistance of the cathode.

In our previous work, we showed that the composite Y_{10} cathode performed similarly to the well-studied pristine $Ba_{0.5}Sr_{0.5}Co_{0.8}Fe_{0.2}O_{3-\delta}$ (BSCF) cathode at high

`

temperatures, and slightly outperformed BSCF in the 400 – 600 °C range.[29] As $Y_5In_1Ca_4$ shows greater thermal stability and electrochemical performance compared to Y_{10}, this suggests that the fully-stabilized $Y_{0.5}In_{0.1}Ca_{0.4}BaCo_3ZnO_{7+\delta}$ + GDC composite cathode may make an excellent candidate for intermediate- to low-temperature SOFC applications.

4.4 CONCLUSIONS

The effects of R-site composition in the $Y_{1-x-y}In_xCa_yBaCo_3ZnO_{7+\delta}$ ($0.2 \leq x + y \leq 0.5$) series of oxides have been investigated. All samples investigated are stable after 120 h exposure to 600, 700, and 800 °C, showing that a small In content is able to sufficiently stabilize the phase. Unit cell volume decreases with increasing In content and increases with increasing Ca content. The oxidation state of Co increases with increasing In and Ca contents. Increased In content has minimal effect on the electrochemical performance of the composite cathodes, while increased Ca content improves the electrochemical performance. All $(Y,In,Ca)BaCo_3ZnO_{7+\delta}$ samples show improved electrochemical performance over the unsubstituted $YBaCo_3ZnO_{7+\delta}$ base composition. $Y_{0.5}In_{0.1}Ca_{0.4}BaCo_3ZnO_{7+\delta}$ has significantly improved electrochemical performance compared to $Y_{0.8}In_{0.1}Ca_{0.1}BaCo_3ZnO_{7+\delta}$ on GDC symmetric cells at low temperatures. With good long-term stability at all temperatures in the range of 600 – 800 °C and improved low-temperature electrochemical performance, the high-Ca content

`

$(Y,In,Ca)BaCo_3ZnO_{7+\delta}$ series of oxides are an attractive option for intermediate- to low-temperature SOFC cathodes.

`

CHAPTER 5

High-Performance $Y_{0.9}In_{0.1}BaCo_3(Zn,Fe)O_{7+\delta}$ Swedenborgite-Type Oxide Cathodes for Reduced Temperature Solid Oxide Fuel Cells

5.1 INTRODUCTION

As discussed in previous Chapters, one of the main areas of SOFC investigation is to develop cathode materials that can operate in the intermediate-temperature (IT) region (600 – 800 °C) or in the low-temperature region (T < 600 °C).[4,15,16,28,29,37,62,74,88-91,106] As such, it was discussed how *swedenborgite*-type $RBa(Co,M)_4O_{7+\delta}$ (R = Y, In, and Ca; M = Co, Zn, Fe, Ga, and Al) oxides have been shown to have favorable thermal expansion matching and electrochemical performance in these reduced temperature ranges, though they tend to have long-term decomposition problems.[29,37,71,72,74,90,91,106,107] Chapters 3 and 4, along with previous work, have shown that these materials can be stabilized through selective substitutions in both the R and M sites.[29,37,71,72,74,90,91,106,107] One of the most frequently used substitutions is the replacement of Co by Zn as the high concentration of $Co^{2+/3+}$ in the tetrahedral sites is thought to be the main source of instability in these materials.[37] However, Zn^{2+} with a stable $3d^{10}$ configuration diminishes the electronic conductivity and the catalytic activity for the oxygen reduction reaction (ORR), degrading the overall electrochemical performance.[37]

Previous work with the *swedenborgite*-type system for SOFC cathodes has shown that a composition of $YBaCo_3ZnO_{7+\delta}$ has good electrochemical performance but tends to decompose at lower temperatures, while $InBaCo_3ZnO_{7+\delta}$ has lower performance but

`

exhibits superior low-temperature stability.[29,37,74,106] In Chapter 4, it was shown that a composition of $Y_{0.9}In_{0.1}BaCo_3ZnO_{7+\delta}$ is stable at all temperatures, but with an electrochemical performance similar to that of the unsubstituted $YBaCo_3ZnO_{7+\delta}$ cathode.[29] Another frequently used R-site cation is Ca^{2+}, which enhances the electrochemical performance, but severely destabilizes the phase and tends to require an increased Zn content to compensate and stabilize the phase.[37,91] Further investigation of the stabilization effect with In substitution has shown in Chapter 4 that it can successfully stabilize a composition of $Y_{0.5}In_{0.1}Ca_{0.4}BaCo_3ZnO_{7+\delta}$ without requiring an increased Zn substitution.[107] These results suggest that it may be possible to utilize the stability promoting effect of In to reduce the required concentration of Zn, thereby improving the electrochemical performance.

As the octahedral-site stabilization energy (OSSE) of $Co^{2+/3+}$ shows a preference for octahedral coordination, it is likely that replacing Zn with an increasing concentration of Co will rapidly destabilize the phase, leading to decomposition at the operating temperatures.[37,88] However, with an OSSE of zero, Fe^{3+} is far more stable in the tetrahedral sites, while not drastically diminishing the electronic conductivity and ORR activity unlike Zn substitution. Accordingly, we present here an investigation of the $Y_{0.9}In_{0.1}BaCo_3(Zn,Fe)O_{7+\delta}$ series of cathodes with lower Zn contents with the goal of discovering a stable cathode with enhanced electrochemical performance for reduced-temperature SOFCs.

`

5.2 EXPERIMENTAL METHODS

5.2.1 Materials Synthesis

The $Y_{0.9}In_{0.1}BaCo_3(Zn,Fe)O_{7+\delta}$ samples were synthesized by conventional solid state reaction (SSR) methods as discussed in Chapter 2. Required amounts of Y_2O_3, In_2O_3, $BaCO_3$, Co_3O_4, ZnO, and Fe_3O_4 were mixed with ethanol in an agate mortar and pestle for 1 h, dried, pressed into pellets, and calcined at 1000 °C for 12 h.[29,37,74,90,91,106,107] The resultant pellets were then ground into powder, pressed again, and sintered at 1200 °C for 24 h. After sintering, the pellets were annealed in air at 900 °C for 6 h and slowly cooled to room temperature at a rate of 1 °C min^{-1}.[29,107]

The $Y_{0.2}Ce_{0.8}O_{1.9}$ (YDC) electrolyte powder was synthesized by the glycine nitrate process (GNP) as discussed in the previous Chapters. The $Gd_{0.2}Ce_{0.8}O_{1.9}$ (GDC) powders were synthesized by SSR and GNP methods as discussed in the previous Chapters.

5.2.2 Materials Characterization

After synthesis and annealing, the $Y_{0.9}In_{0.1}BaCo_3(Zn,Fe)O_{7+\delta}$ powders were characterized by x-ray diffraction (XRD) with Cu K_α radiation. The XRD patterns were analyzed with the MDI Jade program (www.materialsdata.com) and refined to calculate the lattice parameters.

The long-term phase stabilities of the $Y_{0.9}In_{0.1}BaCo_3(Zn,Fe)O_{7+\delta}$ samples were determined as outlined in Chapter 3. Thermogravimetric analysis (TGA) (Netzsch STA

`

449 F3) was utilized to determine the change in oxygen content during thermal cycling as discussed in Chapters 3 and 4.

5.2.3 Electrochemical Characterization

Composite cathodes were manufactured by ball-milling equal parts by mass of $Y_{0.9}In_{0.1}BaCo_3(Zn,Fe)O_{7+\delta}$ and GDC powders in ethanol for 36 – 48 h.[29,90,107] The composite cathodes were then dried and mixed with an organic binder (Heraeus V006) in a 60 : 40 cathode : binder weight ratio to create an ink.[29,107] YDC inks were prepared by mixing the YDC powder with the binder in a 50 : 50 ratio without prior ball milling.[29,107]

The polarization resistances (R_p) of the composite cathodes were measured on 8 mol % yttria stabilized zirconia (8YSZ) electrolyte supported symmetric cells in the range of 400 – 800 °C by AC impedance spectroscopy as discussed in the previous Chapters. The thickness of the electrolyte supports was between 150 – 200 μm (FuelCellMaterials.com). YDC interlayers between the cathode and electrolyte were utilized to prevent interfacial reactions, and were applied as discussed in previous Chapters. The composite cathode layers were screen printed three times on each side and sintered for 3 h at 900 °C.[29,37,74,90,91,106,107] The effective area of the electrodes was 0.25 cm^2. After sintering the cathode, silver current collectors were applied as discussed in previous Chapters. The symmetric cells were allowed to dwell at 400 °C for 1 - 2 h before testing. R_p values of the selected $Y_{0.9}In_{0.1}BaCo_3(Zn,Fe)O_{7+\delta}$ composite cathodes were measured on 250 μm thick GDC electrolytes (FuelCellMaterials.com) for a

`

comparison at lower temperatures.[29,107] The symmetric cells were manufactured similarly to those on 8YSZ electrolytes, although without the YDC buffer layer due to the lack of side reactions. After testing, the microstructures of the symmetric cells were observed using a JEOL JSM-5610 scanning electron microscope (SEM).

5.3 RESULTS AND DISCUSSION

5.3.1 Crystal Chemistry and Phase Stability

The room-temperature XRD patterns of selected $Y_{0.9}In_{0.1}BaCo_3Zn_{1-x}Fe_xO_{7+\delta}$ samples are presented in Figure 5.1. All samples in the range of $0 \leq x \leq 0.8$ are single-phase materials with the *P31c* phase group, analogous to other $RBaCo_3ZnO_7$ (R = Y, In, Ca) materials.[29,74,107] On the other hand, both the x = 0.9 and x = 1.0 samples were not single-phase after sintering at 1200 °C for 24 h, with many unidentified peaks appearing in their XRD patterns. Some of the observed impurity peaks align well with various barium iron oxide phases, which correlates well with the previous work where $BaCoO_3$ was the major impurity phase, but the number of peaks and the possible phases with the presence of six cations make definitive phase identification challenging.[29,74] Unit cell parameters of the single-phase samples obtained by the refinement of the XRD patterns are given in Table 5.1. The data indicate that the lattice parameters do not significantly change with the substitution of Fe for Zn, although a slight increase in unit cell volume with increasing Fe content is observed.

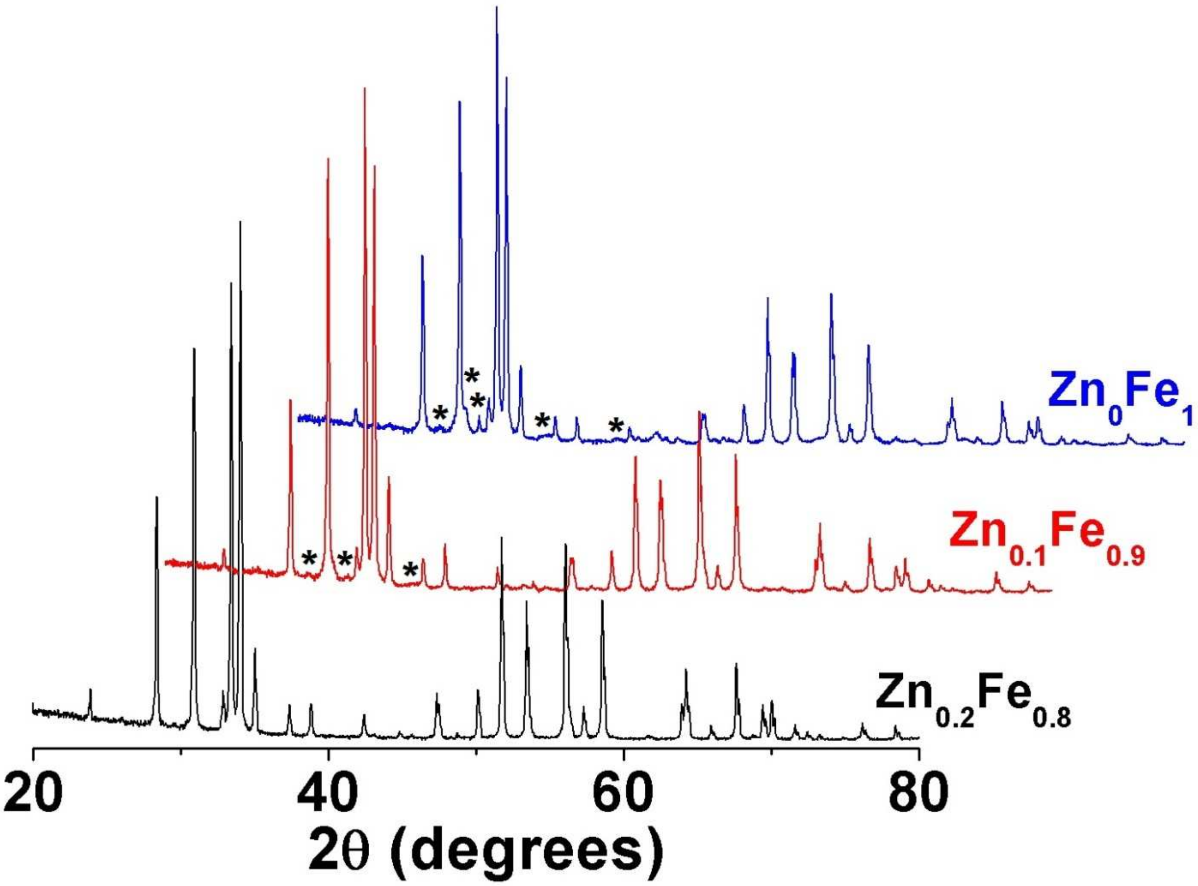

Figure 5.1 Room-temperature XRD patterns of selected as-synthesized $Y_{0.9}In_{0.1}BaCo_3Zn_{1-x}Fe_xO_{7+\delta}$ oxides before long-term stability testing. All samples with x < 0.8 are single-phase oxides with the *P31c* space group. The * in the x = 0.9 and 1.0 samples denote impurity phases.

Table 5.1 Unit cell parameters, high-temperature phase stability, and activation energies of the $Y_{0.9}In_{0.1}BaCo_3Zn_{1-x}Fe_xO_{7+\delta}$ oxides and composite cathodes

x	a (Å)	c (Å)	Volume (Å^3)	Stability (120 h)			E_a (eV)*
				600 °C	700 °C	800 °C	
0.0	6.308	10.274	354.03	✓	✓	✓	1.24
0.2	6.312	10.275	354.51	✓	✓	✓	1.28
0.4	6.313	10.274	354.59	✓	X	✓	1.25
0.6	6.315	10.278	354.95	✓	X	X	N/A
0.8	6.312	10.277	354.58	✓	X	X	N/A

* Values calculated in the range of 433 – 766 °C

The room-temperature oxygen content values of all single-phase samples obtained by iodometric titration after annealing at 900 °C are given in Table 5.2. All the samples show oxygen contents of 7.24 to 7.27. These variations are quite small and are within experimental error; for a reference, in our previous work on $Y_{1-x}In_xBaCo_3ZnO_{7+\delta}$ ($0 \leq x \leq 0.5$), the oxygen contents varied between 7.13 and 7.24.[29] The similarity of oxygen content across the samples can also help explain the relative similarity in lattice volumes. For the samples with $0 \leq x \leq 0.6$, the slight increase in lattice volume can be attributed to the slightly larger ionic radius of Fe^{2+} (0.63 Å) compared to that of Zn^{2+} (0.60 Å).[93] As for the x = 0.8 sample, its higher oxygen content leads to an oxidation of Co^{2+} and Fe^{2+} (0.58 and 0.63 Å) to smaller Co^{3+} and Fe^{3+} ion (0.49 Å for both), resulting in a reduction in lattice volume.

Table 5.2 Oxygen contents of the $Y_{0.9}In_{0.1}BaCo_3Zn_{1-x}Fe_xO_{7+\delta}$ oxides

x	Initial value (25 °C)	After 15 h dwell In TGA at 900 °C	After final cooling in TGA to 80 °C
0.0	7.24	7.09	7.07
0.2	7.25	7.21	7.22
0.4	7.25	7.21	7.22
0.6	7.23	7.21	7.24
0.8	7.27	7.38	7.45

`

The long-term phase stabilities of all the single-phase $Y_{0.9}In_{0.1}BaCo_3Zn_{1-x}Fe_xO_{7+\delta}$ samples in the range of $0 \leq x \leq 0.8$ are presented in Figure 5.2. As can be seen, both the x = 0.0 and x = 0.2 samples are stable after exposure to all temperatures of interest. The x = 0.6 and x = 0.8 samples show stability at 600 °C, but decompose at both 700 and 800 °C; significant decomposition is observed, making the identification of the phases difficult. The x = 0.4 sample, interestingly, shows stability at both 600 and 800 °C, but shows a $BaCoO_3$ impurity phase after 120 h exposure to 700 °C. This result was verified multiple times to ensure repeatability of the results, and the $BaCoO_3$ phase is a well-known decomposition product of similar materials.[29,37,74] This result affirms that increased Fe content compromises lattice stability, and a significant Zn content is required to maintain the phase-stability at all temperatures of interest. Other work on the phase stability of similar materials, $YBaCo_{3+x}(Ge,Al)_{1-x}O_{7+\delta}$ series, have found that samples with Co content > 3.2 tend to show decomposition or phase impurities.[67] Interestingly in this work, we find that a (Co,Fe) content of 3.4 in the lattice is stable at both high and low temperatures, in contrast with previous work where instability occurs either above or below certain temperature thresholds.[29,37,74,90,91,106,107] The reason for the x = 0.4 sample's instability at 700 °C is uncertain, and should be investigated further with future work.

`

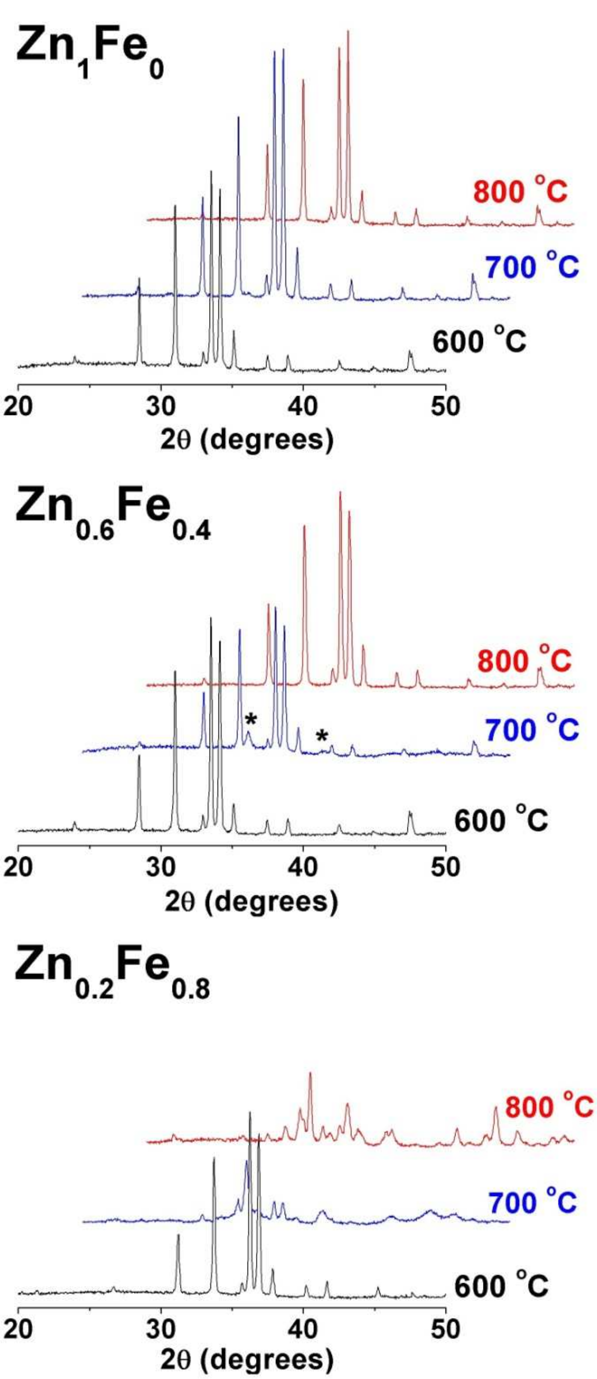

Figure 5.2 Room-temperature XRD patterns of the $Y_{0.9}In_{0.1}BaCo_3Zn_{1-x}Fe_xO_{7+\delta}$ ($0 \leq x \leq 0.8$) oxides after 120 h exposure to 600, 700, and 800 °C. The * in the x = 0.4 sample at 700 °C denote the generated $BaCoO_3$ impurity. The impurities generated in the x = 0.6 and 0.8 samples at 700 and 800 °C are unidentified due to the severity of the phase decomposition.

5.3.2 Thermal Properties and Electrochemical Performance

The variations in oxygen content with temperature of the $Y_{0.9}In_{0.1}BaCo_3Zn_{1-x}Fe_xO_{7+\delta}$ oxides were determined by TGA, with all mass loss/gain attributed to variations in oxygen content. The data gathered with TGA are shown in Figure 5.3, with Figure 5.3a giving a full trace of $Y_{0.9}In_{0.1}BaCo_3Zn_{0.6}Fe_{0.4}O_7$ as a reference. The samples were allowed to anneal for 15 h at 900 °C to stabilize the oxygen contents; for ease of reference, these data are listed in Table 5.2 along with the room-temperature oxygen content values and the oxygen content values after the final cooling of the samples in the TGA to 80 ^{o}C. As can be seen in Figure 5.3, the oxygen contents during the final heating and cooling cycles are similar, in contrast to the larger variations observed during previous steps of the TGA measurement. This trend was observed in all samples, and it correlates well with previous work.[29,74,107] Figure 5.3b shows the oxygen contents of all single-phase samples ($0 \leq x \leq 0.8$) with time after the annealing process. This data show that the reversible absorption/desorption of oxygen during thermal cycling tends to increase with increasing Fe content. This trend can be understood to be due to the replacement of Zn^{2+} with a fixed valence by the transition-metal ion $Fe^{2+/3+}$ with a variable valence; the increase in ions with variable oxidation states allows for an increased oxygen variation during thermal cycling. The increased oxygen absorption capacity of the samples with a larger Fe content can also be used to explain their instability at higher temperatures, as previous work has determined that compounds with larger oxygen absorption are more likely to decompose at high temperatures.[67]

`

Figure 5.3c shows the final cooling curves of all single-phase oxides for clarity. In this figure, it can be observed that the oxygen content after the final cooling cycle to 80 ^{o}C increases with increasing Fe content, although the $0.2 \leq x \leq 0.6$ samples all show relatively similar oxygen contents. Previous work has shown that the interstitial excess oxygen in *swedenborgite*-type materials tend to orient itself around the (Co,M)$^{n+}$ ions in tetrahedral sites.[94] As the concentration of the fixed-valent Zn^{2+} ion decreases, an increase in tetrahedra with variable oxidation states lead to an increase in oxygen storage capacity. Previous work has also shown that an increasing concentration of ions with a fixed oxidation states (*e.g.,* Zn^{2+}, Al^{3+}, Ga^{3+}) decreases the oxygen storage capacity, which further supports our observations.[37,67,74,91]

`

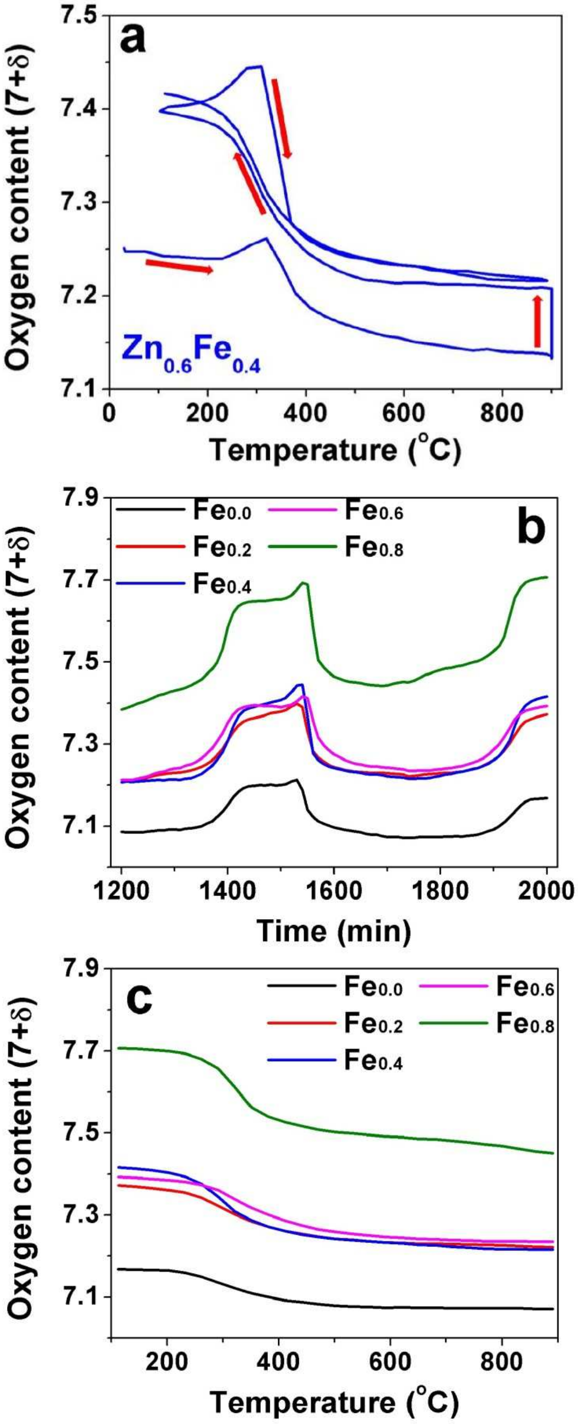

Figure 5.3 Variations in oxygen content as observed via TGA of all the single-phase $Y_{0.9}In_{0.1}BaCo_3Zn_{1-x}Fe_xO_{7+\delta}$ ($0 \leq x \leq 0.8$) oxides: (a) full trace of the x = 0.4 sample for a reference, with the arrows denoting directionality; (b) oxygen content with time after 15 h annealing at 900 °C; and (c) final cooling curve of all samples to 80 ^{o}C.

`

Electrochemical performances of the $Y_{0.9}In_{0.1}BaCo_3Zn_{1-x}Fe_xO_{7+\delta}$ oxides were characterized by AC impedance spectroscopy on cathode | YDC | electrolyte | YDC | cathode symmetric cells. Composite cathodes were utilized as previous research has found $RBa(Co,M)_4O_{7+\delta}$ type oxides to have relatively low oxygen transport properties.[37,90] The composite cathodes were manufactured with 50:50 wt% cathode:GDC, as previous research found this to be the ideal composition for $YBaCo_3ZnO_{7+\delta}$.[90] Previous work has found that the performance of this class of materials is dependent on the three-phase boundary (TPB) region, which is the surface area shared by the cathode, electrolyte, and oxidant.[29,73,74,90,91,106,107] Accordingly, the powders were ball-milled to maximize homogeneity and decrease particle size to increase the size of the TPB. As 8YSZ is known to react with both cobalt and gadolinium to form non-conductive interface layers, YDC was utilized as a buffer layer to prevent reaction.[29,35,36,107] Silver was used for the cathode current collector due to its high electrical conductivity and oxygen reduction properties.[96-98] The silver current collector was assembled as a self-assembling micron-scale mesh as described in Chapter 3, due to its high performance.

Figure 5.4 shows the Arrhenius plots of the polarization resistances (R_ps) of the more stabilized $Y_{0.9}In_{0.1}BaCo_3Zn_{1-x}Fe_xO_{7+\delta}$ + GDC ($0 \leq x \leq 0.4$) composite cathodes on 8YSZ electrolyte-supported symmetric cells in the range of 400 – 800 °C. Previous work has shown that the diameter of the impedance loop can be used to calculate the polarization resistances of the cathodes in cells where the electrolyte has negligible conductivity.[99-101] As 8YSZ has negligible electronic conductivity in this range, the

`

difference between the low and high frequency intercepts was used to calculate the polarization resistances of these cathodes. Figure 5.4 shows that the electrochemical performances of the $Y_{0.9}In_{0.1}BaCo_3Zn_{1-x}Fe_xO_{7+\delta}$ + GDC composite cathodes increase with increasing Fe content. The performance inhibiting nature of Zn^{2+} in this series of oxides is well documented; its $[Ar]3d^{10}$ electronic configuration is exceptionally stable, and as such it cannot be further oxidized or reduced, prohibiting it from participating in electronic transport and oxygen reduction.[37,58,59,74,91,103-106] By replacing Zn^{2+} with $Fe^{2+/3+}$, the material gains additional electrochemically active sites, significantly boosting the performance. Figure 5.4b compares the performance of the x = 0.4 sample with the well-studied $Ba_{0.5}Sr_{0.5}Co_{0.8}Fe_{0.2}O_{3-\delta}$ (BSCF) as a reference. While the x = 0.4 sample is in a composite cathode, the BSCF sample was manufactured as single-phase due to its mixed ionic and electronic conduction properties. In the previous work, we investigated a composite BSCF cathode with the same weight ratio as our *swedenborgite*-type composite cathodes; the composite BSCF was shown to have reduced performance in the lower temperature regions (T < 600 °C).[29] With its reduced activation energy, the $Y_{0.9}In_{0.1}BaCo_3Zn_{0.6}Fe_{0.4}O_{7+\delta}$ + GDC composite cathode significantly outperforms the single-phase BSCF in the reduced temperature region; however, BSCF begins to outperform the x = 0.4 sample at around 700 °C.

`

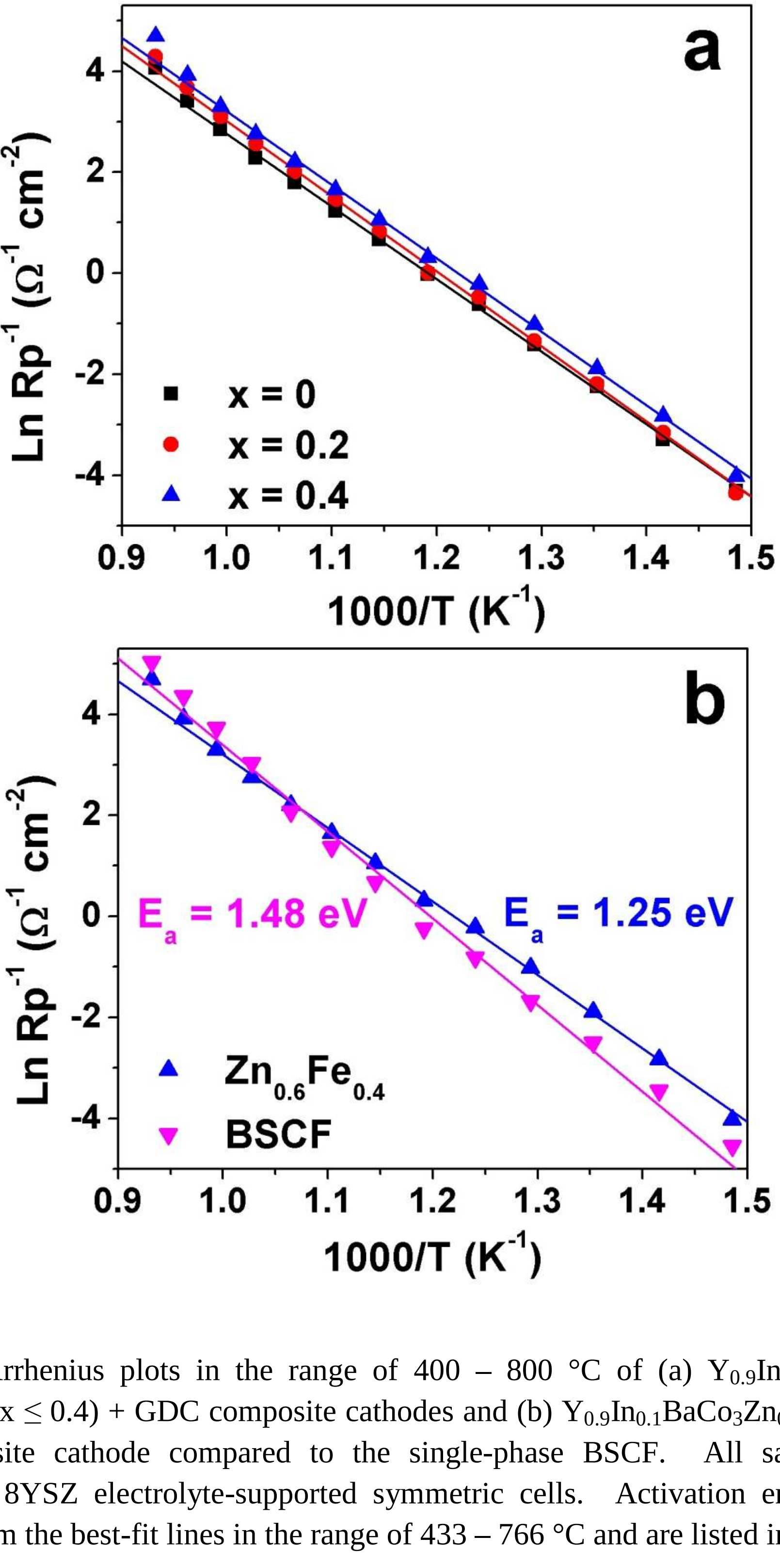

Figure 5.4 Arrhenius plots in the range of 400 – 800 °C of (a) $Y_{0.9}In_{0.1}BaCo_3Zn_{1-x}Fe_xO_{7+\delta}$ ($0 \leq x \leq 0.4$) + GDC composite cathodes and (b) $Y_{0.9}In_{0.1}BaCo_3Zn_{0.6}Fe_{0.4}O_{7+\delta}$ + GDC composite cathode compared to the single-phase BSCF. All samples were measured on 8YSZ electrolyte-supported symmetric cells. Activation energies were calculated from the best-fit lines in the range of 433 – 766 °C and are listed in Table 5.1.

`

Figure 5.5 shows the area normalized Nyquist plots of $Y_{0.9}In_{0.1}BaCo_3Zn_{1-x}Fe_xO_{7+\delta}$ + GDC composite cathodes on 8YSZ symmetric cells in the temperature range of 433 – 600 °C. According to Adler *et al.*, impedance arcs at higher frequencies are attributed to charge transfer across the cathode/electrolyte interface and electronic transfer across the cathode, and impedance arcs at the lower frequencies are attributed to the oxygen adsorption and reduction reactions.[58,99] At all temperatures, the diameter of the low-frequency arc decreases with increasing Fe content. As previously discussed, Zn^{2+} does not contribute to the oxygen reduction reaction, so this result is expected. Interestingly, the diameter of the high-frequency arc is also diminished in the $x = 0.4$ sample, compared to the others. Figure 5.6 shows the cross-sectional SEM micrographs of these symmetric cells after testing, where all samples show similar microstructures. As there is no observable difference in microstructure for the $x = 0.4$ sample, this reduction in impedance is attributed to the higher oxygen content at elevated temperatures and increased electronic conductivity due to the increased Fe content. As the temperature increases, the high-frequency arc reduces drastically in all samples, signifying that at higher temperatures the oxygen reduction reaction is the primary limitation. This correlates well to previous work on similar materials.[29,107]

`

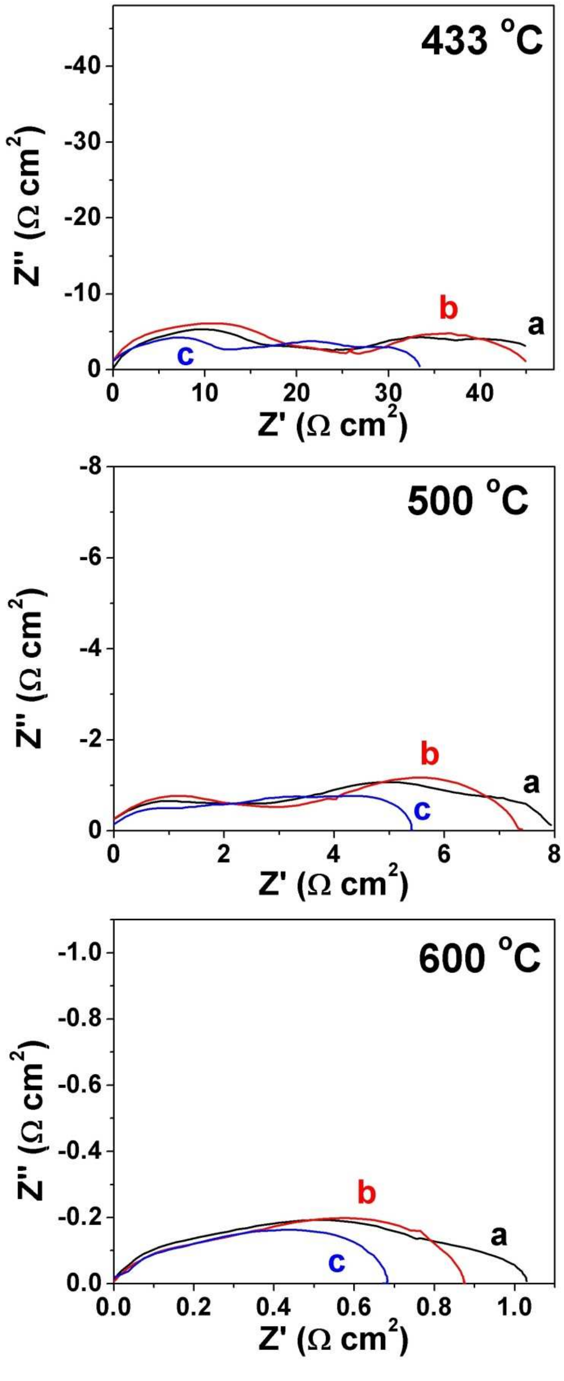

Figure 5.5 Area-normalized Nyquist plots of the $Y_{0.9}In_{0.1}BaCo_3Zn_{1-x}Fe_xO_{7+\delta}$ + GDC composite cathodes on 8YSZ electrolyte-supported symmetric cells: (a) x = 0, (b) x = 0.2, and (c) x = 0.4.

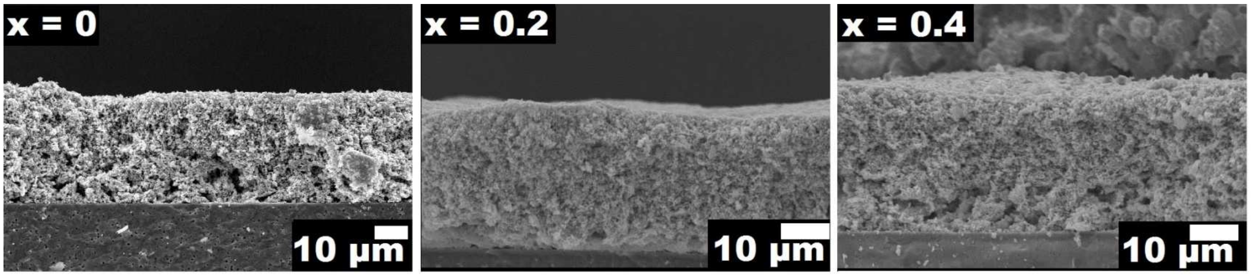

Figure 5.6 Cross-sectional SEM micrographs of the $Y_{0.9}In_{0.1}BaCo_3Zn_{1-x}Fe_xO_{7+\delta}$ + GDC composite cathodes on 8YSZ electrolyte-supported symmetric cells after testing. Performances of these cells are presented in Figures 5.4 and 5.5.

Figure 5.7a shows the Arrhenius plots of the R_ps of two $Y_{0.9}In_{0.1}BaCo_3Zn_{0.6}Fe_{0.4}O_{7+\delta}$ + GDC composite cathodes on GDC electrolyte; one with GDC synthesized by SSR, and another with GDC synthesized by GNP. Powders synthesized by GNP have an exceptionally small particle size, greatly increasing the surface area per mass ratio.[75,76] Previous work by our group has shown that the inclusion of GNP-synthesized GDC can reduce the polarization resistance of these materials by increasing the size of the TPB.[29] In Fig. 5.7a, it can be seen that the inclusion of GDC powder synthesized by GNP reduces the polarization resistances at higher temperatures, signifying improved electrochemical performance. At lower temperatures both samples have similar performances, though the sample with GDC by SSR has slightly reduced impedance. Figure 5.7b shows the area-normalized Nyquist plots of both samples at 500 °C. The data show that the higher-frequency arc of the GDC by GNP sample is significantly expanded, while the low-frequency arc is nearly identical for both samples. The expansion of the high-frequency arc can be understood to be due to the increased interfacial impedance from increased cathode/electrolyte surface area. The similarity of the low-frequency arcs, on the other hand, suggests that at lower temperatures the expansion of the three-phase boundary region has negligible impact on the oxygen reduction reaction. Further work should focus on optimizing the composite cathode ratio as a different ratio may be ideal due to the reduction of dependence on the three phase boundary.

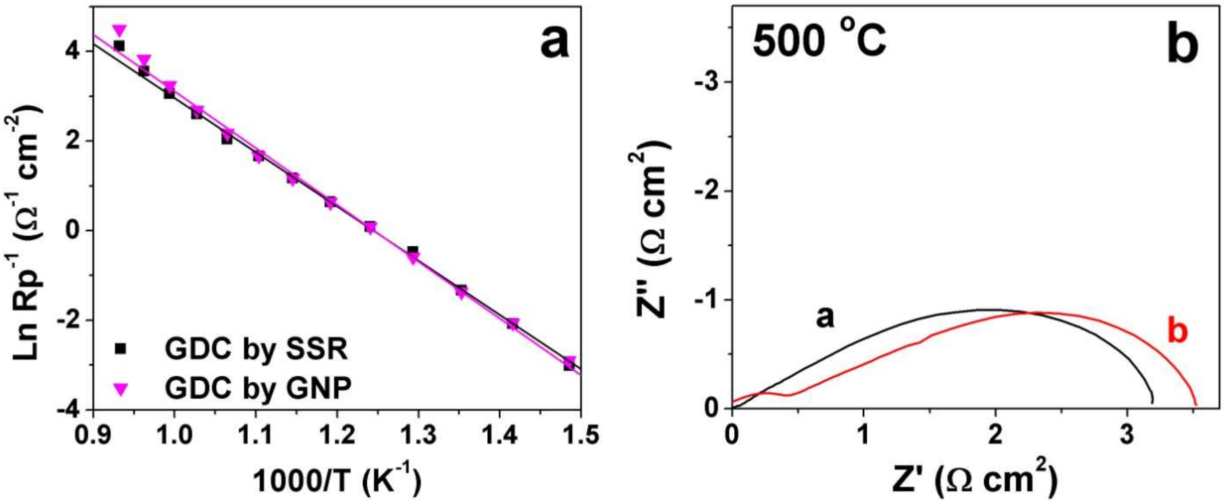

Figure 5.7 Symmetric cell tests comparing $Y_{0.9}In_{0.1}BaCo_3Zn_{0.6}Fe_{0.4}O_{7+\delta}$ composite cathodes with both GDC synthesized by solid state reaction and by GNP on GDC electrolyte supports. (a) Arrhenius plots of polarization resistance in the range of 400 – 800 °C and (b) Nyquist plots of these cells at 500 °C.

`

5.4 CONCLUSIONS

The effects of Fe substitution in the $Y_{0.9}In_{0.1}BaCo_3Zn_{1-x}Fe_xO_{7+\delta}$ series of oxides have been investigated systematically. All samples in the range of $0 \leq x \leq 0.8$ are single-phase materials and have similar room-temperature oxygen contents, although the samples with higher Fe content show a larger capacity for reversible oxygen absorption. Both the x = 0.0 and 0.2 samples are stable in the 600 – 800 °C range after 120 h exposure, while the x = 0.6 and 0.8 samples show significant phase decomposition at 700 and 800 °C. Interestingly, the x = 0.4 sample is metastable at both 600 and 800 °C, although $BaCoO_3$ reaction products are produced at 700 °C. Electrochemical performances of the more stable compounds ($0 \leq x \leq 0.4$) were investigated with AC impedance spectroscopy, which shows that higher Fe content leads to reduced cathode polarization resistance. The x = 0.4 composite cathode exhibits a significant increase in performance compared to the well-studied single-phase BSCF cathode at temperatures below 700 °C, revealing that the $Y_{0.9}In_{0.1}BaCo_3Zn_{0.6}Fe_{0.4}O_{7+\delta}$ composite cathode is an attractive option for reduced temperature solid oxide fuel cells.

CHAPTER 6

Layered $LnBa_{1-x}Sr_xCoCuO_{5+\delta}$ (Ln = Nd and Gd) Perovskite Cathodes for Intermediate Temperature Solid Oxide Fuel Cells

6.1 INTRODUCTION

As discussed in the previous Chapters, studies have shown that the oxygen reduction reaction (ORR) rate in traditional SOFC cathodes is highly dependent on surface chemistry, specifically the triple phase boundary (TPB), or the interfacial area shared by the electrolyte, cathode, and oxidant.[73] In order to overcome this dependency, attention has been focused on cathode materials that are mixed ionic and electronic conductors (MIECs), *i.e.* cathodes that can conduct both O^{2-} ions and electrons, allowing the ORR to occur at all cathodic surface area in contact with the oxidant.[58] A number of perovskite-based structures display MIEC properties, and one of the most promising of these is the recently investigated layered $AA'B_2O_{5+\delta}$ (A = Ba and A' = lanthanide and B = transition metal) perovskite. Due to the large difference between their ionic radii, the Ba^{2+} and Ln^{3+} cations tend to order along the *c* axis with the oxygen vacancies located predominantly in the Ln planes as the Ln^{3+} ions prefer lower coordination numbers.[62]

The $LnBaCo_2O_{5+\delta}$ (Ln = lanthanide) series of oxides is one of the best-studied layered perovskite systems. Previous studies on this system have shown that it is highly amenable to cationic substitutions.[79,88] For example, the substitution of Sr for Ba in $LnBa_{1-x}Sr_xCo_2O_{5+\delta}$ (Ln = Nd and Gd) resulted in improved electrical conductivity, but it also increased the thermal expansion coefficient (TEC) at high temperatures, which can

`

cause delamination of the cathode during cycling.[88] In contrast, the substitution of Cu for Co in $LnBaCo_{2-x}Cu_xO_{5+\delta}$ (Ln = Nd and Gd) decreased the TEC, but it also decreased the electrical conductivity and melting temperature, making it difficult to synthesize without secondary phases.[79]

To utilize the advantageous, positive effects of both the Sr and Cu substitutions, this study focuses on the $LnBa_{1-x}Sr_xCoCuO_{5+\delta}$ (Ln = Nd and Gd, and $0 \leq x \leq 1$) system. The Co : Cu ratio of 1 : 1 was chosen based on a previous study that showed the optimal performance for the $LnBaCo_{2-x}Cu_xO_{5+\delta}$ (Ln = Nd and Gd) system around x = 1.0.[79] Accordingly, the effects of Sr content on the crystal chemistry, oxygen content, electrical conductivity, and electrochemical performance in SOFC of $LnBa_{1-x}Sr_xCoCuO_{5+\delta}$ (Ln = Nd and Gd, and $0 \leq x \leq 1$) are presented.

6.2 EXPERIMENTAL METHODS

The $LnBa_{1-x}Sr_xCoCuO_{5+\delta}$ (Ln = Nd and Gd) samples were synthesized by conventional solid state reactions. Required quantities of Gd_2O_3 (or Nd_2O_3), $BaCO_3$, $SrCO_3$, Co_3O_4, and CuO were mixed with ethanol in an agate mortar and pestle, pressed into pellets, and decarbonated at 850 °C in air for 6 h. The resultant powders were ground, pressed into pellets, and sintered at 960 °C for 12 h. Two to three additional steps of grinding and sintering were carried out at varying temperatures in the range of 970 – 1000 ^{o}C to achieve single-phase samples while avoiding melting of the samples.[79]

`

The resulting powders were annealed in air at 900 °C and slowly cooled to room temperature at a rate of 1 °C min^{-1} to maximize the oxygen content.

The resultant products were characterized by X-ray diffraction (XRD) with Cu Kα radiation, and the Rietveld method was employed to refine the data with the aid of the FullProf program.[80] Thermal expansion data were obtained with a dilatometer (Linseis L75H) as described in Chapter 2. Electrical conductivity data were gathered using a four probe dc method in the Van der Pauw configuration during a cooling cycle from 900 to 40 °C at 20 °C intervals.[85,86] The oxidation state of (Co,Cu) and oxygen content at room temperature were determined by iodometric titration as described in Chapter 2. Thermogravimetric analysis (TGA) data were collected from room temperature to 900 °C at a heating/cooling rate of 2 °C min^{-1} in air with a Netzsch STA 449 F3 thermal analysis system. The samples used in the titration and TGA analysis were first annealed at 900 ^{o}C and cooled to room temperature at a rate of 0.5 ^{o}C min^{-1} to maximize the oxygen content values in the samples. $Gd_{0.1}Ce_{0.9}O_{1.95}$ (GDC) and $La_{0.4}Ce_{0.6}O_{1.8}$ (LDC) were synthesized by the glycine nitrate combustion process (GNP) as described in Chapter 2.

The polarization resistances (R_P) of the $LnBa_{1-x}Sr_xCoCuO_{5+\delta}$ (Ln = Nd and Gd) cathodes on LSGM electrolyte-supported symmetric cells in the range of 550 – 800 °C were determined by ac impedance spectroscopy (Solartron 1260 FRA). To ensure good contact, an intermediate layer of $LnBa_{1-x}Sr_xCoCuO_{5+\delta}$ and LSGM (50 % : 50 % weight ratio) was prepared by mixing with an organic binder (Heraeus V006) to form a slurry, screen-printing onto the dense LSGM electrolyte (0.5 ± 0.05 mm thickness) on both

`

sides, and sintering at 950 °C for 1 h. The cathode layer was prepared by mixing $LnBa_{1-x}Sr_xCoCuO_{5+\delta}$ with the organic binder to form a slurry, screen-printing the slurry on both sides of the intermediate layer three times, and sintering at 950 °C for 3 h. Platinum current collectors were applied by screen-printing platinum paste on both sides and attaching a platinum mesh, followed by sintering at 800 °C for 20 min.

Electrochemical performances of the $LnBa_{1-x}Sr_xCoCuO_{5+\delta}$ cathodes were evaluated on LSGM-electrolyte-supported single cells with GDC / NiO cermet anodes (30 : 70 vol %). The cathode intermediate layer and cathode were prepared as previously described for the symmetric cell. To prevent side-reactions between the LSGM electrolyte and the anode, an intermediate LDC layer was applied in the same manner as for the symmetric cell intermediate layer.[27] The GDC / NiO anode was prepared by ball-milling the required amounts of NiO and GDC powders in ethanol for 24 h. The resultant powder was dried and mixed with an organic binder (Heraeus V006) and then screen-printed onto the intermediate layer three times. The single cell performance was evaluated at 700 – 800 ^{o}C after a 3 h dwell at 800 ^{o}C with air as the oxidant and hydrogen as the fuel, respectively, at 120 and 100 $cm^3\ min^{-1}$. After measurement, the microstructures of the single cells were examined using a JEOL JSM-5610 scanning electron microscope (SEM).

`

6.3. RESULTS AND DISCUSSION

6.3.1 Crystal Chemistry

Figure 6.1 shows the room-temperature XRD patterns of the $LnBa_{1-x}Sr_xCoCuO_{5+\delta}$ (Ln = Nd and Gd) samples for $0 \leq x \leq 1.0$. As mentioned in the experimental section, each sample was prepared at different sintering temperatures to obtain single-phase samples.[79] Previous work has shown that the layered perovskites tend to adopt different space groups depending on their compositions; for example, $GdBa_{1-x}Sr_xCo_2O_{5+\delta}$ was shown to transition from orthorhombic (*Pmmm*) at x = 0 to tetragonal (*P4/mmm*) at $0.2 \leq x \leq 0.6$ to orthorhombic (*Pnma*) at x = 1.0, while $LnBaCo_{2-y}Cu_yO_{5+\delta}$ (Ln = Nd and Gd) was shown to adopt a tetragonal structure (*P4/mmm*) for $0.25 \leq y \leq 1.0$.[79,88] The $LnBa_{1-x}Sr_xCoCuO_{5+\delta}$ (Ln = Nd and Gd) samples in this study with $0 \leq x \leq 0.75$ could all be indexed as tetragonal (*P4/mmm*) similar to $LnBaCoCuO_{5+\delta}$, and they did not undergo any Sr-content-dependent phase transitions unlike the $GdBa_{1-x}Sr_xCo_2O_{5+\delta}$ system.[79,88] This suggests that the substitution of Cu for Co is more influential in determining the structure of this system. As can be seen in Figure 6.2, both the x = 1.0 samples with Ln = Nd and Gd show numerous unidentified peaks. This suggests a solubility limit between $0.75 < x \leq 1.0$ in $LnBa_{1-x}Sr_xCoCuO_{5+\delta}$ (Ln = Nd and Gd). Figure 6.3 shows the Rietveld refinement of $GdBa_{0.5}Sr_{0.5}CoCuO_{5+\delta}$ based on the *P4/mmm* space group, which shows good agreement between the observed and calculated profiles. The qualities of all refinements are listed in Table 6.1.

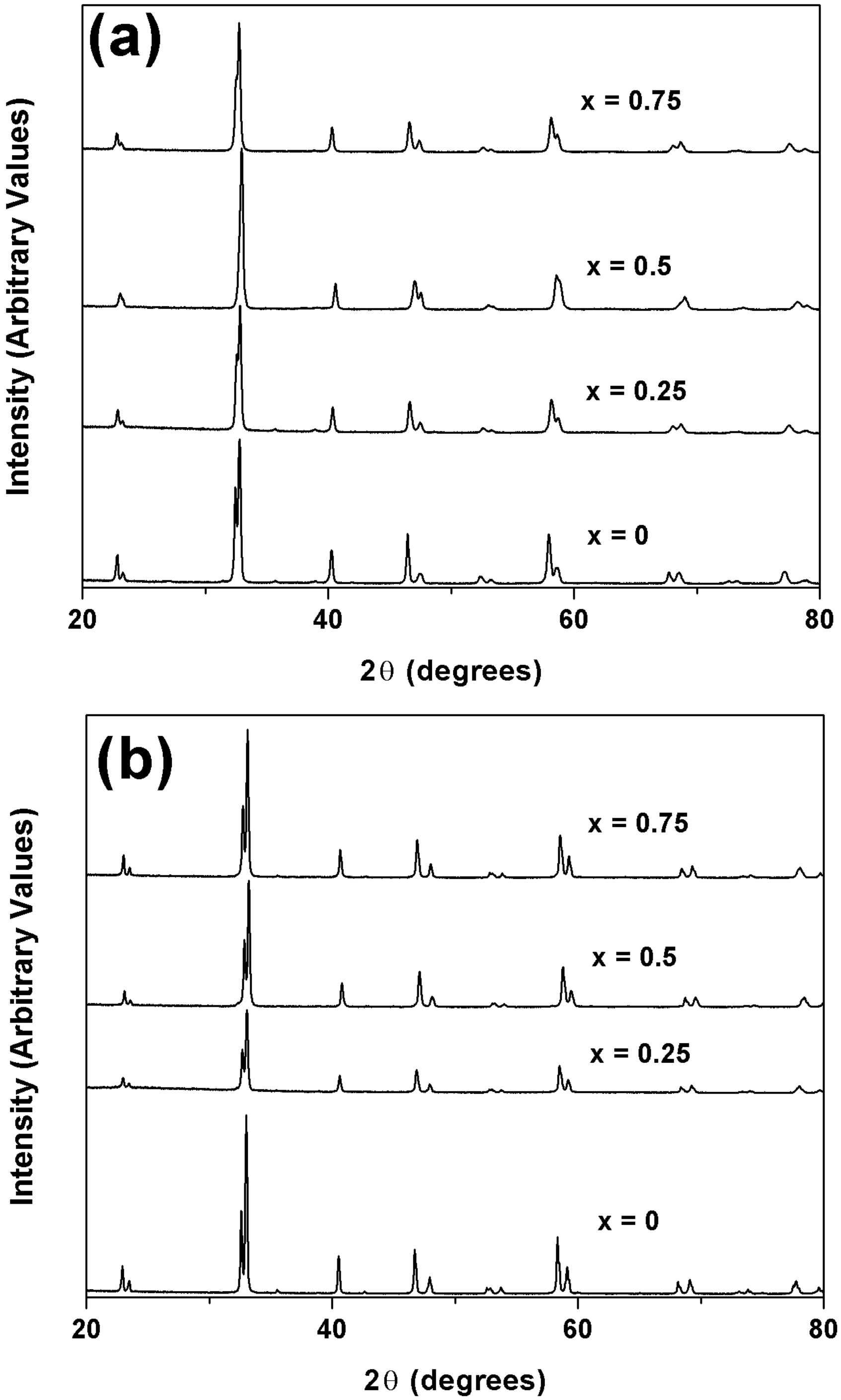

Figure 6.1 Room-temperature XRD patterns of the synthesized (a) $NdBa_{1-x}Sr_xCoCuO_{5+\delta}$ and (b) $GdBa_{1-x}Sr_xCoCuO_{5+\delta}$ samples.

`

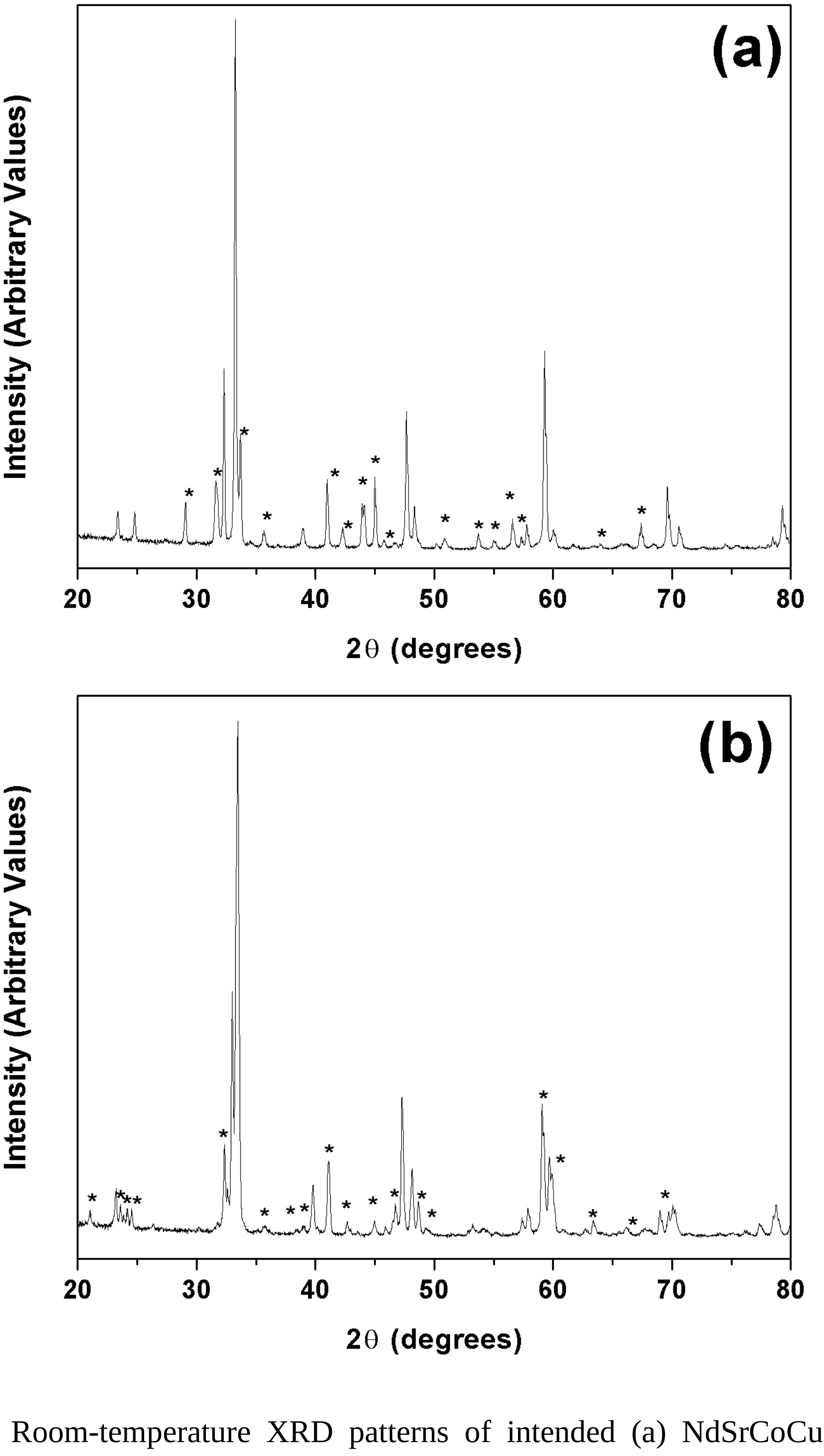

Figure 6.2 Room-temperature XRD patterns of intended (a) $NdSrCoCuO_{5+\delta}$ and (b) $GdSrCoCuO_{5+\delta}$. Peaks marked with * belong to unidentified impurity phases.

`

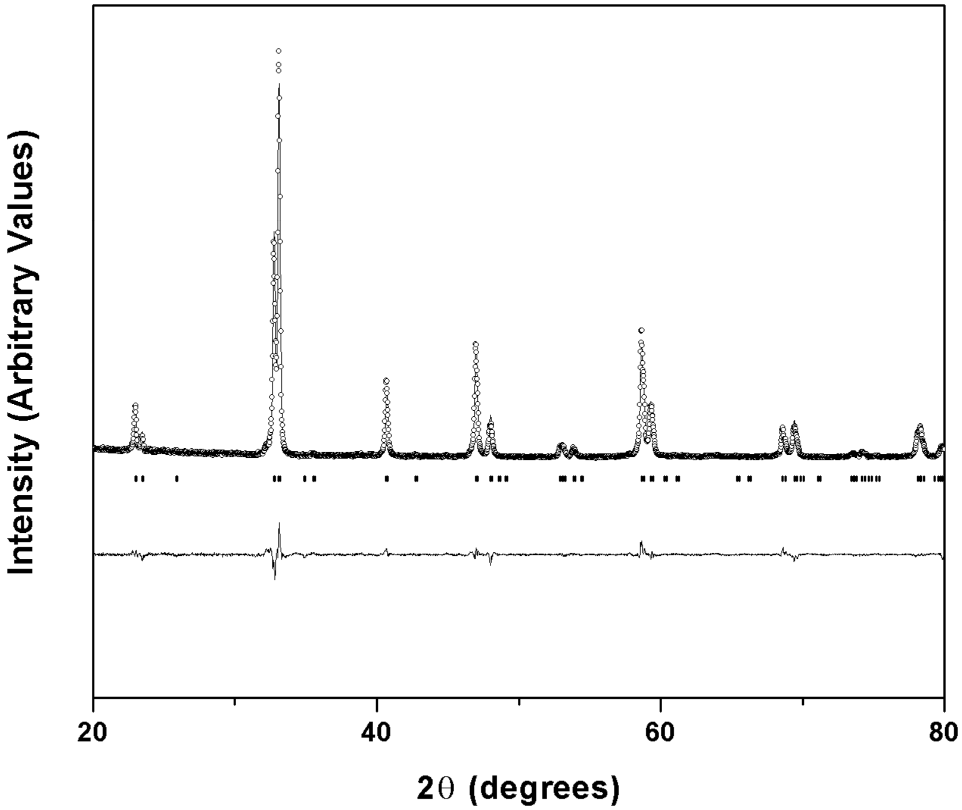

Figure 6.3 Observed and calculated XRD profiles, the differences between them, and peak positions for $GdBa_{0.5}Sr_{0.5}CoCuO_{5+\delta}$. The quality of refinement was found to be χ^2 = 3.36 and R_{bragg} = 4.94.

`

Table 6.1 Structural and compositional parameters of $LnBa_{1-x}Sr_xCoCuO_{5+\delta}$ (Ln = Nd and Gd) oxides

Ln	x	*a* (Å)	*c* (Å)	V (Å^3)	R_{bragg}	χ^2	Lattice distortion (c/2a)	Oxygen content (5+δ)*	(Co,Cu) oxidation*
Nd	0.00	3.920	7.683	118.049	3.610	4.590	0.9801	5.782	3.283
	0.25	3.900	7.672	116.708	2.330	2.170	0.9835	5.753	3.252
	0.50	3.871	7.664	114.851	2.100	3.330	0.9899	5.789	3.289
	0.75	3.894	7.667	116.257	2.270	2.170	0.9845	5.694	3.194
Gd	0.00	3.894	7.604	115.288	3.510	4.680	0.9764	5.643	3.143
	0.25	3.880	7.596	114.331	3.340	1.980	0.9790	5.681	3.181
	0.50	3.866	7.576	113.231	4.940	3.360	0.9799	5.662	3.162
	0.75	3.880	7.593	114.304	5.020	3.250	0.9785	5.581	3.081

***** The oxygen content values and the oxidation state values were determined from furnace-cooled powder samples at room temperature.

`

The data in Table 6.1 also lists the room-temperature unit cell parameters as well as the room-temperature oxygen content values. The unit cell volume of $LnBa_{1-x}Sr_xCoCuO_{5+\delta}$ decreases with Sr content for $0 \le x \le 0.5$ due to the substitution of smaller Sr^{2+} for the larger Ba^{2+} ions.[93] However, the trend reverses at x = 0.75 and the unit cell volume increases. This is due to the decrease in oxygen content and the consequent reduction of the $(Co,Cu)^{n+}$ ions to a larger size.[93]

As all of these compounds were sintered at different temperatures to achieve a single-phase, a direct comparison of their oxygen contents is difficult, as was noted with the $LnBaCo_{2-y}Cu_yO_{5+\delta}$ series.[79] In the $GdBa_{1-x}Sr_xCo_2O_{5+\delta}$ series, it was found before that as the Sr content increases, the oxygen content also increases up to $\delta = 1$ in $GdSrCo_2O_6$.[88] In the case of $LnBa_{1-x}Sr_xCoCuO_{5+\delta}$, however, increasing the oxygen content is difficult due to the replacement of higher-valent $Co^{3+/4+}$ ions with a lower-valent $Cu^{2+/3+}$ ions. Given the relative instabilities of Co^{4+} and Cu^{3+} compared to Co^{3+} and Cu^{2+}, respectively, it is hard to achieve the maximum lattice oxygen content of $\delta = 1$ in the $LnBa_{1-x}Sr_xCoCuO_{5+\delta}$ system. In order to achieve a value of $\delta = 1$, the oxidation state of the ions must be $Ln^{3+}(Ba,Sr)^{2+}Co^{4+}B^{3+}(O^{2-})_6$ (B = Co or Cu). In the case of $Gd^{3+}Ba^{2+}Co^{4+}Co^{3+}(O^{2-})_6$, only half of the B-site ions are in an unstable oxidation state, while in $Ln^{3+}(Ba,Sr)^{2+}Co^{4+}Cu^{3+}(O^{2-})_6$, all of the B-site ions would be in an unstable oxidation state. This suggests that the room-temperature oxygen content values in the $LnBa_{1-x}Sr_xCoCuO_{5+\delta}$ system are near saturation, limiting the increase in oxygen content that was expected with increasing Sr content.

`

From the previous work, it is known that $LnBaCoCuO_{5+\delta}$ (Ln = Nd and Gd) is chemically compatible with the LSGM electrolyte, but undergoes side reactions with GDC.[79] To determine the stability of $LnBa_{1-x}Sr_xCoCuO_{5+\delta}$ with LSGM, a 50 : 50 wt. % mixture was prepared and heated at 950 ^oC for 12 h and examined by XRD. The XRD data indicated no side reactions (data not shown). Therefore, LSGM electrolyte was deemed suitable for use in the electrochemical tests.

6.3.2 Thermal and Electrical Properties

For clarity, three points will be defined along the TGA curves. Figure 6.4 shows the TGA curve of $NdBa_{0.75}Sr_{0.25}CoCuO_{5+\delta}$ as an example, with these three points labeled as "furnace-cooled," "TGA-900," and "TGA-cooled." Furnace-cooled is the oxygen content value obtained from iodometric titration directly after annealing, TGA-900 is the oxygen content value taken from the TGA curve at 900 ^oC, and TGA-cooled is the oxygen content value taken from the TGA curve at room temperature after being cooled from 900 ^oC. Figure 6.5 shows the TGA heating curves of the $LnBa_{1-x}Sr_xCoCuO_{5+\delta}$ (Ln = Nd and Gd) samples, recorded in air. All samples start to lose oxygen at around 300 ^oC, but at varying rates. As these samples were annealed at 900 ^oC for 12 h and cooled at a very slow rate of 0.5 ^oC min^{-1} prior to measurement, their oxygen content was expected to be at a maximum. This discrepancy may be due to the difference between the stationary atmosphere in the furnace and the dynamic, flowing atmosphere of the TGA. For ease of reference, the oxygen contents of all compounds at furnace-cooled room

`

temperature, TGA-900, and TGA-cooled room temperature can be found in Table 6.2. With Ln = Nd, both the x = 0.25 and x = 0.75 samples exhibit significant differences between the furnace-cooled and TGA-cooled oxygen contents, while the x = 0 and x = 0.5 samples show a much smaller difference. The differences between the furnace-cooled and TGA-cooled oxygen contents are negligible for the Ln = Gd samples as well.

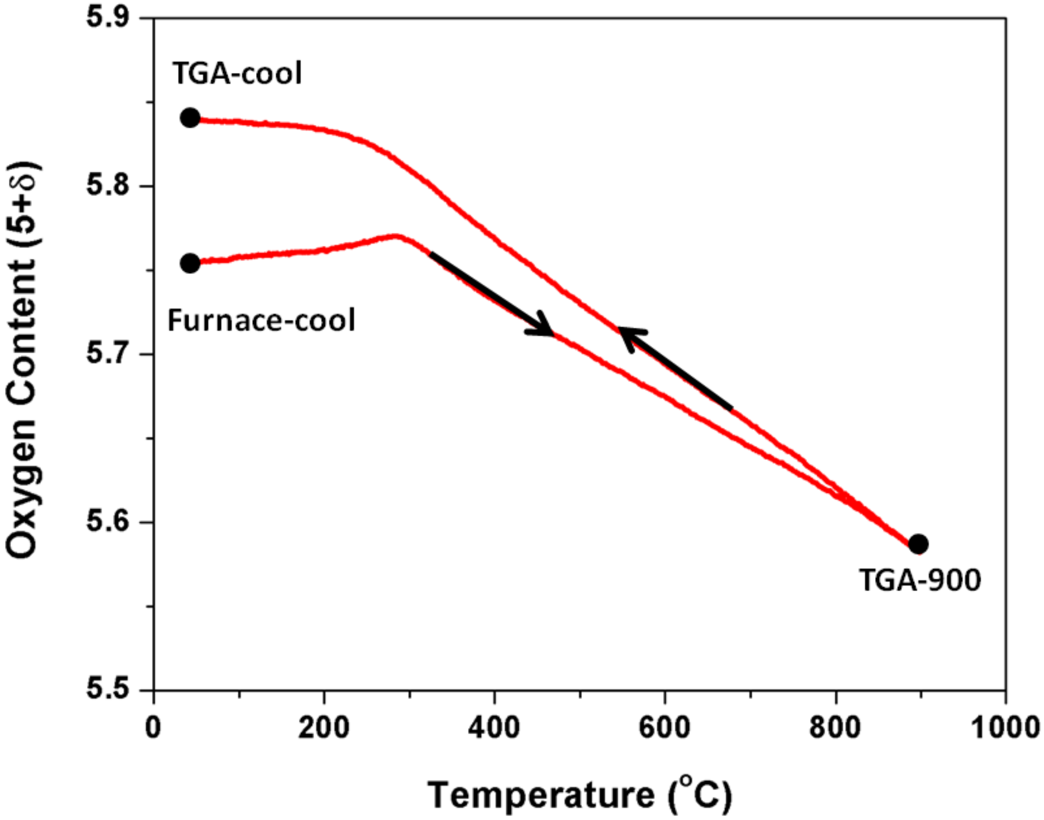

Figure 6.4 TGA plot of $NdBa_{0.75}Sr_{0.25}CoCuO_{5+\delta}$, illustrating the variations in oxygen content during heating and cooling.

`

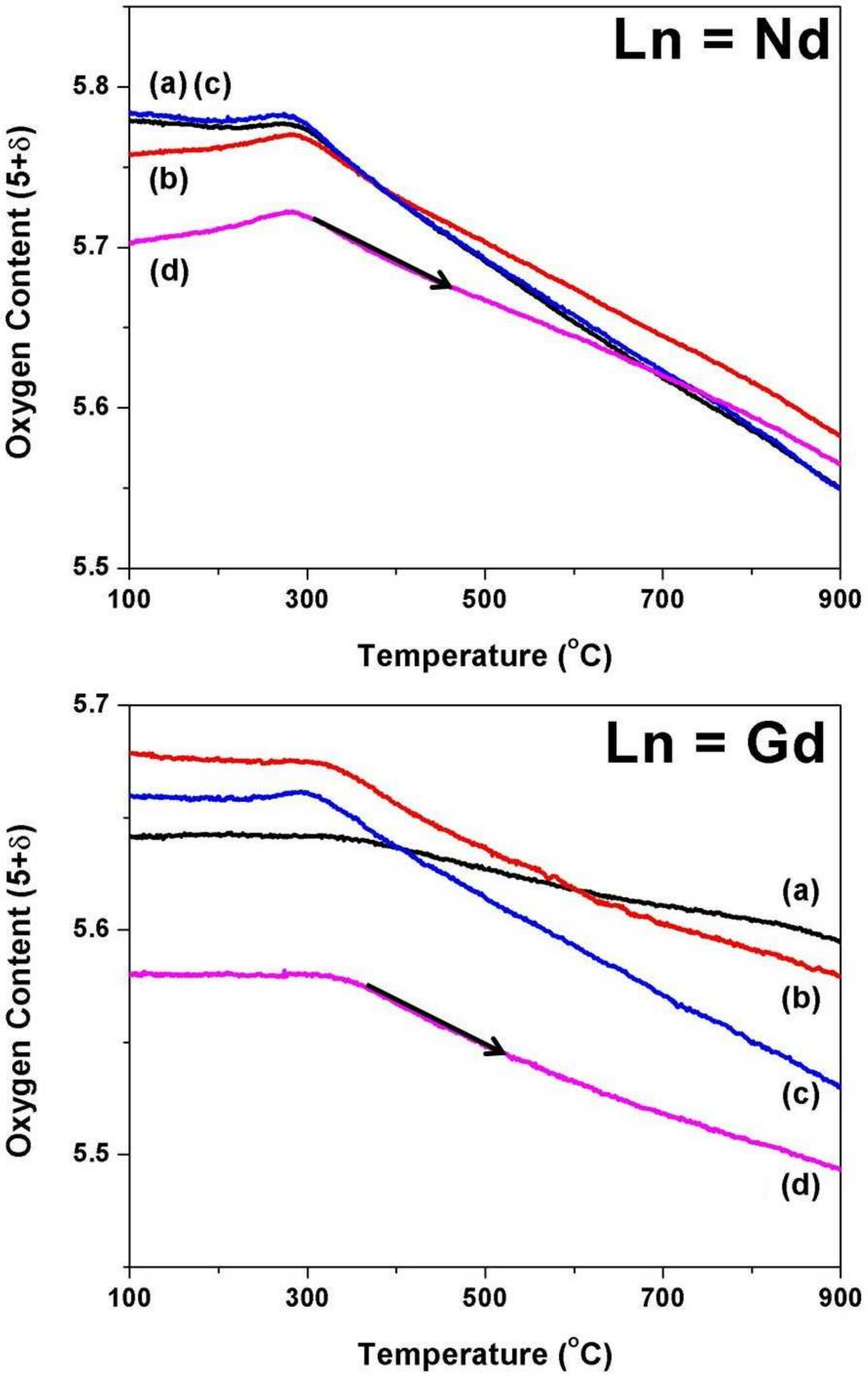

Figure 6.5 Variations in the oxygen content with temperature of the $LnBa_{1-x}Sr_xCoCuO_{5+\delta}$ samples in air: (a) x = 0.0, (b) x = 0.25, (c) x = 0.50, and (d) x = 0.75. Measurements were taken during heating of the samples.

`

Table 6.2 Variations in oxygen content values as measured by titration and TGA of $LnBa_{1-x}Sr_xCoCuO_{5+\delta}$ (Ln = Nd and Gd)

		Oxygen Content (5+δ)		
Ln	x	Furnace-cooled	TGA-900	TGA-cooled
Nd	0.00	5.782	5.550	5.770
	0.25	5.753	5.583	5.840
	0.50	5.789	5.549	5.769
	0.75	5.694	5.565	5.797
Gd	0.00	5.643	5.594	5.655
	0.25	5.681	5.579	5.678
	0.50	5.662	5.530	5.680
	0.75	5.581	5.493	5.592

The thermal expansion curves of $LnBa_{1-x}Sr_xCoCuO_{5+\delta}$ (Ln = Nd and Gd) in air are shown in Figure 6.6 and the TEC values are given in Table 6.3. All samples show an increase in expansion rate around 300 °C, which can be attributed to the loss of oxygen from the lattice and the reduction of $(Co,Cu)^{n+}$.[93] For the Ln = Nd samples, the x = 0.25 and x = 0.5 samples show a significant increase in thermal expansion compared to the x = 0 and x = 0.75 samples. This change occurs mostly after 300 °C; at temperatures below 300 °C, the TEC is similar amongst all the samples. This suggests that the loss of oxygen in the x = 0.25 and x = 0.5 samples has a greater effect on TEC than in the other samples.

This may be due to the degree of oxygen loss (Table 6.2), as x = 0.25 shows a large difference between TGA-900 and TGA-cooled oxygen content values, and x = 0.5 shows a large difference between initial furnace-cooled and TGA-900 oxygen content values. In the Ln = Gd samples, however, the substitution of Sr for Ba was found to have less of an effect on thermal expansion. This may be due to the fact that the Gd samples have smaller changes in oxygen content upon heating and cooling, due to the increased covalency of the Gd-O bond compared to the Nd-O bond, and that the oxygen vacancies in layered perovskites are predominantly located in the LnO layer.[108]

`

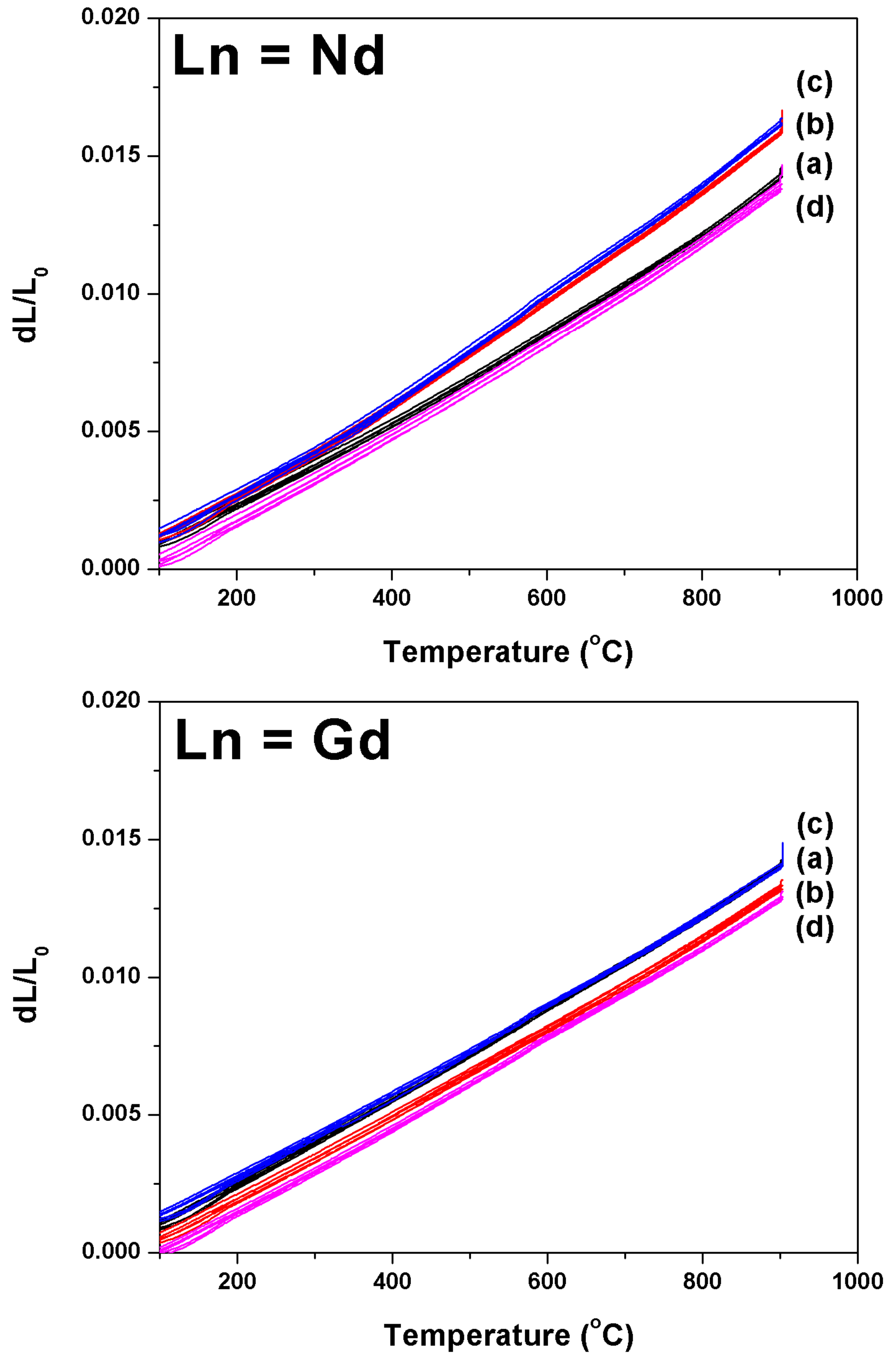

Figure 6.6 Thermal expansion (*dL/L$_0$*) curves in air of the $LnBa_{1-x}Sr_xCoCuO_{5+\delta}$ samples: (a) x = 0.0, (b) x = 0.25, (c) x = 0.50, and (d) x = 0.75. L_0 is the initial length of the sample pellet.

`

Table 6.3 Maximum power density, TEC, and electrical conductivity of selected cathode materials

Chemical Composition	Maximum Power Density ($mW\ cm^{-2}$)*	TEC (80 – 900 ^{o}C) ($10^{-6}\ K^{-1}$)**	Electrical Conductivity ($S\ cm^{-1}$)*
$GdBaCoCuO_{5+\delta}$	468	16.3	90.239
$GdBa_{0.25}Sr_{0.75}CoCuO_{5+\delta}$	530	16.0	46.727
$NdBa_{0.25}Sr_{0.75}CoCuO_{5+\delta}$	562	17.0	170.523

* Maximum power density and electrical conductivity values taken at 800 °C

** TEC values measured from 80 to 900 °C

The variations of the electrical conductivities of $LnBa_{1-x}Sr_xCoCuO_{5+\delta}$ (Ln = Nd and Gd) as a function of temperature are shown in Figure 6.7. In both series, a change in conductivity behavior can be observed above 300 ^{o}C. The decrease in conductivity (in the Ln = Nd system in Figure 6.7a) or the slowdown in the increase in conductivity (in the Ln = Gd system in Figure 6.7b) above 300 ^{o}C can be attributed to the increase in oxygen vacancies, disturbing the O-Co-O conductance pathway.[88] In the Ln = Nd series, the conductivity value at a given temperature increases with x first for $0 \leq x \leq 0.5$ and then decreases for x = 0.75. The increasing conductivity could be due to reduced lattice distortion, as the lattice distortion (*c/2a*) values shown in Table 6.1 follow the same pattern. Previous work has shown that higher lattice distortion (*i.e.*, further from the ideal value of unity) has a significant effect on electrochemical performance.[109] The decrease in conductivity on going from x = 0.5 to 0.75 could be due to the larger concentration of oxygen vacancies. The Ln = Gd series shows a similar trend in conductivity values with x

`

as the Ln = Nd series in the $0.25 \leq x \leq 0.75$ region, but the conductivity values show a slowdown in the increase above 300 °C instead of a decrease as found in the Ln= Nd system. This is due to a much smaller change in oxygen content with temperature in the Ln = Gd system compared to the Ln = Nd system in Figure 6.5. Also, the x = 0 sample in the Ln = Gd system shows a continuous increase in conductivity with temperature unlike the Ln = Nd analog due to the much smaller decrease in oxygen content with temperature (Figure 6.5). The electrical conductivity values for these samples are smaller compared to those of other layered perovskite systems, but the values are similar to those seen in the $LnBaCo_{2-x}Cu_xO_{5+\delta}$ (Ln = Nd, Gd) system, since the substitution of copper for cobalt is known to reduce electronic conductivity.[79] The higher conductivities of the Ln = Nd system compared to the Ln = Gd system is due to both the lower concentration of oxygen vacancies and the decreased lattice distortion in the Ln = Nd system.[62]

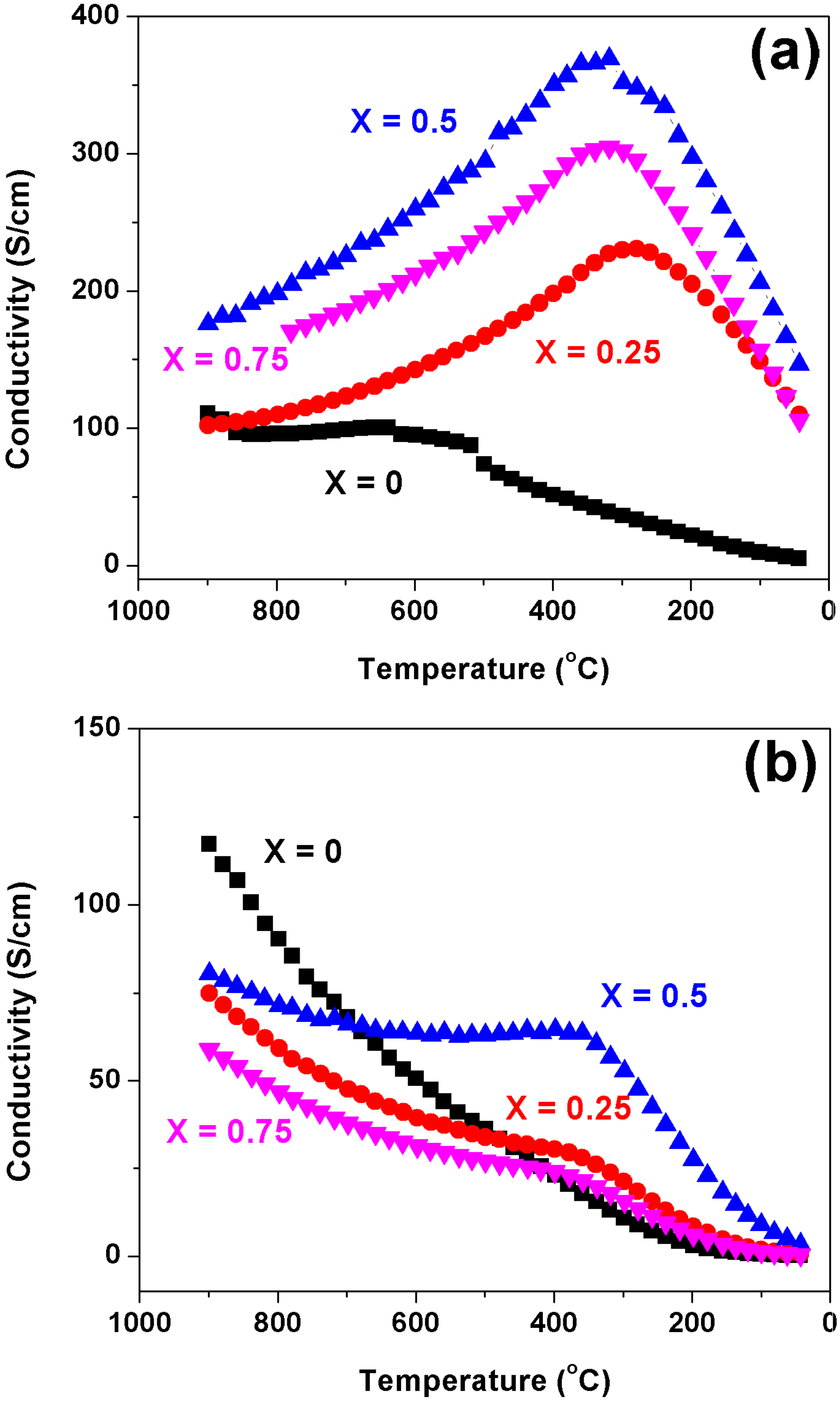

Figure 6.7 Variations of the electrical conductivity with temperature of (a) $NdBa_{1-x}Sr_xCoCuO_{5+\delta}$ and (b) $GdBa_{1-x}Sr_xCoCuO_{5+\delta}$ in air, measured with a 4 probe Van der Pauw setup.

`

6.3.3 Electrochemical Properties

The electrochemical performances of the $LnBa_{1-x}Sr_xCoCuO_{5+\delta}$ (Ln = Nd and Gd) samples were evaluated by ac-impedance spectroscopy in air with cathode | cathode + LSGM (50 : 50 wt%) | LSGM | cathode + LSGM (50 : 50 wt%) | cathode symmetric cells with 0.5 mm thick electrolyte. Composites were used to ensure good contact during heating cycles, as in previous work.[62,79,88] The variations of ionic conductance with temperature are shown in Figure 6.8. It is seen that the Ln = Nd system has higher conductance than the Ln = Gd system, which is expected based on previous work that showed a decrease in the size of the Ln^{3+} ions is accompanied by a decrease in the performance due to reduced bulk oxygen diffusion and surface exchange rates.[62] In both the Ln = Nd and Gd samples, there exists a trend of decreasing conductance with x in the $0 \leq x \leq 0.5$ region, followed by an increase in conductance at x = 0.75. This could be explained by the variations in the lattice volume, cation ordering, and oxygen content. Previous work has shown that a decrease in the free lattice volume (volume of the lattice not occupied by its constituent ions) of perovskites can slow down oxygen transport due to a constriction of its transportation pathway, which can explain the decrease in conductance in the $0 \leq x \leq 0.5$ region.[110-113] It has also been shown that an increase in Sr substitution results in an increase in cationic disorder between Ln^{3+} and $(Ba_{1-x}Sr_x)^{2+}$ due to the smaller size difference between Ln^{3+} and Sr^{2+}, which in turn results in increased oxygen diffusivity.[88,109,110] Furthermore, the x = 0.75 sample has a higher concentration of oxygen vacancies. Thus, the increase in cell volume and number of oxygen vacancies

(Table 6.1) along with higher oxygen diffusivity all lead to a higher conductance for the x = 0.75 samples.

`

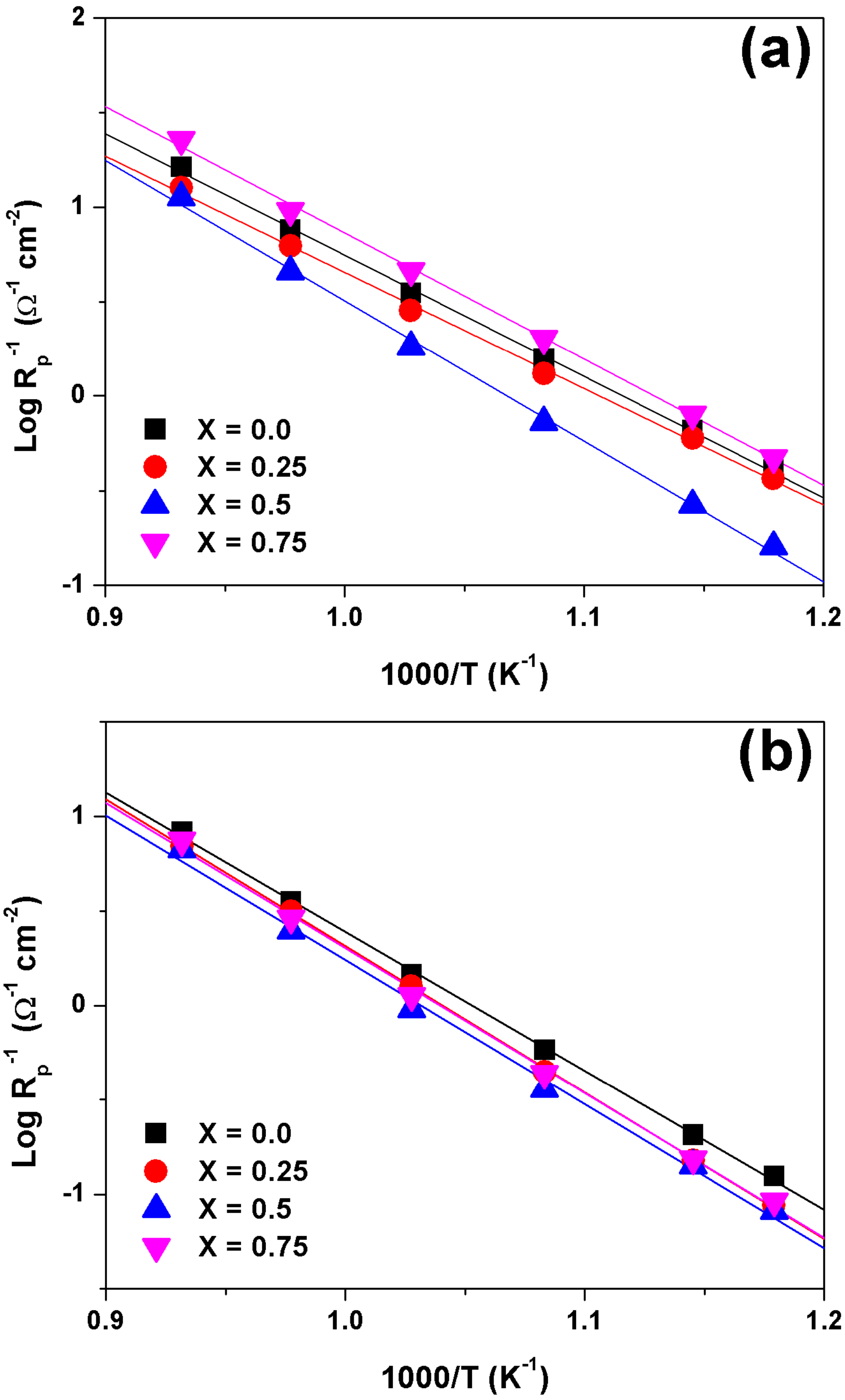

Figure 6.8 Variations of the conductance (R_p^{-1}) with temperature of the (a) $NdBa_{1-x}Sr_xCoCuO_{5+\delta}$ and (b) $GdBa_{1-x}Sr_xCoCuO_{5+\delta}$ cathodes with temperature in air, as measured with an LSGM-supported symmetrical cell by ac-impedance spectroscopy.

`

Based on ac impedance spectroscopy data, three single cells were fabricated. These single cells consisted of a cathode |cathode + LSGM | LSGM | LDC | GDC + NiO configuration, with the LDC acting as a buffer layer between LSGM and the GDC + NiO anode to prevent side reactions.[62] The $GdBaCoCuO_{5+\delta}$, $GdBa_{0.25}Sr_{0.75}CoCuO_{5+\delta}$, and $NdBa_{0.25}Sr_{0.75}CoCuO_{5+\delta}$ samples were used as cathodes for three single cells and were tested as described in the experimental section. Figure 6.9 shows the polarization and power density curves of these three samples. All samples showed open circuit voltages close to the theoretical value of 1.10 V.[88] The non-substituted $GdBaCoCuO_{5+\delta}$ shows the worst performance, with a maximum power density of 468 mW cm^{-2} at 800 ^{o}C. This power density value is lower than that reported by Kim *et al*, which could be due to the differences in the cathode microstructure and porosity, arising from a different synthesis procedure and difference in electrolyte thickness (Figure 6.10).[79] The $GdBa0_{.25}Sr_{0.75}CoCuO_{5+\delta}$ sample shows a maximum power density at 800 ^{o}C of 530 mW cm^{-2}, which is a ~ 15% increase compared to the x = 0 sample although both the x = 0 and 0.75 samples show similar polarization conductance values at the SOFC operating temperatures of 700 – 800 ^{o}C in Figure 6.8b. The discrepancy between the single cell and symmetric cell measurements may be related to the experimental variations in the fabrication process as well as the effects of the anode in the single cell. The impedance values were taken along the heating curve, while the single cell measurements were taken along the cooling curve after a 3 h dwell time at 800 ^{o}C. The electrochemical performance of the $NdBa_{0.25}Sr_{0.75}CoCuO_{5+\delta}$ samples correlated well to the ac impedance measurements. $NdBa_{0.25}Sr_{0.75}CoCuO_{5+\delta,}$ which showed the highest conductance

`

measured by ac impedance, also showed the highest maximum power density of 562 mW cm^{-2}, a 6% increase over $GdBa_{0.25}Sr_{0.75}CoCuO_{5+\delta}$.

Table 6.3 compares the key performance data of the samples obtained with the single cell measurements. The increase in electrochemical performances of the x = 0.75 samples, while maintaining similar thermal expansion coefficients, suggests that the $LnBa_{0.25}Sr_{0.75}CoCuO_{5+\delta}$ (Ln = Nd and Gd) samples are attractive candidates for use as cathodes in IT-SOFC systems.

`

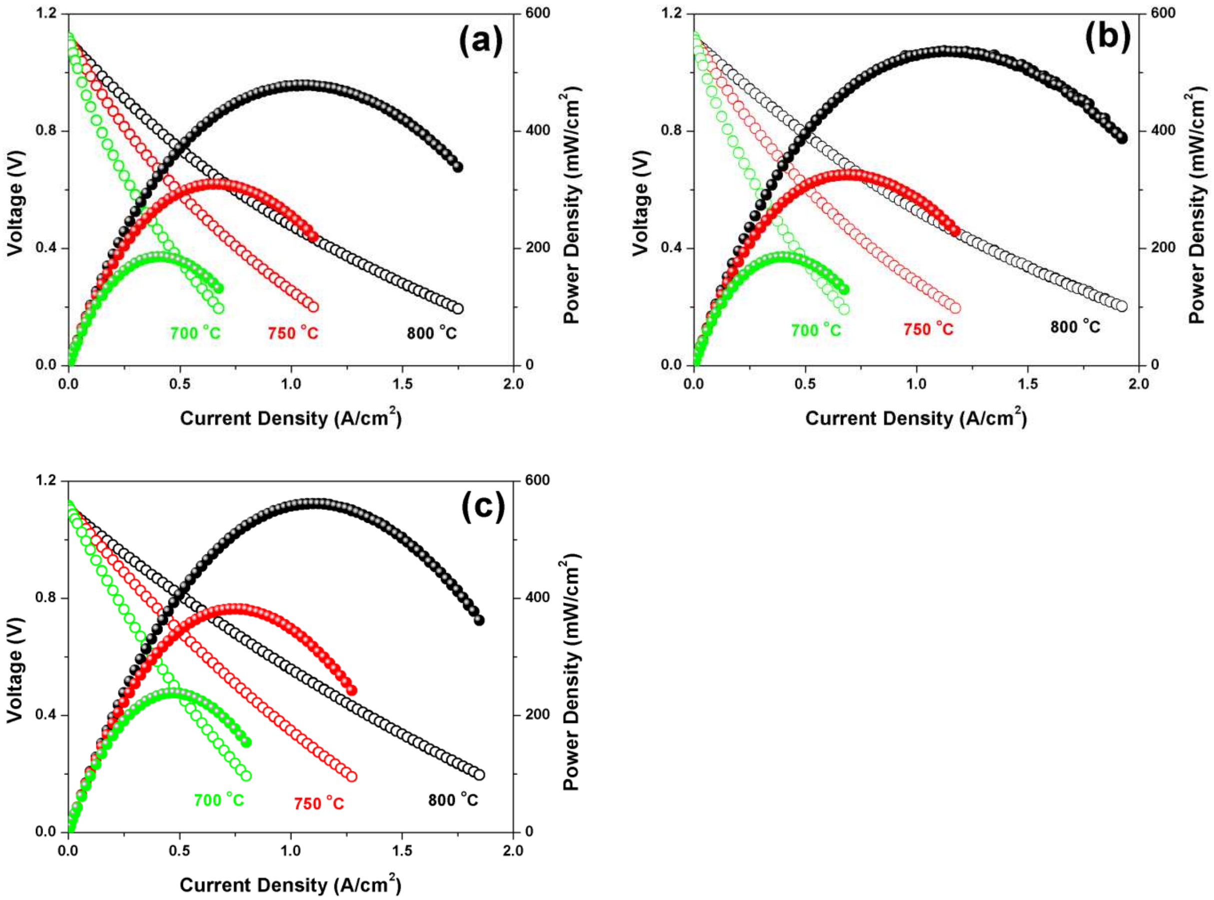

Figure 6.9 Comparison of the electrochemical performance data of (a) GdBaCoCuO$_{5+\delta}$, (b) GdBa$_{0.25}$Sr$_{0.75}$CoCuO$_{5+\delta}$, and (c) NdBa$_{0.25}$Sr$_{0.75}$CoCuO$_{5+\delta}$ cathodes in the range of 700 – 800 °C with an electrolyte-supported single cell.

`

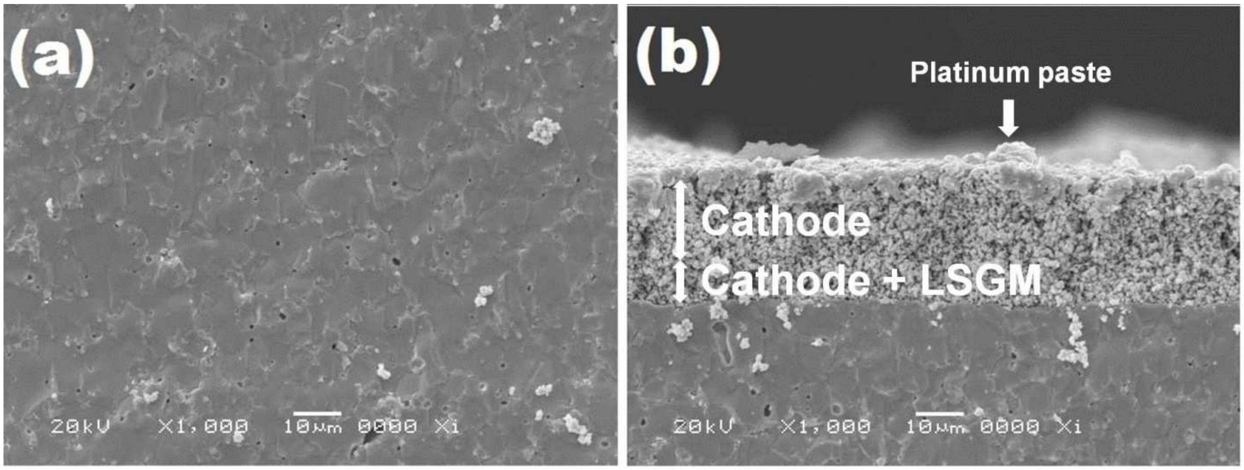

Figure 6.10 SEM micrographs showing the cross sections of the (a) LSGM dense electrolyte and (b) cathode | cathode + LSGM | LSGM portion of the $GdBaCoCuO_{5+\delta}$ single cells. Images were taken after the measurement of single cell performance. Cathode particles in the dense electrolyte region in both images are due to fracturing of the cell after measurement.

6.4. CONCLUSIONS

The effect of Sr substitution in the $LnBa_{1-x}Sr_xCoCuO_{5+\delta}$ $0 \leq x \leq 0.75$) system has been investigated. All samples could be refined based on a *P4/mmm* tetragonal space group without any change in symmetry with Sr content unlike the analogous $LnBa_{1-x}Sr_xCo_2O_{5+\delta}$ system, indicating that the B-site substitution has a dominant influence on the crystal structure. The oxygen content determined by iodometric titration and TGA measurements showed that the Ln = Nd samples lose more oxygen upon heating than the Ln = Gd samples. Electrical conductivity was lowered by the substitution of Cu for Co, which correlated with the lattice distortion values. Electrochemical measurements

`

showed that the $LnBa_{0.25}Sr_{0.75}CoCuO_{5+\delta}$ (Ln = Nd and Gd) samples exhibit a significant improvement over the x = 0 samples in SOFC. As the x = 0.75 samples show higher electrochemical performance over the x = 0 samples without increasing the thermal expansion, the $LnBa_{0.25}Sr_{0.75}CoCuO_{5+\delta}$ (Ln = Nd and Gd) perovskites prove to be promising candidates for IT-SOFC cathodes.

`

CHAPTER 7

Synthesis of 3-Dimensional Silver Networks and their Application for Solid Oxide Fuel Cells

7.1 INTRODUCTION

Precious metals have long been used in the stack assembly of various fuel cells. Low-temperature fuel cells, such as the polymer electrolyte membrane fuel cells (PEMFC), traditionally operate with precious metals like platinum as catalysts for the electrochemical reactions.[3,114-121] Solid oxide fuel cells (SOFCs), however, are attractive in that they do not need precious metal catalysts to achieve high fuel to electricity efficiencies.[4,15,16] However, precious metals are still widely used in SOFC stack assemblies as current collecting materials, as they offer excellent electrical conductivity and low reactivity with traditional SOFC materials.

SOFCs traditionally operate at very high temperatures (800 - 1000°C) to overcome the low catalytic activity at low temperatures. Besides the ability to utilize less expensive, non-precious metal electrocatalysts (*e.g.* Ni and Co), it also allows for the utilization of a wide variety of fuels and offers the ability to improve their efficiencies further by operating in a combined heat and power (CHP) setup.[4,15,16] Unfortunately, these high temperatures require specialized materials to avoid problematic side reactions, deter materials decomposition, and alleviate thermal expansion mismatch between the various stack components.[122,123] As these specialized materials can be expensive, there has been significant interest in reducing SOFC operating temperatures; this has

`

necessitated the development of new functional materials as traditional electrodes do not have adequate performance at these reduced temperatures.[124,125]

Due to these high operating temperatures, the precious metal of choice for SOFCs was generally platinum, with a melting temperature (T_m) at atmospheric pressure of 1768 °C.[95] With the advent of intermediate temperature (600 – 800 °C) SOFC (IT-SOFC) electrodes, however, the use of silver (T_m = 962 °C) and gold (T_m = 1064 °C) has become possible.[29,37,59,61,62,88,90,95,107] At the time of writing this chapter, the commodities price of silver (~ 0.6 USD g^{-1}) is significantly less than that of gold (~41 USD g^{-1}) and platinum (~46 USD g^{-1}), making it a desirable replacement.[126]

Due to its high electrical conductivity and favorable oxygen reduction reaction catalytic activity, platinum has widely been studied as an electrode and current collector in solid oxide fuel cells. Recent work has also focused on the possibility of silver to be used similarly, with good success.[96-98] Many of these electrodes and current collectors are, however, manufactured with labor- or energy-intensive patterning processes to achieve the desired microstructure.[98] In our previous work, we utilized silver current collectors in the form of a micron-grade mesh[29], which were manufactured by a single-step procedure of screen-printing commercially available silver paste that had been diluted with commercially available dispersant. The results showed that functional silver network can be easily manufactured, and that it may be possible to form a 3-dimensional structure of silver similarly.

`

In this Chapter, we present a facile synthesis of a 3-dimensional silver network by screen printing and heat treating Ag_2O particles. The effects of synthesis procedures on microstructure, stability of the Ag materials under SOFC operating environments, and their electrochemical performance as cathodes for ORR in SOFC are presented.

7.2 EXPERIMENTAL METHODS

The Ag_2O nanoparticles were synthesized by a precipitation reaction. $AgNO_3$ was dissolved in deionized (DI) water under agitation on a stir plate and diethylamine ($CH_3Ch_2NHCH_2CH_3$) was then added dropwise to precipitate Ag_2O.[127,128] The addition of diethylamine was continued until precipitation was no longer visually observed. The resultant heterogeneous mixture was then filtered through a vacuum flask with a nylon filter. The powder was washed with deionized water for 1 h to ensure removal of the diethylamine. The resultant powder were then dried overnight at ~ 60 °C, and characterized by x-ray diffraction (XRD) with Cu K_α radiation.

The dried Ag_2O powder was then mixed with an organic binder (Heraeus V006) in a 50 : 50 mass ratio to form inks for screen printing. These inks were then screen printed three times on an 8 mol% yttria stabilized zirconia (8YSZ) substrate of 150 – 200 μm thickness and heat treated for 2 h at various temperatures in the range of 450 – 900 °C. These structures were then characterized using a JEOL JSM-5610 scanning electron microscope (SEM).

`

Electrochemical cells were manufactured by screen-printing the ink three times on both sides of the 8YSZ substrates to make symmetric cells. Two cells were manufactured; one was sintered at 600 °C for 2 h, and the other was sintered at 800 °C for 2 h. For a comparison, cells with commercially purchased Ag (FuelCellMaterials Ag-I) and Pt pastes (FuelCellMaterials Pt-I) were manufactured by screen printing one layer of paste on 8YSZ substrates. One Ag cell was sintered at 800 °C for 1 h. Two Pt cells were manufactured; one sintered at 800 °C for 1 h and the other sintered at 1500 °C for 1 h to observe the effect of sintering temperature on performance. The polarization resistances (R_ps) of all samples were observed by a Solartron 1260 FRA impedance analyzer in the range of 400 – 800 °C. All electrodes were manufactured with a screen-printed area of 0.25 cm^2.

The stability of silver as a SOFC current collector was also investigated. Ag current collectors were manufactured as the micron-scale mesh similar to that in our previous work for both the anode and cathode side of a SOFC single cell.[29] The utilized cathode was $YBaCo_3ZnO_{7+\delta}$ + GDC and the anode was Ni-GDC. The fuel cell was attached to an alumina tube SOFC single cell station and sealed with Kimax glass, which was heated at 800 °C for 3 h for sealing. After sealing, the SOFC station was operated with H_2 for the fuel and air as the oxidant at 100 cm^3 min^{-1} for both gases. After exposure to the atmospheres, the Ag current collectors were observed by SEM.

Silver disks were manufactured by pressing Ag_2O powder into pellets and sintering at 900 °C, followed by a slow 1 °C min^{-1} cooling rate to anneal the disks. These

`

disks were then exposed to various atmospheres before being observed by SEM. One disk was heated in 10% H_2 – 90 % Ar atmosphere, allowed to dwell at room temperature under gas flow for 20 min, heated at 4 °C min^{-1} to 900 °C, and allowed to dwell for 2 h before cooling to room temperature at the same rate. The other disk was heated in nitrogen atmosphere to 900 °C at a rate of 4 °C min^{-1} and allowed to dwell at 900 °C for 2 h before the atmosphere was changed to a 10% H_2 – 90 % Ar. This pellet was allowed to dwell in this atmosphere for another 2 h before being reverted back to N_2 and cooled to room temperature at the same rate. These pellets were then examined by SEM to assess the effect on the microstructure.

7.3 RESULTS AND DISCUSSION

7.3.1 Materials Processing and Effect on Microstructure

The XRD pattern of Ag_2O is shown in Figure 7.1. The pattern fits well with published data on Ag_2O, although there is an observable impurity phase that was successfully indexed as *Fm-3m* metallic Ag. It is possible that some of this metallic contaminant can be sourced to the overnight 60 °C drying process. Ag_2O is well known to decompose into Ag metal at temperatures above 300 °C in air, which made this an excellent synthesis reagent for our process.[129-131]

`

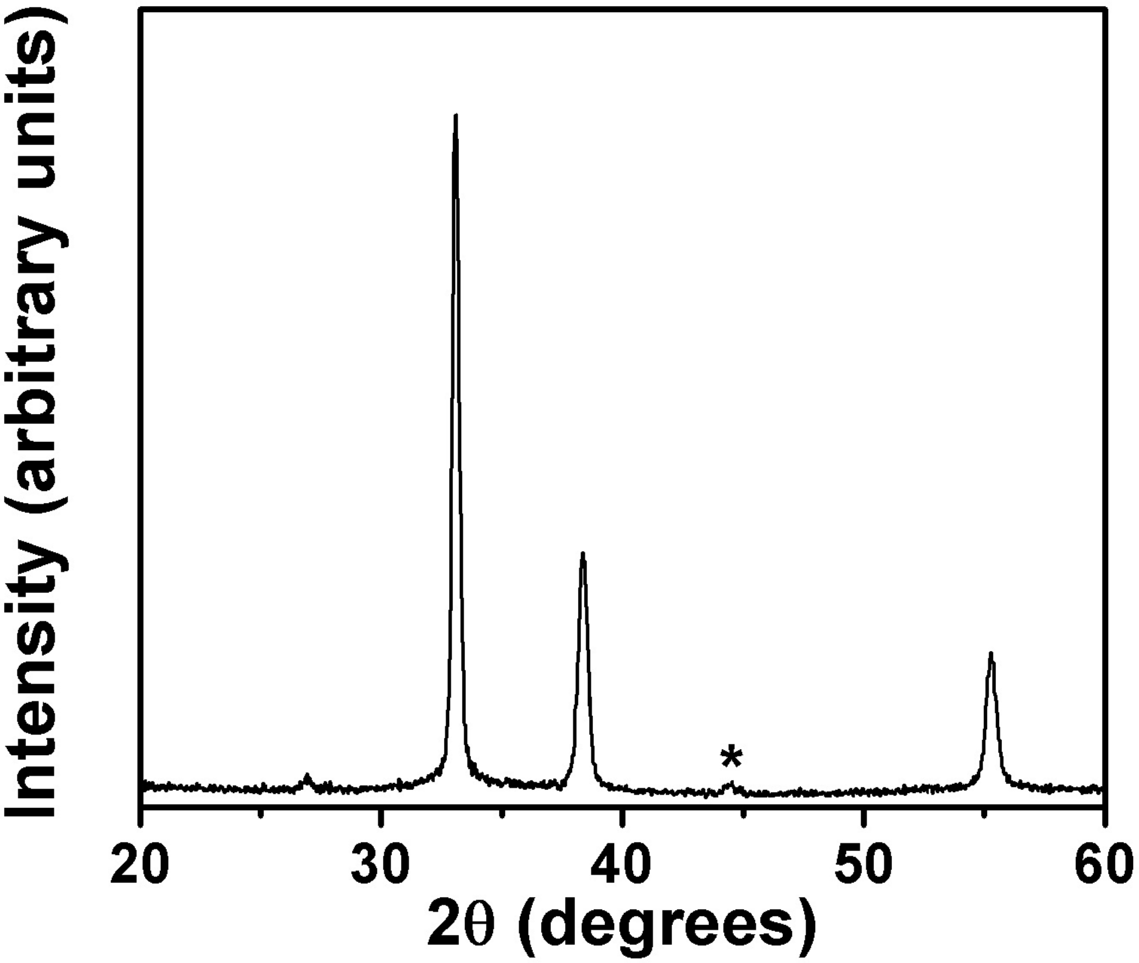

Figure 7.1 XRD data of the as-synthesized Ag_2O powders after washing with de-ionized water and drying overnight. The peaks marked with an * refer to trace amounts of Ag metal contaminants from the drying process.

An ink was manufactured using this Ag_2O nanopowder in a 50 : 50 Ag_2O : binder weight ratio, which was then screen printed three times onto 8YSZ electrolyte substrates. These samples were then sintered for 2 h at temperatures ranging from 450 – 900 °C to observe the effect of sintering temperature on microstructure. The SEM micrograph recorded after sintering is shown in Figure 7.2, which shows that the synthesis process successfully created a three-dimensional network of Ag particles supported by the substrate. Figure 7.2 also shows that the morphology of the network is highly dependent on the sintering temperature; the 450 °C sintered sample shows significantly smaller particles with a greatly increased surface area, while the samples sintered at higher temperatures show an increased coarsening of particles and an overall reduction in surface area. This can be understood by the relatively low T_m of Ag (962 °C), along with the relatively small particle size of the oxide prior to sintering.[95,132,133] Figure 7.3 shows the cross-sectional SEM micrographs of the 600 and 900 °C cells as further reference. As can be seen in Figure 7.3, the 600 °C sample maintains good porosity, while the 900 °C sample has formed a dense layer of Ag. Both Figures 7.2 and 7.3 show that the microstructure of these materials can be easily tailored through altering their processing temperatures, which can be useful in designing functional materials.

`

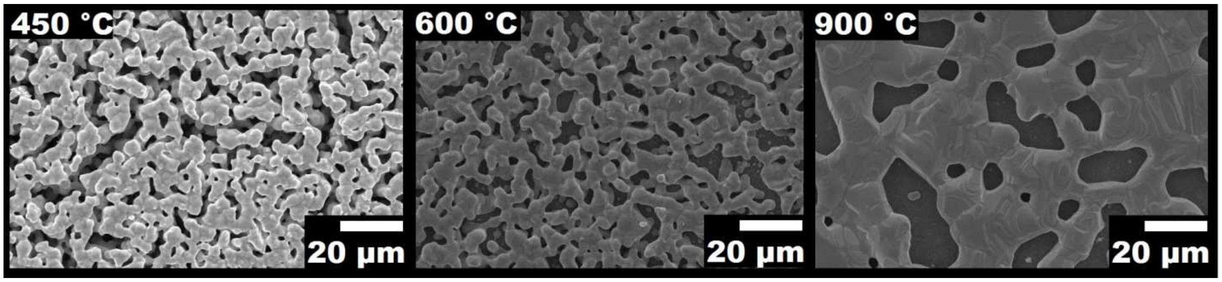

Figure 7.2 SEM micrographs of as-synthesized Ag network. All samples were made from the same ink (50 : 50 weight ratio), but were sintered at different temperatures.

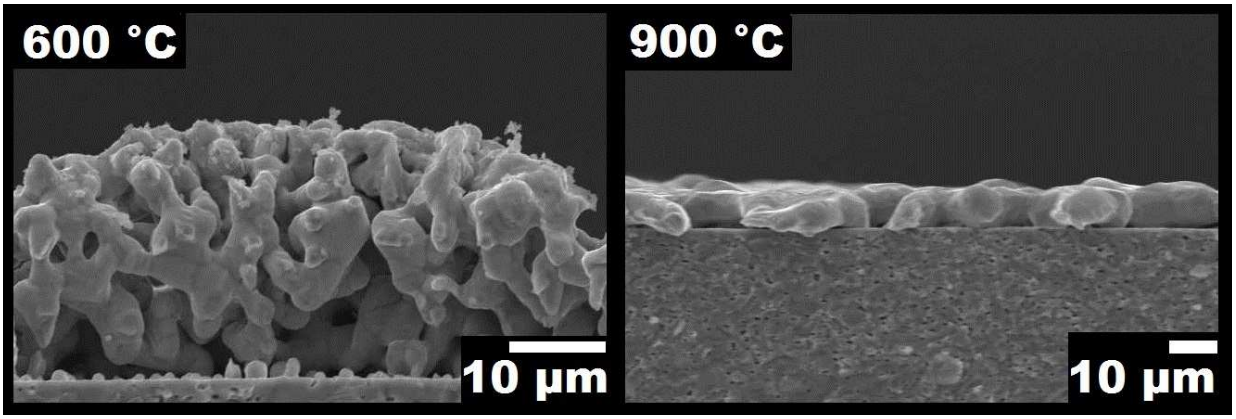

Figure 7.3 Cross-sectional SEM micrographs of the cells shown in Figure 7.2.

7.3.2 Materials Stability in Solid Oxide Fuel Cell Environments

In order to determine the usefulness of these materials in SOFC setups, Ag current collectors, mesh, and leads were applied to both the anode and cathode of an 8YSZ-electrolyte-supported single cell using a traditional Ni-GDC anode and a *swedenborgite*-type $YBaCo_3ZnO_{7+\delta}$-GDC composite cathode and exposed to the operating conditions.

`

The SEM images of the Ag current collector wires after the attempted single cell test are shown in Figure 7.4, in which the cathode-side Ag wire was unaffected, while the anode-side wire underwent significant material degradation in the form of fractures and pitting. These results were then duplicated by exposing the samples to specialized atmosphere; a piece of Ag wire was heated in an ambient air environment at 800 ^{o}C, while another was heated in air to 800 °C before being exposed to a 10% H_2 – 90 % Ar environment; both wires were then examined by SEM. The air-exposed wire was observed to be unaffected, while the H_2 exposed wire showed degradation (results not shown here) similar to the anode side under the SOFC operating conditions in Figure 7.4. Previous work has shown that the source of this degradation is not hydrogen embrittlement that is common to many other metals, but instead is steam embrittlement.[134,135] Ag is a well-documented oxygen storage material, and has been observed to absorb as much as much oxygen as twenty times its volume.[136] The dissolved oxygen has been shown to react with H_2 to form water; at elevated temperatures, this water is in the form of gaseous steam and has been shown to cause pitting and fracturing of the silver along grain boundaries.

`

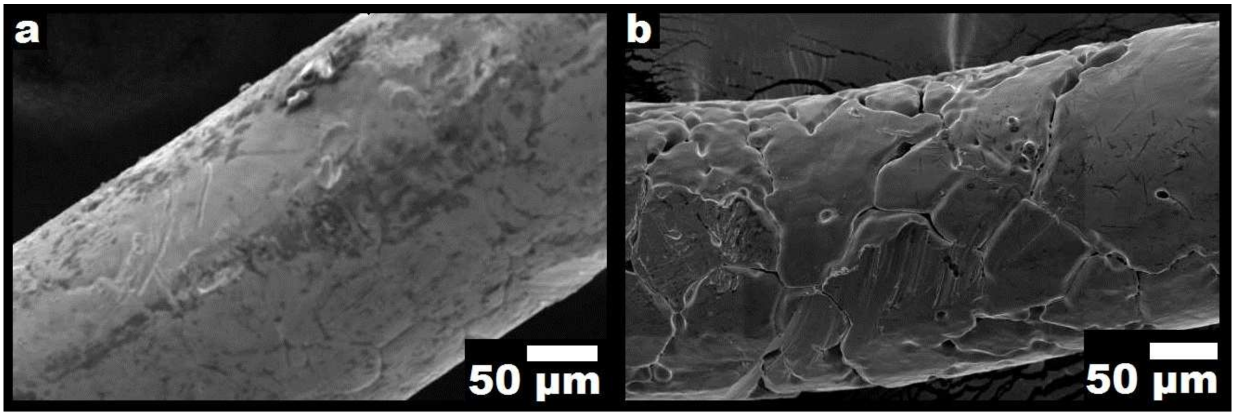

Figure 7.4 SEM micrographs showing the results of the Ag current collector of a SOFC single cell on the (a) air-exposed cathode side and (b) the hydrogen-exposed anode side. The cathode side current collector wire shows no damage, while the anode side wire shows remarkable pitting and grain boundary fractures resulting in total cell failure.

To further observe the steam embrittlement behavior, two Ag disks were sintered and annealed in air at 900 °C before being subjected to various atmospheres as outlined in the experimental section; one disk was subjected to high-temperature (800 ^{o}C) N_2 treatment before being exposed to 10% H_2 – 90 % Ar atmosphere at (800 ^{o}C), while the other was subjected to 10% H_2 – 90 % Ar atmosphere the entire heating cycle, up to 800 °C. As can be seen in Figure 7.5, both samples were found to exhibit almost no microstructural defects; there was no pitting or fracturing observed in either sample, although the sample exposed to high-temperature (800 ^{o}C) N_2 did show some unusual surface growth. In both cases, the lack of pitting and fractures is attributed to the chemical removal of the dissolved oxygen from Ag. The low-temperature (~ 25 ^{o}C) H_2 leaches the dissolved oxygen as water from the lattice, which is removed during the

`

heating process. N_2 heat treatment at high temperatures (800 ^oC) also provides a reducing environment and removes the dissolved oxygen. These results show that while the steam embrittlement of Ag can result in cell failure, it can be overcome through preventative measures, allowing Ag to be utilized as an anode-side material for IT-SOFCs.

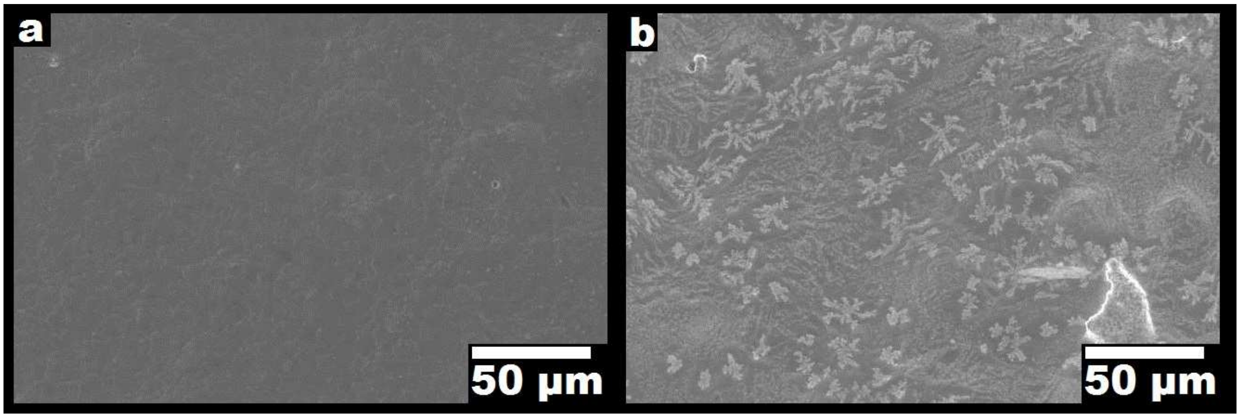

Figure 7.5 SEM micrographs of two Ag disks after heat treatment in different atmospheres: (a) an Ag disk that was exposed to 10% H_2 – 90 % Ar atmosphere at a low temperature (~ 25 ^oC) before being heated to 900 °C and (b) an Ag disk that was exposed to N_2 atmosphere at 900 °C for 2 h before being exposed to 10% H_2 – 90 % Ar.

7.3.3 Electrochemical Performance as a Cathode Material in SOFC

To compare the effect of the microstructure of the Ag on electrochemical performance as a cathode material for ORR in SOFC, various cells were manufactured. Figure 7.6 shows the Nyquist plots of two Ag symmetric cells on commercially available

`

8YSZ electrolyte at 600 °C. Both cells were manufactured by the Ag_2O decomposition method as discussed previously in section 7.2, with one cell sintered at 600 °C and the other at 800 °C. Figure 7.6 shows that the diameter of the impedance arc is significantly reduced in the sample sintered at the higher temperature. When comparing this result to those in Figures 7.2 and 7.3, it can be reasonably concluded that the reason for the drastic difference in microstructure results from the different processing temperatures. As can be seen in Figures 7.2 and 7.3, the lower-temperature sintered sample shows a significantly larger surface area, but the higher-temperature sintered sample shows a significantly larger degree of interconnectivity and greater adhesion to the electrolyte support. As the oxygen reduction reaction in cathode materials is a function of the surface area of the gas-solid interface, the improved performance of the higher-temperature sintered sample suggests that the performance of these Ag cathodes are not limited by their oxygen reduction kinetics. Instead, these results suggest that the performance of these materials is primarily transport limited, which correlates well with previous work on similar materials.[137] In particular, this is supported by the loss of the high-frequency impedance arc that is present in the sample sintered at 600 °C; this arc is generally attributed to the resistance to charge transfer across interfaces, such as grain boundaries or the cathode/electrolyte interface.[58]

`

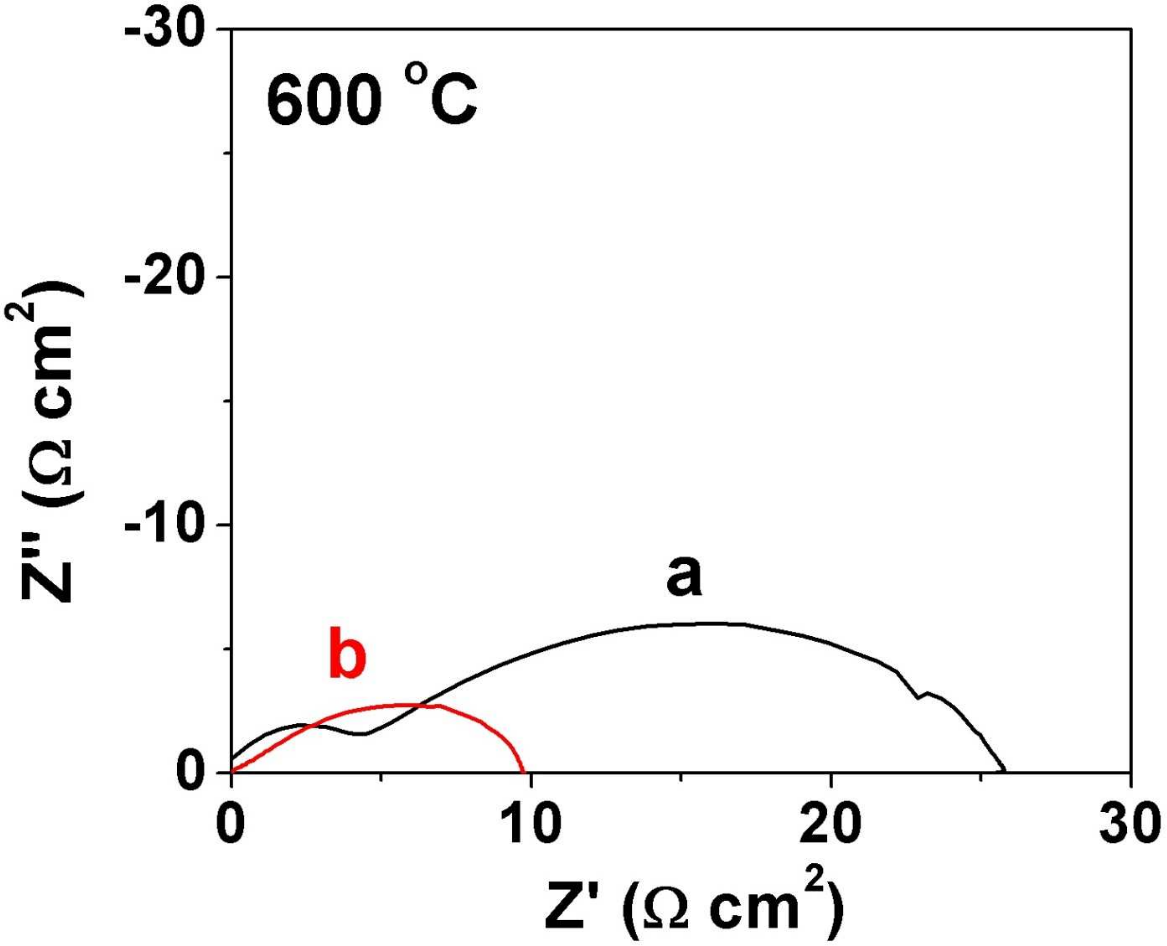

Figure 7.6 Nyquist plots recorded at 600 °C of two electrolyte-supported symmetric cells with an Ag cathode sintered at two different temperatures: (a) impedance spectrum of the symmetric cell sintered at 600 °C and (b) impedance spectrum of the symmetric cell sintered at 800 °C. Both symmetric cells were manufactured with the same starting material.

`

To compare the performance of the Ag cathodes to the traditional Pt electrodes, three symmetric cells were manufactured utilizing commercially available pastes, as described in section 7.2. The Nyquist plots of the AC impedance spectra of all three cells can be seen in Figure 7.7. In Figure 7.7a, it can be readily seen that the 800 °C sintered Ag cell drastically outperforms the Pt cell sintered at the same temperature. As Pt has a significantly higher T_m than Ag, another cell sintered at 1500 °C was manufactured to determine if this result was due to insufficient sintering. The impedance of this cell in comparison to the 800 °C sintered Pt cell can be seen in Figure 7.7b. The data indicates that the impedance of the 1500 °C cell is significantly larger than that of the 800 °C sample. The SEM micrographs of both Pt cells taken after the electrochemical testing can be seen in Figure 7.8. The 1500 °C sample shows a microstructure very similar to the higher-temperature sintered Ag cathode in Figure 7.2, while the 800 °C sample shows a porous structure similar to the lower-temperature sintered Ag samples in Figure 7.2. Interestingly, in the case of Pt, the lower-temperature sintered sample shows a better performance, suggesting that the increased surface area of the porous structure is beneficial. The improved performance of Ag compared to Pt is likely due to the ability for Ag to transport dissolved oxygen through the bulk of the material; this effectively increases the electrochemically active region to the majority of the Ag/8YSZ interface, in contrast to the Pt cathode, which is limited to the three phase boundary (the shared surface area between O_2, Pt, and 8YSZ).[58,73,138] This can also be used to explain why the performance of Ag cathodes in this work decreases with increasing porosity, while the performance of Pt cathodes improves with increased porosity. However, both Pt

`

samples show polarization resistances that are orders of magnitude higher than that of the Ag electrode, showing that Ag materials have great promise for use in IT-SOFCs.

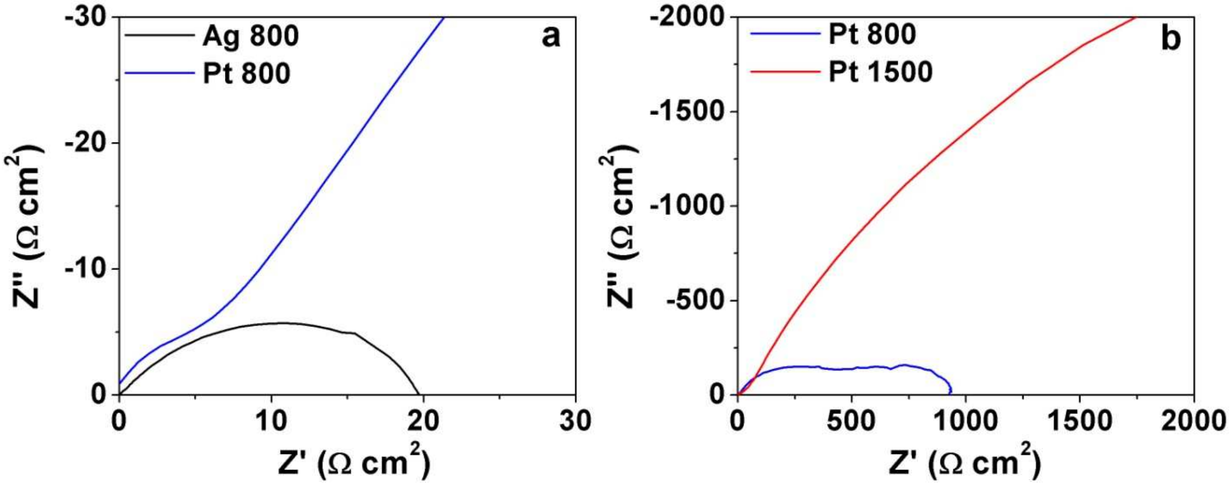

Figure 7.7 Nyquist plots recorded at 600 °C of symmetric cells manufactured from commercially available Ag and Pt pastes: (a) comparison between Ag and Pt inks sintered at 800 °C and (b) comparison between the Pt cell in Figure (a) and another cell sintered at 1500 °C.

`

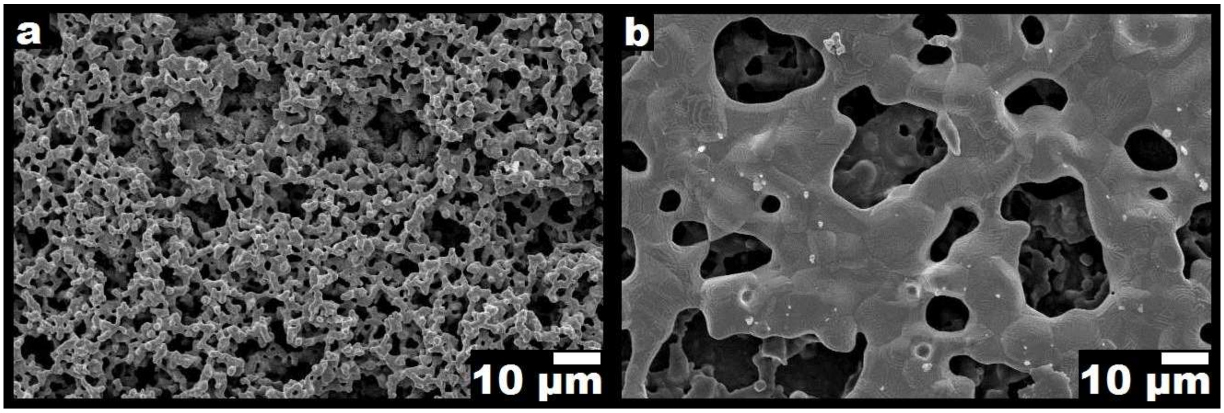

Figure 7.8 SEM micrographs detailing the differences in the microstructures of two cathodes manufactured with commercially available Pt inks: (a) sintered at 800 °C and (b) sintered at 1500 °C. The performance of these cathodes can be seen in Figure 7.7.

7.4 CONCLUSIONS

A facile synthesis procedure for a 3-dimensional silver network from Ag_2O nanoparticles has been developed. The results show that the synthesis temperature greatly impacts the microstructure of the material, with higher sintering temperatures leading to a reduction in surface area and increased coarsening of Ag particles. Initial electrochemical tests showed that the use of Ag as an anode-side current collector was problematic, as steam embrittlement caused significant damage to the current collector. However, work with different gas atmospheres showed that the use of high-temperature (800 ^oC) N_2 and low-temperature (~25 ^oC) H_2 exposure can successfully remove the dissolved oxygen from the Ag, allowing high-temperature H_2 exposure without pitting or grain boundary fractures. Electrochemical impedance spectroscopy tests of symmetric cells on 8YSZ show that Ag greatly outperforms Pt as a cathode material for the oxygen

`

reduction reaction. Further tests with Ag cathodes of various microstructures show that the performance is improved with a larger degree of particle interconnectivity, suggesting that the performance of Ag as a cathode is limited by the rate of oxygen transport in the bulk material instead of the oxygen reduction reaction on the surface. These results show that complex structures of Ag can be successfully manufactured through simple single-step syntheses for use in both anode and cathode SOFC environments, and can be further tailored for desired physical properties as an electrode, current collector, or interconnect material.

`

CHAPTER 8

Summary

With the goal of developing high performance, low thermal-expansion cathode materials for IT-SOFCs, the *swedenborgite*-type $RBaCo_3(Zn,Fe)O_{7+\delta}$ (R = Y, In, and Ca) series of oxides, along with the layered perovskite $LnBa_{1-x}Sr_xCoCuO_{5+\delta}$ (Ln = Nd and Gd) series of oxides, were investigated. The synthesis and utilization of Ag-based materials were also investigated for their capability to be used as IT-SOFC functional materials in place of the more expensive Pt based materials.

The long-term (120 h) thermal stability of the various $RBaM_4O_{7+\delta}$ (R = Y, In, and Ca; M = Co, Zn, and Fe) materials were investigated at 600, 700, and 800 °C. It was observed that the stability of these materials was primarily a function of oxygen content, lattice parameters, and M-site content. In the $Y_{1-x}In_xBaCo_3ZnO_{7+\delta}$ series, it was observed that any In content ≥ 0.1 successfully inhibited the formation of the decompositional $BaCoO_3$ and Co_3O_4 impurity phases. It was determined that this stabilization effect was a function of both lattice volume and oxygen content; at lower In contents, the higher electronegativity of the In^{3+} ion increased room-temperature oxygen contents, and all substitutions of In were found to decrease the reversible oxygen absorption at high temperatures that are known to be related to the decomposition reactions. As the In content increases past x = 0.2 – 0.3, however, the decreasing lattice volume from the substitution of the smaller In^{3+} ion for the larger Y^{3+} ion led to decreased oxygen contents similar to that in $YBaCo_3ZnO_{7+\delta}$; however, the smaller lattice volumes led to steric

`

inhibitions of the decompositional reactions by creating less space for the ions to rearrange themselves into the decompositional products. This stabilization effect of In was also observed in the $Y_{1-x-y}In_xCa_yBaCo_3ZnO_{7+\delta}$ series ($0.2 \leq x + y \leq 0.5$), where all compounds had an In content ≥ 0.1, and all compounds were observed to be stable at all temperatures. Previous work had found that the substitution of Ca^{2+} for Y^{3+} would lead to a greatly destabilized phase, requiring a greater quantity of the stability-promoting, but performance inhibiting Zn^{2+} ion; in this work, it was observed that an In content of 0.1 successfully stabilized contents up to $Y_{0.5}In_{0.1}Ca_{0.4}BaCo_3ZnO_{7+\delta}$, negating the need for increased Zn content. The M-site stability also plays a large role in determining the phase stability of these materials; while increased $Co^{2+/3+}$ content leads to improved electrochemical performance of these materials, it is known to be unstable in the tetrahedrally-coordinated M sites due to a large octahedral site stabilization energy. Here, the composition of $Y_{0.9}In_{0.1}BaCo_3Zn_{0.8}Fe_{0.2}O_{7+\delta}$ was able to be fully-stabilized, and a composition of $Y_{0.9}In_{0.1}BaCo_3Zn_{0.6}Fe_{0.4}O_{7+\delta}$ was stable at both 600 and 800 °C, but decomposed at 700 °C. These studies show that a small substitution of In^{3+} for Y^{3+} can greatly improve the long-term stability of these phases.

The electrochemical performances of the stabilized $RBaCo_3MO_{7+\delta}$ + $Gd_{0.2}Ce_{0.8}O_{1.9}$ (GDC) composite compounds were also investigated. In the $Y_{1-x}In_xCo_3ZnO_{7+\delta}$ series, it was observed that the substitution of In^{3+} for Y^{3+} had very little effect on the overall polarization resistances of the materials, showing that the improved stability granted by In does not negatively impact its ability to function as an IT-SOFC cathode. When compared to the well-studied BSCF material, the performance of the

`

$YBaCo_3ZnO_{7+\delta}$ + GDC composite showed similar polarization resistances in the range of 600 - 800 °C, and was found to have slightly reduced polarization resistances at temperatures in the range of 400 – 600 °C. When substituting the GDC synthesized by solid state reaction in the composite with GDC synthesized by GNP, it was observed that the polarization resistance of the symmetric cells decreased substantially; this shows that the electrochemical performance of these materials are strongly dependent upon the three-phase boundary region, and that further improvement may be possible through careful manipulation of the morphology of the electrode. The substitution of Ca^{2+} for Y^{3+} in the $(Y,In,Ca)BaCo_3ZnO_{7+\delta}$ series was found to produce reduced polarization resistances at all temperatures. While the $Y_{0.8}In_{0.1}Ca_{0.1}BaCo_3ZnO_{7+\delta}$ ($Y_8In_1Ca_1$) + GDC sample was found to slightly outperform the unsubstituted $YBaCo_3ZnO_{7+\delta}$ + GDC composite, the $Y_{0.5}In_{0.1}Ca_{0.4}BaCo_3ZnO_{7+\delta}$ ($Y_5In_1Ca_4$) + GDC composite cathode greatly outperformed $Y_8In_1Ca_1$ at all temperatures, especially in the temperature range of 400 – 600 °C. The improved performance of the increased Ca content is due to the substitution of the divalent Ca^{2+} ion for the trivalent Y^{3+} ion; this substitution was found to increase the oxidation state of the Co ions, leading to a greater covalency of the O – Co – O bond and boosting the oxygen reduction reaction. In the case of the M-site substitution in the $Y_{0.9}In_{0.1}BaCo_3Zn_{1-x}Fe_xO_{7+\delta}$ series of cathodes, electrochemical performances were only measured in the range of $0 \leq x \leq 0.4$ due to the unfavorable stability of the compounds with $x \geq 0.6$. Because Zn^{2+} has an incredibly stable $3d^{10}$ electronic configuration, it cannot participate in electronic conduction or in the oxygen reduction reaction; higher Zn contents invariably lead to diminished performance as SOFC cathode materials, though

`

they are required for phase stability. As such, it was observed that the polarization resistance of the cathodes decreased with increasing $Fe^{2+/3+}$ content, suggesting enhanced electrochemical performance. In particular, the $Y_{0.9}In_{0.1}BaCo_3Zn_{0.6}Fe_{0.4}O_{7+\delta}$ sample showed significantly increased performance over the unsubstituted $Y_{0.9}In_{0.1}BaCo_3ZnO_{7+\delta}$ sample, and showed drastically improved low-temperature performance compared to the well-studied BSCF cathode. Together, these studies show that the electrochemical performance of this class of materials has significant promise when compared to traditional SOFC cathodes, and that future manipulations of chemistry and morphology may yield further improvements in their performance.

The substitution of Sr for Ba in the layered perovskite $LnBa_{1-x}Sr_xCoCuO_{5+\delta}$ (Ln = Nd and Gd) was investigated for phase stability and electrochemical performance. Synthesis of these materials was challenging, with the copper content depressing the melting point of these oxides; the maximum observed Sr substitution resulting in single-phase materials was x = 0.75 for both the Nd and Gd materials. All synthesized materials adopted the tetragonal *P4/mmm* space group, suggesting that the A-site composition is less influential in determining the structure of these materials. The thermal expansion coefficients of all materials were reduced with the substitution of Cu for Co, but it was observed that the increased ionicity of the Nd-O bond compared to the Gd-O bond increased the thermal expansion of the $NdBa_{1-x}Sr_xCoCuO_{5+\delta}$ series of oxides. As the electrical conductivity behavior of these materials are dependent on the O – Co – O bonds, the Ln = Nd series showed increased electrical conductivity compared to the Ln = Gd series due to a reduction in the number of oxygen vacancies and a reduced lattice

`

distortion. The electrochemical performances of the Ln = Nd samples was observed to be higher than that of the Ln = Gd series, as the increased Ln^{3+} ionic radius correlates to an increased bulk oxygen diffusion and surface exchange rate. It was observed that the Sr = 0.75 samples had improved electrochemical performance due to increased cationic lattice disorder and increasing oxide-ion conductivity of the cathodes.

The use of functional silver materials in SOFCs was investigated as a potential substitution for the more expensive, traditionally utilized platinum. Early work discovered that self-assembling silver micromeshes were easily synthesized from silver paste and dispersant, and that these materials had excellent performance as a cathodic current collector. Following work also found that the single-step synthesis of three-dimensional functional silver network was possible through screen printing and heat treating of Ag_2O nanoparticles synthesized by a precipitation reaction. It was observed that the microstructure of these materials could be easily tailored by their processing temperature to produce either increased porosity and surface area, or increased interconnectivity and adhesion to the substrate. Preliminary work with silver materials indicated that they are well-suited for use for cathode-side applications in air atmospheres, but suffer from steam embrittlement in the hydrogen-based anode atmospheres. This embrittlement was successfully avoided through the use of pre-treatments in both high-temperature N_2 atmospheres and low-temperature H_2 atmospheres before exposure to high-temperature H_2. When investigating the performance of silver as an SOFC cathode, it was determined that the performance of

`

silver is primarily transport limited, but also that the silver materials investigated in this work greatly outperformed similar platinum materials.

Overall, this work has provided an improved understanding of alternative cathode materials for IT-SOFCs. In particular, an improved understanding of the structure-property-performance relationships of the *swedenborgite*-type $RBaCo_3MO_{7+\delta}$ (R = Y, In, and Ca; M = Zn and Fe) series of cathodes has been developed. Previous application of these materials was stifled by their poor phase stability on exposure to IT-SOFC operating temperatures; however, through the modification of the crystal chemistry of these materials with appropriate cationic substitutions, it was possible to successfully stabilize the phase at all temperatures of interest. The optimized compositions thus exhibited improved performance without sacrificing the long-term stability, greatly improving their applicability as commercially-viable SOFC cathodes. Investigations with silver discovered the ability for functional silver materials to be manufactured without energy-intensive methods, and in some cases, silver thus prepared was found to show performance superior to the traditionally utilized platinum-based materials.

Future work should focus on a greater understanding of the long-term phase stability of the *swedenborgite*-type materials; the development of a theoretical model would be a great asset to future development of high-performance cathode materials. Other work involving theoretical models would be of great use in determining their oxygen transport and oxygen reduction reaction mechanisms, allowing further gains in performance through modifications in crystal chemistry. Additionally, as the electrochemical performances of these materials have been found to be greatly dependent on the area of the three-phase boundary, future work investigating alternative synthesis routes to optimize the composite morphology may be promising.

LIST OF PUBLICATIONS RELATED TO THIS WORK

1. West, M. & Manthiram, A. Layered $LnBa_{1-x}Sr_xCoCuO_{5+\delta}$ (Ln = Nd and Gd) perovskite cathodes for intermediate temperature solid oxide fuel cells. *International Journal of Hydrogen Energy* **38**, 3364-3372, doi:http://dx.doi.org/10.1016/j.ijhydene.2012.12.133 (2013).

2. West, M., Sher, S.-J. & Manthiram, A. Effects of In substitution in $Y_{1-x}In_xBaCo_3ZnO_{7+\delta}$ ($0 \le x \le 0.5$) cathodes for intermediate temperature solid oxide fuel cells. *Journal of Power Sources* **271**, 252-261, doi:http://dx.doi.org/10.1016/j.jpowsour.2014.08.006 (2014).

3. West, M. & Manthiram, A. Improved phase stability and electrochemical performance of $(Y,In,Ca)BaCo_3ZnO_{7+\delta}$ cathodes for intermediate temperature solid oxide fuel cells. *International Journal of Hydrogen Energy* (in press).

4. West, M., Ortiz, C., & Manthiram, A. High-Performance $Y_{0.9}In_{0.1}BaCo_3(Zn,Fe)O_{7+\delta}$ Swedenborgite-Type Oxide Cathodes for Reduced Temperature Solid Oxide Fuel Cells. *International Journal of Hydrogen Energy* (submitted).

5. West, M. & Manthiram, A. Synthesis Method for 3-Dimensional Silver Network and their Application in Solid Oxide Fuel Cells. *International Journal of Hydrogen Energy* (submitted).

`

REFERENCES

1 Larminie, J. & Dicks, A. *Fuel cell systems explained*. (Wiley, 2000).

2 Alcaide, F., Cabot, P.-L. & Brillas, E. Fuel cells for chemicals and energy cogeneration. *Journal of Power Sources* **153**, 47-60, doi:http://dx.doi.org/10.1016/j.jpowsour.2005.11.041 (2006).

3 Joon, K. Fuel cells – a 21st century power system. *Journal of Power Sources* **71**, 12-18, doi:http://dx.doi.org/10.1016/S0378-7753(97)02765-1 (1998).

4 Nguyen, Q. M. & Takahashi, T. *Science and technology of ceramic fuel cells*. (Elsevier Science, 1995).

5 Dokiya, M. SOFC system and technology. *Solid State Ionics* **152–153**, 383-392, doi:http://dx.doi.org/10.1016/S0167-2738(02)00345-4 (2002).

6 Singhal, S. C. Advances in solid oxide fuel cell technology. *Solid State Ionics* **135**, 305-313, doi:http://dx.doi.org/10.1016/S0167-2738(00)00452-5 (2000).

7 Fabbri, E., Pergolesi, D. & Traversa, E. Materials challenges toward proton-conducting oxide fuel cells: a critical review. *Chemical Society Reviews* **39**, 4355-4369, doi:10.1039/B902343G (2010).

8 Iwahara, H., Esaka, T., Uchida, H. & Maeda, N. Proton conduction in sintered oxides and its application to steam electrolysis for hydrogen production. *Solid State Ionics* **3–4**, 359-363, doi:http://dx.doi.org/10.1016/0167-2738(81)90113-2 (1981).

9 Kreuer, K. D. Proton-conducting oxides. *Annual Review of Materials Research* **33**, 333-359, doi:10.1146/annurev.matsci.33.022802.091825 (2003).

10 Malavasi, L., Fisher, C. A. J. & Islam, M. S. Oxide-ion and proton conducting electrolyte materials for clean energy applications: structural and mechanistic

features. *Chemical Society Reviews* **39**, 4370-4387, doi:10.1039/B915141A (2010).

11 Ricote, S., Bonanos, N., Lenrick, F. & Wallenberg, R. $LaCoO_3$: Promising cathode material for protonic ceramic fuel cells based on a $BaCe_{0.2}Zr_{0.7}Y_{0.1}O_{3-\delta}$ electrolyte. *Journal of Power Sources* **218**, 313-319, doi:http://dx.doi.org/10.1016/j.jpowsour.2012.06.098 (2012).

12 Bard, A. J. & Faulkner, L. R. *Electrochemical methods : fundamentals and applications*. 2nd edn, (Wiley, 2001).

13 Brett, C. M. A. & Brett, A. M. O. *Electrochemistry : principles, methods, and applications*. (Oxford University Press, 1993).

14 Kim, Y. N. *Perovskite-Related and Trigonal $RBaCo_4O_7$-Based Oxide Cathodes for Intermediate Temperature Solid Oxide Fuel Cells* Ph.D. thesis, The University of Texas at Austin, (2011).

15 Yamamoto, O. Solid oxide fuel cells: fundamental aspects and prospects. *Electrochimica Acta* **45**, 2423-2435, doi:http://dx.doi.org/10.1016/S0013-4686(00)00330-3 (2000).

16 Brett, D. J. L., Atkinson, A., Brandon, N. P. & Skinner, S. J. Intermediate temperature solid oxide fuel cells. *Chemical Society Reviews* **37**, 1568-1578, doi:10.1039/B612060C (2008).

17 Gellings, P. J. & Bouwmeester, H. J. M. *The CRC handbook of solid state electrochemistry*. (CRC Press, 1997).

18 Singhal, S. C. & Kendall, K. *High-temperature solid oxide fuel cells : fundamentals, design, and applicatons*. (Elsevier Advanced Technology, 2003).

19 Baur, E. & Preis, H. Über Brennstoff-Ketten mit Festleitern. *Zeitschrift für Elektrochemie und angewandte physikalische Chemie* **43**, 727-732, doi:10.1002/bbpc.19370430903 (1937).

`

20 Sōmiya, S., Yamamoto, N. & Yanagida, H. *Science and technology of zirconia III.* (American Ceramic Society, 1988).

21 Badwal, S. P. S. Zirconia-based solid electrolytes: microstructure, stability and ionic conductivity. *Solid State Ionics* **52**, 23-32, doi:http://dx.doi.org/10.1016/0167-2738(92)90088-7 (1992).

22 Minh, N. Q. Ceramic Fuel Cells. *Journal of the American Ceramic Society* **76**, 563-588, doi:10.1111/j.1151-2916.1993.tb03645.x (1993).

23 Feng, M. a. G., J.B. A superior oxide-ion electrolyte. *European Journal of Solid State and Inorganic Chemistry* **31**, 663-672 (1994).

24 Huang, K., Tichy, R. S. & Goodenough, J. B. Superior Perovskite Oxide-Ion Conductor; Strontium- and Magnesium-Doped $LaGaO_3$: I, Phase Relationships and Electrical Properties. *Journal of the American Ceramic Society* **81**, 2565-2575, doi:10.1111/j.1151-2916.1998.tb02662.x (1998).

25 Huang, P. n. & Petric, A. Superior Oxygen Ion Conductivity of Lanthanum Gallate Doped with Strontium and Magnesium. *Journal of The Electrochemical Society* **143**, 1644-1648, doi:10.1149/1.1836692 (1996).

26 Ishihara, T., Matsuda, H. & Takita, Y. Effects of rare earth cations doped for La site on the oxide ionic conductivity of $LaGaO_3$-based perovskite type oxide. *Solid State Ionics* **79**, 147-151, doi:http://dx.doi.org/10.1016/0167-2738(95)00054-A (1995).

27 Wan, J., Zhu, J. H. & Goodenough, J. B. $La_{0.75}Sr_{0.25}Cr_{0.5}Mn_{0.5}O_{3-\delta}$ + Cu composite anode running on H_2 and CH_4 fuels. *Solid State Ionics* **177**, 1211-1217, doi:http://dx.doi.org/10.1016/j.ssi.2006.04.046 (2006).

28 West, M. & Manthiram, A. Layered $LnBa_{1-x}Sr_xCoCuO_{5+\delta}$ (Ln = Nd and Gd) perovskite cathodes for intermediate temperature solid oxide fuel cells. *International Journal of Hydrogen Energy* **38**, 3364-3372, doi:http://dx.doi.org/10.1016/j.ijhydene.2012.12.133 (2013).

`

29 West, M., Sher, S.-J. & Manthiram, A. Effects of In substitution in $Y_{1-x}In_xBaCo3ZnO7+\delta$ ($0 \leq x \leq 0.5$) cathodes for intermediate temperature solid oxide fuel cells. *Journal of Power Sources* **271**, 252-261, doi:http://dx.doi.org/10.1016/j.jpowsour.2014.08.006 (2014).

30 Gödickemeier, M. & Gauckler, L. J. Engineering of Solid Oxide Fuel Cells with Ceria-Based Electrolytes. *Journal of The Electrochemical Society* **145**, 414-421, doi:10.1149/1.1838279 (1998).

31 Gödickemeier, M., Sasaki, K., Gauckler, L. J. & Riess, I. Electrochemical Characteristics of Cathodes in Solid Oxide Fuel Cells Based on Ceria Electrolytes. *Journal of The Electrochemical Society* **144**, 1635-1646, doi:10.1149/1.1837653 (1997).

32 Tuller, H. L. & Nowick, A. S. Doped Ceria as a Solid Oxide Electrolyte. *Journal of The Electrochemical Society* **122**, 255-259, doi:10.1149/1.2134190 (1975).

33 Eguchi, K., Setoguchi, T., Inoue, T. & Arai, H. Electrical properties of ceria-based oxides and their application to solid oxide fuel cells. *Solid State Ionics* **52**, 165-172, doi:http://dx.doi.org/10.1016/0167-2738(92)90102-U (1992).

34 Virkar, A. V. Theoretical Analysis of Solid Oxide Fuel Cells with Two-Layer, Composite Electrolytes: Electrolyte Stability. *Journal of The Electrochemical Society* **138**, 1481-1487, doi:10.1149/1.2085811 (1991).

35 Duan, Z. *et al.* $Ba_{0.5}Sr_{0.5}Co_{0.8}Fe_{0.2}O_{3-\delta}$ as a cathode for IT-SOFCs with a GDC interlayer. *Journal of Power Sources* **160**, 57-64, doi:http://dx.doi.org/10.1016/j.jpowsour.2006.01.092 (2006).

36 Tsoga, A., Gupta, A., Naoumidis, A. & Nikolopoulos, P. Gadolinia-doped ceria and yttria stabilized zirconia interfaces: regarding their application for SOFC technology. *Acta Materialia* **48**, 4709-4714, doi:http://dx.doi.org/10.1016/S1359-6454(00)00261-5 (2000).

`

37 Kim, J.-H. & Manthiram, A. Low Thermal Expansion $RBa(Co,M)_4O_7$ Cathode Materials Based on Tetrahedral-Site Cobalt Ions for Solid Oxide Fuel Cells†. *Chemistry of Materials* **22**, 822-831, doi:10.1021/cm9015244 (2009).

38 Maricle, D. L., Swarr, T. E. & Karavolis, S. Enhanced ceria — a low-temperature SOFC electrolyte. *Solid State Ionics* **52**, 173-182, doi:http://dx.doi.org/10.1016/0167-2738(92)90103-V (1992).

39 Ogawa, T., Ioroi, T., Ichimoto, Y., Ogumi, Z. & Talrehara, Z.-I. Solid Oxide Fuel Cells III. *The Electrochemical Society Proceedings* (1993).

40 Yoon, D., Su, Q., Wang, H. & Manthiram, A. Superior power density solid oxide fuel cells by enlarging the three-phase boundary region of a NiO-$Ce_{0.8}Gd_{0.2}O_{1.9}$ composite anode through optimized surface structure. *Physical Chemistry Chemical Physics* **15**, 14966-14972, doi:10.1039/C3CP52679H (2013).

41 Horita, T., Sakai, N., Kawada, T., Yokokawa, H. & Dokiya, M. Oxidation and Steam Reforming of CH 4 on Ni and Fe Anodes under Low Humidity Conditions in Solid Oxide Fuel Cells. *Journal of The Electrochemical Society* **143**, 1161-1168, doi:10.1149/1.1836613 (1996).

42 Matsuzaki, Y. & Yasuda, I. The poisoning effect of sulfur-containing impurity gas on a SOFC anode: Part I. Dependence on temperature, time, and impurity concentration. *Solid State Ionics* **132**, 261-269, doi:http://dx.doi.org/10.1016/S0167-2738(00)00653-6 (2000).

43 Steele, B. C. H., Kelly, I., Middleton, H. & Rudkin, R. Oxidation of methane in solid state electrochemical reactors. *Solid State Ionics* **28–30, Part 2**, 1547-1552, doi:http://dx.doi.org/10.1016/0167-2738(88)90417-1 (1988).

44 Yoon, D. & Manthiram, A. Hydrogen tungsten bronze as a decoking agent for long-life, natural gas-fueled solid oxide fuel cells. *Energy & Environmental Science* **7**, 3069-3076, doi:10.1039/C4EE01455C (2014).

45 Yoon, D. & Manthiram, A. Hydrocarbon-fueled solid oxide fuel cells with surface-modified, hydroxylated Sn/Ni-$Ce_{0.8}Gd_{0.2}O_{1.9}$ heterogeneous catalyst anode. *Journal of Materials Chemistry A* **2**, 17041-17046, doi:10.1039/C4TA02662D (2014).

46 Mori, M. & Hiei, Y. Solid Oxide Fuel Cell VI. *The Electrochemical Society Proceedings* (1999).

47 Srilomsak, S., Schilling, D. P. & Anderson, H. U. Solid Oxide fuel Cell I. *The Electrochemical Society Proceedings* (1989).

48 Manthiram, A., Kim, J.-H., Kim, Y. & Lee, K.-T. Crystal chemistry and properties of mixed ionic-electronic conductors. *J Electroceram* **27**, 93-107, doi:10.1007/s10832-011-9635-x (2011).

49 Kostogloudis, G. C., Vasilakos, N. & Ftikos, C. Crystal structure, thermal and electrical properties of $Pr_{1-x}Sr_xCoO_{3-\delta}$ (x = 0, 0.15, 0.3, 0.4, 0.5) perovskite oxides. *Solid State Ionics* **106**, 207-218, doi:http://dx.doi.org/10.1016/S0167-2738(97)00506-7 (1998).

50 De Souza, R. A. & Kilner, J. A. Oxygen transport in $La_{1-x}Sr_xMn_{1-y}Co_yO_{3\pm\delta}$ perovskites: Part I. Oxygen tracer diffusion. *Solid State Ionics* **106**, 175-187, doi:http://dx.doi.org/10.1016/S0167-2738(97)00499-2 (1998).

51 Kamata, H., Hosaka, A., Mizusaki, J. & Tagawa, H. High temperature electrocatalytic properties of the SOFC air electrode $La_{0.8}Sr_{0.2}MnO_3$/YSZ. *Solid State Ionics* **106**, 237-245, doi:http://dx.doi.org/10.1016/S0167-2738(97)00495-5 (1998).

52 Tikhonovich, V. N., Kharton, V. V., Naumovich, E. N. & Savitsky, A. A. Surface modification of La(Sr)MnO_3 electrodes. *Solid State Ionics* **106**, 197-206, doi:http://dx.doi.org/10.1016/S0167-2738(97)00505-5 (1998).

`

53 Tagawa, T., Kyaw Moe, K., Hiramatsu, T. & Goto, S. Design of electrode for solid oxide fuel cells reactor. *Solid State Ionics* **106**, 227-235, doi:http://dx.doi.org/10.1016/S0167-2738(97)00497-9 (1998).

54 Kawada, T. *et al.* Determination of Oxygen Vacancy Concentration in a Thin Film of $La_{0.6}Sr_{0.4}CoO_{3-\delta}$ by an Electrochemical Method. *Journal of The Electrochemical Society* **149**, E252-E259, doi:10.1149/1.1479728 (2002).

55 Zipprich, W., Waschilewski, S., Rocholl, F. & Wiemhöfer, H. D. Improved preparation of $La_{1-x}Me_xCoO_{3-\delta}$ (Me = Sr, Ca) and analysis of oxide ion conductivity with ion conducting microcontacts. *Solid State Ionics* **101–103, Part 2**, 1015-1023, doi:http://dx.doi.org/10.1016/S0167-2738(97)00164-1 (1997).

56 Bae, J.-M. & Steele, B. C. H. Properties of $La_{0.6}Sr_{0.4}Co_{0.2}Fe_{0.8}O_{3-\delta}$ (LSCF) double layer cathodes on gadolinium-doped cerium oxide (CGO) electrolytes: I. Role of SiO_2. *Solid State Ionics* **106**, 247-253, doi:http://dx.doi.org/10.1016/S0167-2738(97)00428-1 (1998).

57 Steele, B. C. H. & Bae, J.-M. Properties of $La_{0.6}Sr_{0.4}Co_{0.2}Fe_{0.8}O_{3-x}$ (LSCF) double layer cathodes on gadolinium-doped cerium oxide (CGO) electrolytes: II. Role of oxygen exchange and diffusion. *Solid State Ionics* **106**, 255-261, doi:http://dx.doi.org/10.1016/S0167-2738(97)00430-X (1998).

58 Adler, S. B. Factors Governing Oxygen Reduction in Solid Oxide Fuel Cell Cathodes. *Chemical Reviews* **104**, 4791-4844, doi:10.1021/cr020724o (2004).

59 Wang, Z. *et al.* Oxygen reduction and transport on the $La_{1-x}Sr_xCo_{1-y}Fe_yO_{3-\delta}$ cathode in solid oxide fuel cells: a first-principles study. *Journal of Materials Chemistry A* **1**, 12932-12940, doi:10.1039/C3TA11554B (2013).

60 Zhang, C. & Bristowe, P. D. First principles calculations of oxygen vacancy formation in barium-strontium-cobalt-ferrite. *RSC Advances* **3**, 12267-12274, doi:10.1039/C3RA41585F (2013).

61 Ried, P., Holtappels, P., Wichser, A., Ulrich, A. & Graule, T. Synthesis and Characterization of $La_{0.6}Sr_{0.4}Co_{0.2}Fe_{0.8}O_{3-\delta}$ and $Ba_{0.5}Sr_{0.5}Co_{0.8}Fe_{0.2}O_{3-\delta}$. *Journal of The Electrochemical Society* **155**, B1029-B1035, doi:10.1149/1.2960873 (2008).

62 Kim, J.-H. & Manthiram, A. $LnBaCo_2O_{5+\delta}$ Oxides as Cathodes for Intermediate-Temperature Solid Oxide Fuel Cells. *Journal of The Electrochemical Society* **155**, B385-B390, doi:10.1149/1.2839028 (2008).

63 Señarís-Rodríguez, M. A. & Goodenough, J. B. Magnetic and Transport Properties of the System $La_{1-x}Sr_xCoO_{3-\delta}$ ($0 \leq x \leq 0.50$). *Journal of Solid State Chemistry* **118**, 323-336, doi:http://dx.doi.org/10.1006/jssc.1995.1351 (1995).

64 Fergus, J. W. Lanthanum chromite-based materials for solid oxide fuel cell interconnects. *Solid State Ionics* **171**, 1-15 (2004).

65 Hjalmarsson, P., Søgaard, M., Hagen, A. & Mogensen, M. Structural properties and electrochemical performance of strontium-and nickel-substituted lanthanum cobaltite. *Solid State Ionics* **179**, 636-646 (2008).

66 Wandekar, R., Wani, B. & Bharadwaj, S. Crystal structure, electrical conductivity, thermal expansion and compatibility studies of Co-substituted lanthanum strontium manganite system. *Solid State Sciences* **11**, 240-250 (2009).

67 Parkkima, O., Yamauchi, H. & Karppinen, M. Oxygen Storage Capacity and Phase Stability of Variously Substituted $YBaCo_4O_{7+\delta}$. *Chemistry of Materials* **25**, 599-604, doi:10.1021/cm3038729 (2013).

68 Parkkima, O. & Karppinen, M. The $YBaCo_4O_{7+\delta}$-Based Functional Oxide Material Family: A Review. *European Journal of Inorganic Chemistry* **2014**, 4056-4067, doi:10.1002/ejic.201402135 (2014).

69 Avci, S. *et al.* Oxygen Stoichiometry in the Geometrically Frustrated Kagomé System YBaCo4O7+δ: Impact on Phase Behavior and Magnetism. *Chemistry of Materials* **25**, 4188-4196, doi:10.1021/cm401710b (2013).

70 Kadota, S., Karppinen, M., Motohashi, T. & Yamauchi, H. R-Site Substitution Effect on the Oxygen-Storage Capability of $RBaCo_4O_{7+\delta}$. *Chemistry of Materials* **20**, 6378-6381, doi:10.1021/cm801412q (2008).

71 Zhou, Q. *et al.* Novel $YBaCo_{3.2}Ga_{0.8}O_{7+\delta}$ as a cathode material and performance optimization for IT-SOFCs. *International Journal of Hydrogen Energy* **39**, 10710-10717, doi:http://dx.doi.org/10.1016/j.ijhydene.2014.04.206 (2014).

72 Zhou, Q. *et al.* Preparation, characterization, and electrochemical properties of $YBaCo_{3.4}Al_{0.3}Ga_{0.3}O_{7+\delta}$ and $YBaCo_{3.2}Al_{0.4}Ga_{0.4}O_{7+\delta}$ cathodes for IT-SOFCs. *Ceramics International* **40**, 13481-13485, doi:http://dx.doi.org/10.1016/j.ceramint.2014.05.075 (2014).

73 O'Hayre, R., Barnett, D. M. & Prinz, F. B. The Triple Phase Boundary: A Mathematical Model and Experimental Investigations for Fuel Cells. *Journal of The Electrochemical Society* **152**, A439-A444, doi:10.1149/1.1851054 (2005).

74 Kim, Y. N., Kim, J. H., Huq, A., Paranthaman, M. P. & Manthiram, A. $(Y_{0.5}In_{0.5})Ba(Co,Zn)_4O_7$ cathodes with superior high-temperature phase stability for solid oxide fuel cells. *Journal of Power Sources* **214**, 7-14, doi:http://dx.doi.org/10.1016/j.jpowsour.2012.03.050 (2012).

75 Chick, L. A. *et al.* Glycine-nitrate combustion synthesis of oxide ceramic powders. *Materials Letters* **10**, 6-12, doi:http://dx.doi.org/10.1016/0167-577X(90)90003-5 (1990).

76 Taguchi, H., Matsuda, D., Nagao, M., Tanihata, K. & Miyamoto, Y. Synthesis of Perovskite-Type $(La_{1-x}Sr_x)MnO_3$ $(0 \le x \le 0.3)$ at Low Temperature. *Journal of the American Ceramic Society* **75**, 201-202, doi:10.1111/j.1151-2916.1992.tb05465.x (1992).

77 Kleinlogel, C. & Gauckler, L. J. Sintering of Nanocrystalline CeO_2 Ceramics. *Advanced Materials* **13**, 1081-1085, doi:10.1002/1521-4095(200107)13:14<1081::AID-ADMA1081>3.0.CO;2-D (2001).

78 Nicholas, J. D. & De Jonghe, L. C. Prediction and evaluation of sintering aids for Cerium Gadolinium Oxide. *Solid State Ionics* **178**, 1187-1194, doi:http://dx.doi.org/10.1016/j.ssi.2007.05.019 (2007).

79 Kim, Y. N. & Manthiram, A. Layered $LnBaCo_{2-x}Cu_{x}O_{5+\delta}$ $(0 \leqslant x \leqslant 1.0)$ Perovskite Cathodes for Intermediate-Temperature Solid Oxide Fuel Cells. *Journal of The Electrochemical Society* **158**, B276-B282, doi:10.1149/1.3527006 (2011).

80 Rodríguez-Carvajal, J. Recent advances in magnetic structure determination by neutron powder diffraction. *Physica B: Condensed Matter* **192**, 55-69, doi:http://dx.doi.org/10.1016/0921-4526(93)90108-I (1993).

81 Pecharsky, V. K. & Zavalij, P. Y. *Fundamentals of powder diffraction and structural characterization of materials*. 2nd edn, (Springer, 2009).

82 Rietveld, H. M. A Profile Refinement Method for Nuclear and Magnetic Structures. *Journal of Applied Crystallography* **2**, 65-71 (1969).

83 Will, G. *Powder diffraction : the Rietveld method and the two-stage method to determine and refine crystal structures from powder diffraction data*. (Springer, 2006).

84 Manthiram, A., Swinnea, J. S., Sui, Z. T., Steinfink, H. & Goodenough, J. B. The influence of oxygen variation on the crystal structure and phase composition of the superconductor yttrium barium copper oxide ($YBa_2Cu_3O_{7-x}$). *Journal of the American Chemical Society* **109**, 6667-6669, doi:10.1021/ja00256a019 (1987).

85 Riess, I. Method for determining the electrode overpotential on circular samples. *Journal of Applied Physics* **71**, 4079-4081, doi:doi:http://dx.doi.org/10.1063/1.350833 (1992).

86 Van der Pauw, L. J. A method of measuring specific resistivity and Hall effect of discs of arbitrary shape. *Philips Research Reports* **13**, 1-9 (1958).

87 Van der Pauw, L. J. A method of measuring the resistivity and Hall coefficient on lamellae of arbitrary shape. *Philips Research Reports* **20**, 220-224 (1958).

88 Kim, J.-H., Prado, F. & Manthiram, A. Characterization of $GdBa_{1-x}Sr_xCo_2O_{5+\delta}$ $(0 \leqslant x \leqslant 1.0)$ Double Perovskites as Cathodes for Solid Oxide Fuel Cells. *Journal of The Electrochemical Society* **155**, B1023-B1028, doi:10.1149/1.2965792 (2008).

89 Kim, J., Jun, A., Shin, J. & Kim, G. Effect of Fe Doping on Layered $GdBa_{0.5}Sr_{0.5}Co_2O_{5+\delta}$ Perovskite Cathodes for Intermediate Temperature Solid Oxide Fuel Cells. *Journal of the American Ceramic Society* **97**, 651-656, doi:10.1111/jace.12692 (2014).

90 Kim, J. H., Kim, Y. N., Cho, S. M., Wang, H. & Manthiram, A. Electrochemical characterization of $YBaCo_3ZnO_7$ + $Gd_{0.2}Ce_{0.8}O_{1.9}$ composite cathodes for intermediate temperature solid oxide fuel cells. *Electrochimica Acta* **55**, 5312-5317, doi:http://dx.doi.org/10.1016/j.electacta.2010.04.058 (2010).

91 Kim, Y. N., Kim, J.-H. & Manthiram, A. Characterization of $(Y_{1-x}Ca_x)_{BaCo4-y}Zn_yO_7$ as cathodes for intermediate temperature solid oxide fuel cells. *International Journal of Hydrogen Energy* **36**, 15295-15303, doi:http://dx.doi.org/10.1016/j.ijhydene.2011.08.089 (2011).

92 Li, S. & Xie, K. Composite Oxygen Electrode Based on LSCF and BSCF for Steam Electrolysis in a Proton-Conducting Solid Oxide Electrolyzer. *Journal of The Electrochemical Society* **160**, F224-F233, doi:10.1149/2.027303jes (2013).

93 Shannon, R. Revised effective ionic radii and systematic studies of interatomic distances in halides and chalcogenides. *Acta Crystallographica Section A* **32**, 751-767, doi:doi:10.1107/S0567739476001551 (1976).

94 Hao, H. *et al.* Oxygen adsorption properties of $YBaCo_4O_7$-type compounds. *Solid State Ionics* **177**, 631-637, doi:http://dx.doi.org/10.1016/j.ssi.2006.01.030 (2006).

`

95 Haynes, W. M., R., L. D., J., B. T. & Press, C. R. C. *CRC handbook of chemistry and physics : a ready-reference book of chemical and physical data*. (2013).

96 Guo, Y. *et al.* Significant impact of the current collection material and method on the performance of $Ba_{0.5}Sr_{0.5}Co_{0.8}Fe_{0.2}O_{3-\delta}$ electrodes in solid oxide fuel cells. *Journal of Power Sources* **196**, 5511-5519, doi:http://dx.doi.org/10.1016/j.jpowsour.2011.02.056 (2011).

97 Huang, H., Holme, T. P. & Prinz, F. B. Oxygen Reduction Characteristics on Ag, Pt, and Ag-Pt Alloys in Low-Temperature SOFCs. *ECS Transactions* **3**, 31-40, doi:10.1149/1.2789268 (2007).

98 Shim, J. H., Kim, Y. B., Park, J. S. & Prinz, F. B. Silver Nanomesh as a Cathode for Solid Oxide Fuel Cells. *ECS Transactions* **35**, 2209-2212, doi:10.1149/1.3570214 (2011).

99 Adler, S. B., Chen, X. Y. & Wilson, J. R. Mechanisms and rate laws for oxygen exchange on mixed-conducting oxide surfaces. *Journal of Catalysis* **245**, 91-109, doi:http://dx.doi.org/10.1016/j.jcat.2006.09.019 (2007).

100 Choi, S. *et al.* Highly efficient and robust cathode materials for low-temperature solid oxide fuel cells: $PrBa_{0.5}Sr_{0.5}Co_{2-x}Fe_xO_{5+\delta}$. *Sci. Rep.* **3**, doi:10.1038/srep02426 (2013).

101 Liu, M. & Hu, H. Effect of Interfacial Resistance on Determination of Transport Properties of Mixed-Conducting Electrolytes. *Journal of The Electrochemical Society* **143**, L109-L112, doi:10.1149/1.1836892 (1996).

102 Pauling, L., King, H. P. & Winchell, A. N. The crystal structure of swedenborgite, $NaBe_4SbO_7$. *American Minerologist* **20**, 492 - 501 (1935).

103 Lee, Y.-L., Kleis, J., Rossmeisl, J., Shao-Horn, Y. & Morgan, D. Prediction of solid oxide fuel cell cathode activity with first-principles descriptors. *Energy & Environmental Science* **4**, 3966-3970, doi:10.1039/C1EE02032C (2011).

104 Pavone, M., Ritzmann, A. M. & Carter, E. A. Quantum-mechanics-based design principles for solid oxide fuel cell cathode materials. *Energy & Environmental Science* **4**, 4933-4937, doi:10.1039/C1EE02377B (2011).

105 Suntivich, J. *et al.* Design principles for oxygen-reduction activity on perovskite oxide catalysts for fuel cells and metal–air batteries. *Nat Chem* **3**, 546-550, doi:http://www.nature.com/nchem/journal/v3/n7/abs/nchem.1069.html#supplementary-information (2011).

106 Kim, J.-H. *et al.* High temperature phase stabilities and electrochemical properties of $InBaCo_{4-x}Zn_xO_7$ cathodes for intermediate temperature solid oxide fuel cells. *Electrochimica Acta* **56**, 5740-5745, doi:http://dx.doi.org/10.1016/j.electacta.2011.04.047 (2011).

107 West, M. & Manthiram, A. Improved phase stability and electrochemical performance of $(Y,In,Ca)BaCo_3ZnO_{7+\delta}$ cathodes for intermediate temperature solid oxide fuel cells. *International Journal of Hydrogen Energy* **In press** (2014).

108 Kim, J.-H. *et al.* High Temperature Crystal Chemistry and Oxygen Permeation Properties of the Mixed Ionic–Electronic Conductors $LnBaCo_2O_{5+\delta}$ (Ln = Lanthanide) *Journal of The Electrochemical Society* **156**, B1376-B1382, doi:10.1149/1.3231501 (2009).

109 Mogensen, M., Lybye, D., Bonanos, N., Hendriksen, P. V. & Poulsen, F. W. Factors controlling the oxide ion conductivity of fluorite and perovskite structured oxides. *Solid State Ionics* **174**, 279-286, doi:http://dx.doi.org/10.1016/j.ssi.2004.07.036 (2004).

110 Parfitt, D., Chroneos, A., Tarancon, A. & Kilner, J. A. Oxygen ion diffusion in cation ordered/disordered $GdBaCo_2O_{5+\delta}$. *Journal of Materials Chemistry* **21**, 2183-2186, doi:10.1039/C0JM02924F (2011).

111 Cook, R. L. & Sammells, A. F. On the systematic selection of perovskite solid electrolytes for intermediate temperature fuel cells. *Solid State Ionics* **45**, 311-321, doi:http://dx.doi.org/10.1016/0167-2738(91)90167-A (1991).

112 Sammells, A. F., Cook, R. L., White, J. H., Osborne, J. J. & MacDuff, R. C. Rational selection of advanced solid electrolytes for intermediate temperature fuel cells. *Solid State Ionics* **52**, 111-123, doi:http://dx.doi.org/10.1016/0167-2738(92)90097-9 (1992).

113 Cook, R. L., Osborne, J. J., White, J. H., MacDuff, R. C. & Sammells, A. F. Investigations on $BaTh_{0.9}Gd_{0.1}O_3$ as an Intermediate Temperature Fuel Cell Solid Electrolyte. *Journal of The Electrochemical Society* **139**, L19-L20, doi:10.1149/1.2069273 (1992).

114 Acres, G. J. K. Recent advances in fuel cell technology and its applications. *Journal of Power Sources* **100**, 60-66, doi:http://dx.doi.org/10.1016/S0378-7753(01)00883-7 (2001).

115 Gasteiger, H. A., Kocha, S. S., Sompalli, B. & Wagner, F. T. Activity benchmarks and requirements for Pt, Pt-alloy, and non-Pt oxygen reduction catalysts for PEMFCs. *Applied Catalysis B: Environmental* **56**, 9-35, doi:http://dx.doi.org/10.1016/j.apcatb.2004.06.021 (2005).

116 Liu, H. *et al.* A review of anode catalysis in the direct methanol fuel cell. *Journal of Power Sources* **155**, 95-110, doi:http://dx.doi.org/10.1016/j.jpowsour.2006.01.030 (2006).

117 McLean, G. F., Niet, T., Prince-Richard, S. & Djilali, N. An assessment of alkaline fuel cell technology. *International Journal of Hydrogen Energy* **27**, 507-526, doi:http://dx.doi.org/10.1016/S0360-3199(01)00181-1 (2002).

118 Nørskov, J. K. *et al.* Origin of the Overpotential for Oxygen Reduction at a Fuel-Cell Cathode. *The Journal of Physical Chemistry B* **108**, 17886-17892, doi:10.1021/jp047349j (2004).

`

119 O'Hayre, R. P. *Fuel cell fundamentals*. 2nd edn, (John Wiley & Sons, 2009).

120 Wang, Y., Chen, K. S., Mishler, J., Cho, S. C. & Adroher, X. C. A review of polymer electrolyte membrane fuel cells: Technology, applications, and needs on fundamental research. *Applied Energy* **88**, 981-1007, doi:http://dx.doi.org/10.1016/j.apenergy.2010.09.030 (2011).

121 Watanabe, M. & Motoo, S. Electrocatalysis by ad-atoms: Part II. Enhancement of the oxidation of methanol on platinum by ruthenium ad-atoms. *Journal of Electroanalytical Chemistry and Interfacial Electrochemistry* **60**, 267-273, doi:http://dx.doi.org/10.1016/S0022-0728(75)80261-0 (1975).

122 Tietz, F. Thermal expansion of SOFC materials. *Ionics* **5**, 129-139, doi:10.1007/BF02375916 (1999).

123 Wei, T. *et al.* A modified liquid-phase-assisted sintering mechanism for $La_{0.8}Sr_{0.2}Cr_{1-x}Fe_xO_{3-\delta}$—A high density, redox-stable perovskite interconnect for solid oxide fuel cells. *Journal of Power Sources* **250**, 152-159, doi:http://dx.doi.org/10.1016/j.jpowsour.2013.11.012 (2014).

124 Jørgensen, M. J. & Mogensen, M. Impedance of Solid Oxide Fuel Cell LSM/YSZ Composite Cathodes. *Journal of The Electrochemical Society* **148**, A433-A442, doi:10.1149/1.1360203 (2001).

125 Tsai, T. & Barnett, S. A. Effect of LSM-YSZ cathode on thin-electrolyte solid oxide fuel cell performance. *Solid State Ionics* **93**, 207-217, doi:http://dx.doi.org/10.1016/S0167-2738(96)00524-3 (1997).

126 KITCO. *New York Spot Price*, <www.kitco.com/market> (2014).

127 Lea, M. C. On the Reactions of Ethylamine and Diethylamine. *The American Journal of Science and Arts* **33**, 80-86 (1862).

128 Panáček, A. *et al.* Polyacrylate-Assisted Size Control of Silver Nanoparticles and Their Catalytic Activity. *Chemistry of Materials* **26**, 1332-1339, doi:10.1021/cm400635z (2014).

129 Hood, G. C. & Murphy, G. W. The decomposition of silver oxide—An autocatalytic reaction. *Journal of Chemical Education* **26**, 169, doi:10.1021/ed026p169 (1949).

130 Benton, A. F. & Drake, L. C. Kinetics of Reaction and Adsorption in the System Silver—Oxygen. *Journal of the American Chemical Society* **56**, 255-263, doi:10.1021/ja01317a001 (1934).

131 L'Vov, B. V. Kinetics and mechanism of thermal decomposition of silver oxide. *Thermochimica Acta* **333**, 13-19, doi:http://dx.doi.org/10.1016/S0040-6031(99)00085-4 (1999).

132 Takagi, M. Electron-Diffraction Study of Liquid-Solid Transition of Thin Metal Films. *Journal of the Physical Society of Japan* **9**, 359-363, doi:10.1143/JPSJ.9.359 (1954).

133 Rahimian, M., Ehsani, N., Parvin, N. & Baharvandi, H. R. The effect of particle size, sintering temperature and sintering time on the properties of Al–Al_2O_3 composites, made by powder metallurgy. *Journal of Materials Processing Technology* **209**, 5387-5393, doi:http://dx.doi.org/10.1016/j.jmatprotec.2009.04.007 (2009).

134 Louthan, M. R., Jr. Hydrogen Embrittlement of Metals: A Primer for the Failure Analyst. *J Fail. Anal. and Preven.* **8**, 289-307, doi:10.1007/s11668-008-9133-x (2008).

135 Klueh, R. L. & Mullins, W. W. Some Observations on Hydrogen Embrittlement of Silver. *Transactions of the Metallurgical Society of AIME* **242**, 237-244 (1968).

136 Steacie, E. W. R. & Johnson, F. M. G. The Solubility and Rate of Solution of Oxygen in Silver. *Proceedings of the Royal Society of London. Series A* **112**, 542-558, doi:10.1098/rspa.1926.0128 (1926).

137 Van Herle, J. & McEvoy, A. J. Oxygen diffusion through silver cathodes for solid oxide fuel cells. *Journal of Physics and Chemistry of Solids* **55**, 339-347, doi:http://dx.doi.org/10.1016/0022-3697(94)90230-5 (1994).

138 Jiménez, R. *et al*. Reaction-Zone Expansions and Mechanism of the O_2, Ag/Yttria-Stabilized Zirconia Electrode Reaction. *Journal of the Electrochemical Society* **144**, 582-585 (1997).